Title

Development of a Planar Multiple Electrode Array for Spatially-Resolved Transepithelial Electrical Resistance Measurements

Permalink

https://escholarship.org/uc/item/847091hn

Author

Gardner, Alexander Davis

Publication Date

2023

Peer reviewed|Thesis/dissertation

Development of a Planar Multiple Electrode Array for Spatially-Resolved Transepithelial
Electrical Resistance Measurements

By

ALEXANDER DAVIS GARDNER
THESIS

Submitted in partial satisfaction of the requirements for the degree of

MASTER OF SCIENCE

in

Electrical and Computer Engineering

in the

OFFICE OF GRADUATE STUDIES

of the

UNIVERSITY OF CALIFORNIA

DAVIS

Approved:

_____

Erkin Şeker, Chair

_____

Hyoyoung Jeong

_____

Rajeevan Amirtharajah

Committee in Charge

2023

i

Abstract

In vitro cell culture models are quickly replacing animal models for drug development, mechanistic studies, and precision medicine. Visual methods are the primary means of studying organ-on-a-chip (OoC) models, but are limited to microscopy and immunofluorescent staining protocols. These techniques expose tissues to an adverse environment outside of an incubator or must be prepared with fluorescent proteins, which may affect the underlying cellular processes. In addition, these quantification approaches are often end-point assessments, limiting the number of measurements from a sample.

Impedance-based methods allow for continuous monitoring of the electrical properties of tissues that provide insight into biochemical and cellular mechanisms. Transepithelial electrical resistance (TEER) is a useful metric for quantifying the integrity of an epithelial cell layer (e.g., gut epithelium), but lacks the spatial resolution of the microscopic techniques. This thesis reports on the design and experimental validation of a distributed hardware including a voltage-controlled current source (VCCS) for safe current injection, TEER measurement circuitry to sample the impedance across conductive phantoms, and real-time data conversion for monitoring changes in the system. Tomographic concepts will be adapted from electrical impedance tomography (EIT) systems to realize a distributed TEER device capable of continuous, non-invasive spatial imaging of tissues. Multiplexers will spatially expand the TEER measurement circuitry to detect minor changes in impedance by gathering a representative sample of data from the entire chip. The system is validated using conductive and insulating phantoms in saline tanks with varying size and orientation. Finally, EIT image reconstruction techniques are used for converting the raw data to images with high spatial resolution. This platform should be broadly applicable to real-time monitoring of developing in vitro tissue cultures and spatial detection of barrier disruptions, and can be scaled for studies requiring frequency sweeps or higher resolution images.

Table of Contents

List of Figures

List of Tables

List of Abbreviations

ADC - Analog-to-Digital Converter

CUT - Culture-Under-Test

DDS - Direct Digital Synthesis

EIDORS - Electrical Impedance Tomography and Diffuse Optical Tomography Reconstruction

Software

EIS- Electrical Impedance Spectroscopy

EIT - Electrical Impedance Tomography

FEM - Finite Element Method

LDO - Low-dropout Voltage Regulator

LUT - Lookup Table

OoC - Organ-on-a-Chip

PDMS - Polydimethylsiloxane

PETE - Polyethylene Terephthalate

PGA - Programmable Gain

SNR - Signal-to-Noise Ratio

SPS - Samples per Second

TEER - Transepithelial Electrical Resistance

TIA - Transimpedance Amplifier

VCCS - Voltage Controlled Current Source

List of Symbols

σ Unknown conductivity distribution

σ_0 Homogeneous conductivity

η Conductivity perturbation

u, U Voltage of the body

$j(x, y)$ Current density

B Body of interest for EIT application

$\sigma(p)$ Conductivity at a point p in body B

ϵ Regularization parameter or smoothing parameter

Acknowledgements

I would like to thank the members of the Şeker Lab, especially Hyehyun Kim, Greg Girardi, and Dr. Noah Goshi, for their patience in teaching wet bench techniques and Caco-2 epithelial tissue husbandry. A special thanks to my PI, Dr. Erkin Şeker, for his guidance throughout this research endeavor. It was a true pleasure to realize this platform from our initial discussions on designing a TEER device through the prototyping iterations to the final design.

A special thanks to my mother, Amy, my father, Stewart, and my siblings, Stewart, William, and Marguerite, for encouraging me throughout this project. I would also like to thank Natalie for the warmth she has shown to me every step of the way. I thank my friends Izzy and Trevor, two friends who I could always count on for help or just a much needed break. And of course, I thank my best friends, Ian, Wyatt, Nathan, and Stuart for the much needed laughter and goofing off that has kept me sane.

Chapter 1 - Introduction

In studying cell culture morphology, the most common method is bright-field microscopy, which provides basic information about the spatial organization and shape of cells, which can be further quantified for inferences about cell behavior (e.g., cellular fragmentation suggesting cell death). Fluorescence microscopy, enabled by staining cells based on their genomic, proteomic, or functional states, provides even richer information about the cell behavior. These techniques; however, both have shortcomings. For example, it is generally necessary to chemically fix the cells for staining in fluorescence microscopy, after which the cells are no longer alive. As an alternative, electrical impedance tomography is a nondestructive technique and has the potential to provide additional details about cellular state and function compared to microscopy-based techniques.

Electrical Impedance Measurements

Research into the electrical properties of tissue have revealed the unique properties of different tissues in close proximity. Studies of cancerous tissues in breasts have revealed that healthy and cancerous tissue differ in the density of tumor stroma which affects their relative impedances. Conductivity of blood has been used as an electrical marker to detect the circulation of blood through tissue and to detect pooling of blood. Ion fluxes in/out of neurons has been used to detect conductivity changes in different regions of the brain [1][2]. Through precise measurements, all of these properties show promise as applications of nondestructive impedance imaging assays capable of real-time monitoring and diagnosis.

Electrical Impedance Tomography

Electrical impedance measurements for image reconstruction have been of interest since the early 1900s. The concept of Electrical Impedance Tomography (EIT) for medical screening was adopted from the geophysical community that used electrical resistivity tomography to resolve the location of ore and the movement of groundwater as early as 1911. Interest in medical applications began with early research in the 1970s for thoracic imaging,

which led to increased research in the application of EIT for brain, breast, and mixed tissues [1]. Within the last 20 years, commercial devices have become available for pediatric and adult ventilation monitoring since EIT is non-invasive and is able to continuously image the body over long durations with insignificant influence on the tissue properties [3].

EIT is founded on the basic principles of Kirchhoff's Laws. A constant current is injected into a body and the voltage is measured at the remaining electrodes on the periphery (Figure 1.1). From these measurements, impedance data is calculated, which can be used for monitoring changes over time, like many impedance spectroscopy applications. Tomographic applications take an entire frame of measurement data, or the data from each electrode when alternating current injection profiles are administered, and reconstruct a prediction of the conductivity within the body. Small perturbations in the impedance at each electrode are all that is required to predict the object's shape, location, or even the presence of multiple objects. This is useful for applications where implicit knowledge of an object's position, or even the position of tissues, is unknown.

Switching sequences
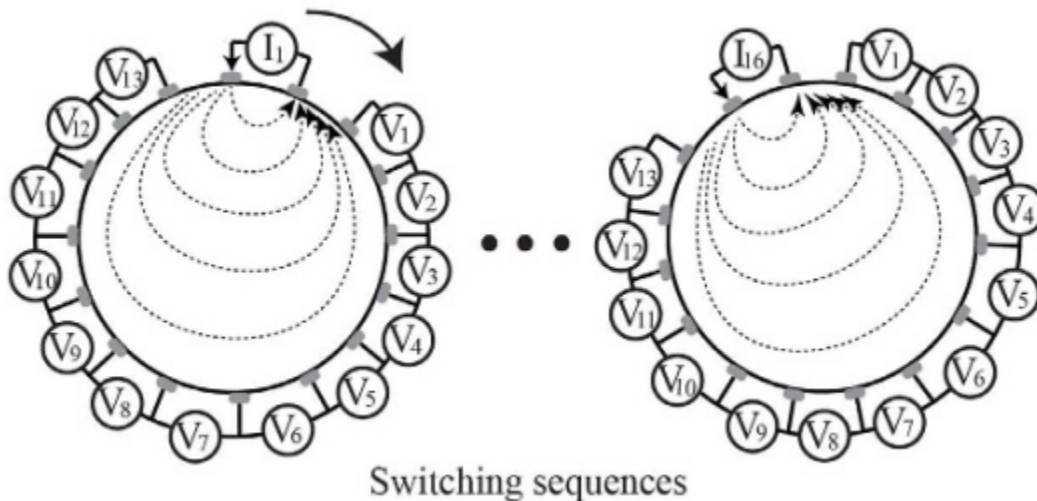
Figure 1.1 Current injection and voltage measurement sequence for an adjacent pattern [4].

The specific pattern of current drive and voltage measurement can have significant impacts on a system's spatial detection capability. Figure 1.2 shows some of the patterns employed, with black electrodes indicating current carrying electrodes, and red electrodes

2

indicating voltage measurement. The color gradient of the system represents the sensitivity of each four-terminal electrode combination. Sensitivity is a complex function of overlapping electric fields generated by the current carrying electrode pair and a reciprocal electric field generated by current injected through the voltage measurement electrode pair. The resulting sensitivity matrix describes the effect that every point has on the measured impedance. Areas with high sensitivity are hotter colors, lower sensitivity is represented with cooler colors. Positively and negatively sensitive areas are important because they indicate the areas where a change in conductivity is best measured. Areas with near zero sensitivity are an issue because a change in conductivity will not be measured [5]. For an application where objects are expected to be nearest to the periphery, a neighboring (often referred to as adjacent) pattern is useful because there is the highest sensitivity in the region immediately around the electrodes. Depth detection applications that require resolving objects closer to the center would benefit from an opposite or cross pattern because they have a nearly uniform, positive sensitivity across the entirety of the chamber.
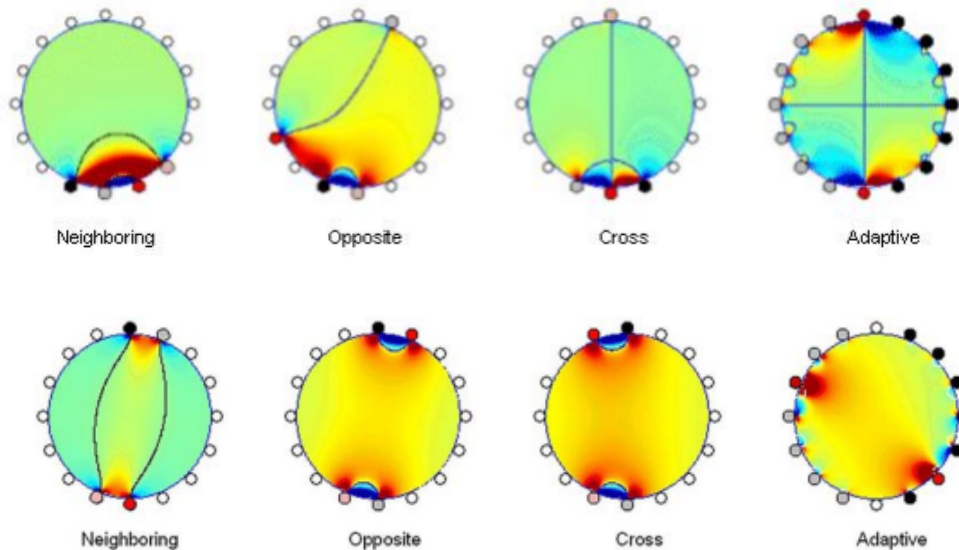
Figure 1.2 Sensitivity distribution among different EIT stimulation patterns [5].

In considering the specifics of an EIT design, it is first necessary to define the application. If the application involves rapid, continuous measurement of the body, it is important

to consider the tradeoff of sensed paths from current injection/voltage sense pairings and the desired frame rate. To measure a complete frame of an EIT system, we will consider the four-pole systems of Figure 1.3 using the neighboring method. For a set of measurements, current is driven across two electrodes, and a differential voltage measurement is taken at every other electrode as in Figure 1.1. A complete measurement frame from a system of 8 electrodes requires 40 measurements, following a formula of $(N_{elec} - 3) \cdot N_{elec}$. For a 32 electrode system, the measurements needed for a single frame quickly slow down the frame rate, needing 928 measurements to cover the entire frame.

When deciding the necessary number of electrodes for the EIT application, it is important to consider the inverse relationship between higher electrode counts and image spatial resolution clarity. From Figure 1.4, it is clear that the application in [6] benefits most from a 16 electrode system which has a comparable image quality to a 32 electrode system. The 16 electrode system exhibits a 5.3x faster frame acquisition rate and a 4.46x reduction in the measurements needed to acquire a clear image with as many as five inclusions. Although there is greater coverage within the body, systems with higher numbers of electrodes must compensate for lower frame rates, increased hardware complexity, and decreased image sharpening.
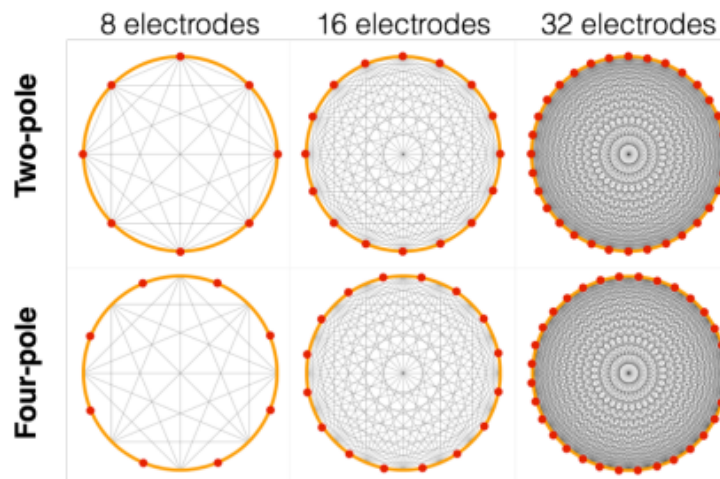
Figure 1.3 Surface coverage among two-pole and four pole electrode systems [6].
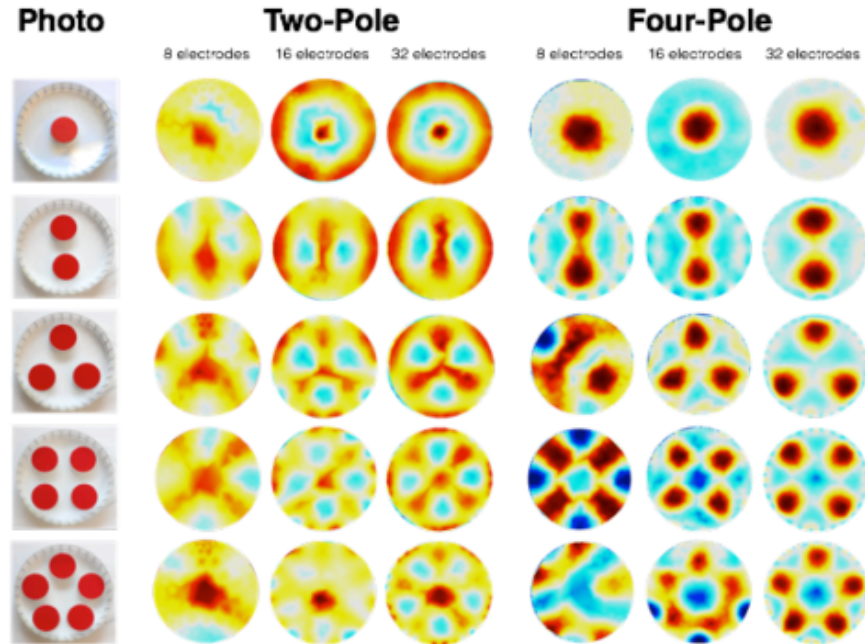
Figure 1.4 Clarity comparison of different inclusion orientations and number of electrodes. Image improvement plateaus as diminishing improvements to image quality are made by increasing the electrode count [6].

Though the adjacent method is popular for its high coverage, the detection of an internal body is not optimized with this pattern. Trigonometric patterns that space current drive and voltage measurement electrodes by 90° perform 5x better in a 16 electrode system. Adler *et al.* [7] reported that adjacent patterns are best suited to detect objects near the boundary of a system. An OoC device with a permeable membrane situated between electrode planes will not benefit from heightened boundary sensitivity, making selection of a compatible pattern all the more critical.

A final consideration for an EIT system is the practical application. Is a single set of measurements all that is needed, or is the device intended for long term functional monitoring? To answer this question, three main EIT modalities have been developed. *Absolute EIT* reconstructs images from a single set of measurements. *Frequency-difference EIT* takes measurements at two or more frequencies and calculates the difference in impedance between

the two frequencies. *Time-difference EIT* takes measurements over time to reduce the sensitivity of the system to errors associated with interference from patient movement. Of these functional monitoring techniques, absolute EIT is the most susceptible to inaccuracies in the model geometry, electrode properties, and from signal-to-noise ratio (SNR) in the amplifier stages. Time-difference EIT shows the most stability [1].

Electrical Impedance Spectroscopy

In the literature, EIT is the process of recreating impedance images from boundary measurements around a body. Electrical Impedance Spectroscopy (EIS), while similar to EIT, is often used for non-invasive and label-free measurements of cell capacitance and resistance. Although the terms EIS and EIT are sometimes used interchangeably in the literature, there are two key differences. EIT generally uses a single AC current frequency whereas EIS uses a frequency sweep to isolate data from different cellular components (e.g., the paracellular and transcellular pathways). When an application uses EIS specifically, there is a focus on the raw electrical data over the visual reconstruction of an image and EIS applications are more commonly employed on tissues cultured on planar, porous membranes. EIT, on the other hand, would be applied to studying boundary changes on surfaces where electrodes can be evenly spaced (e.g., thoracic changes from ventilation).

Tissues have unique electrical properties that are expressed at different frequencies, shown in Figures 1.5 and 1.6. A frequency sweep within the range of 0.1 Hz to 10 MHz is common among EIS systems to quantify the contribution of the cell membrane, intercellular junctions, etc. EIS has been applied to epithelial culture monitoring, but has yet to show its capability as an effective imaging technique.

6
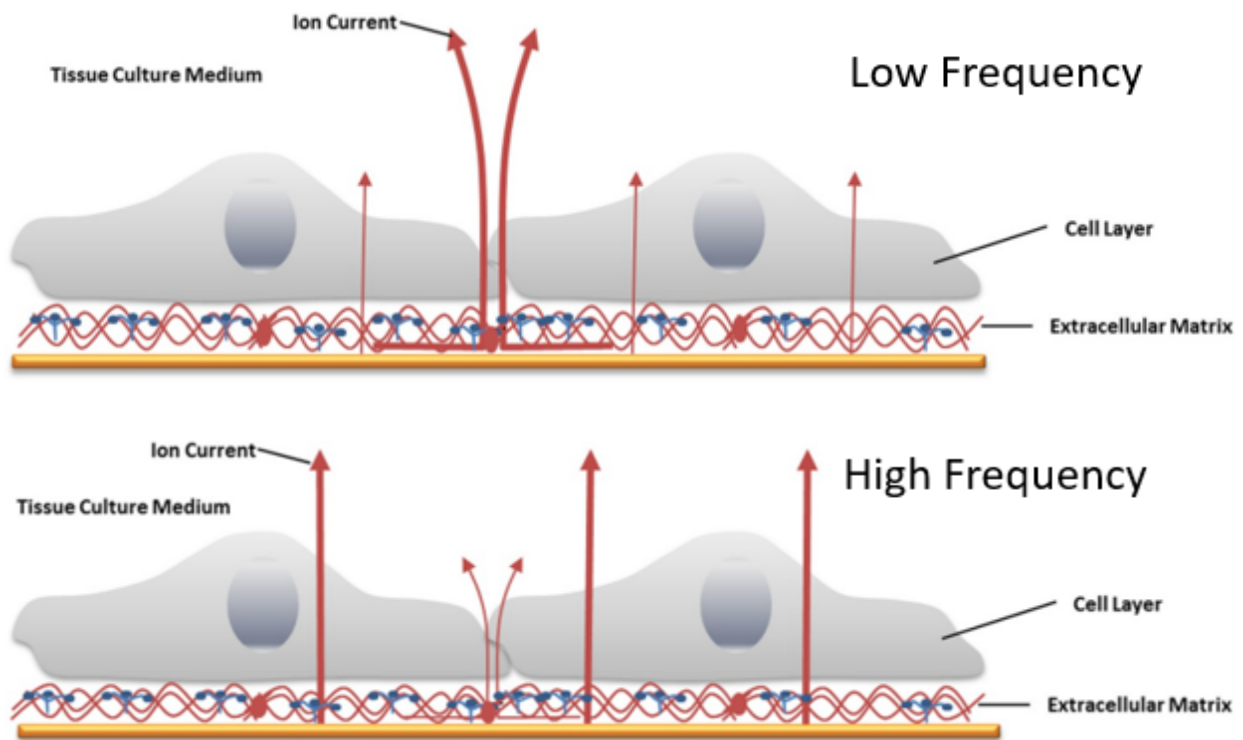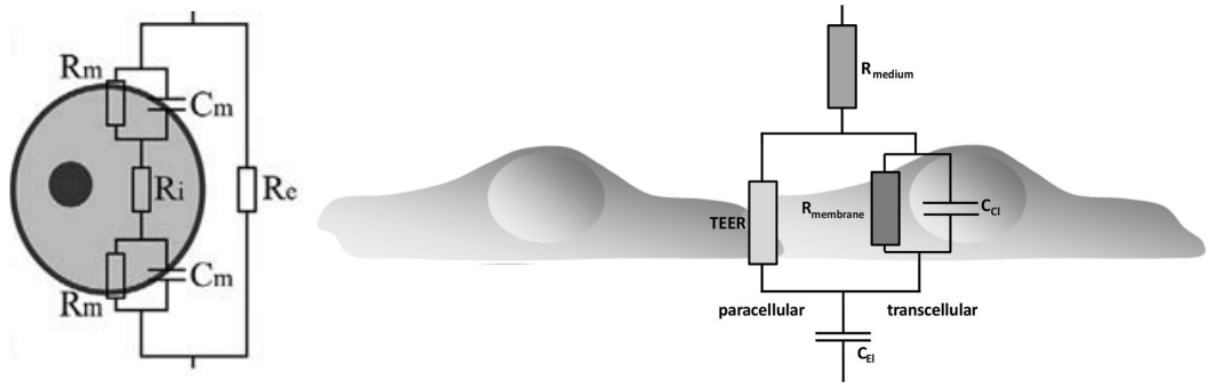
Figure 1.5 RC model of cell and frequency relationship of the monolayer. RC model of an individual cell, top left. The cellular membrane's lipid bilayer is represented as a parallel RC network of R_m and C_m. The intracellular fluid, R_i, and extracellular fluid, R_e are purely resistive [5]. In a multicellular network, the RC network is simplified to represent the paracellular and transcellular paths. Cells are simplified to a whole cell model of $R_{membrane}$ and C_{cl}. The intercellular junctions are represented by R_{TEER}. Electrode capacitance, C_{el} and R_{medium} represent extracellular impedance factors. Middle, tissue frequency response is dominated by the paracellular pathway at low frequencies. Bottom, tissue frequency response is dominated by the transcellular pathway at high frequencies [8].
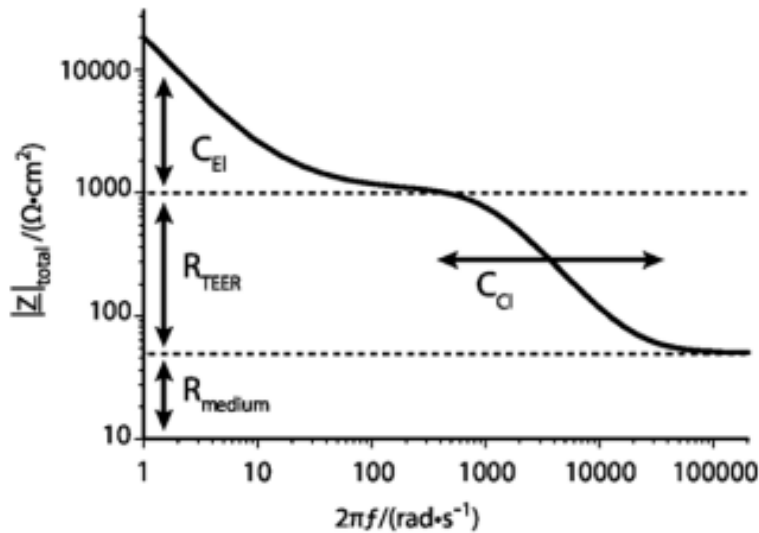
Figure 1.6 Frequency response of tissue for an excitation sweep between 1 Hz and 100 kHz. The existence of an electric double layer between the electrodes and media contributes significant impedance to the system at low frequencies. Increasing frequencies results in tissue properties dominating the impedance measurements [8].

Applications of EIS are being investigated outside of in vitro tissue cultures, and one of the biggest areas of interest is applications in mammography for breast cancer diagnostics [9-12]. These works aim to combine EIS techniques with tomographic image reconstruction to detect tumor inclusions within breast tissue. Differences within the tissue can be small and non-localized, contributing to the ill-posed nature of the reconstruction problem, and decrease spatial detection accuracy [2]. In this work, parallel electrode planes for tissue monitoring are adapted from the aforementioned literature and applied to spatial detection of conductive and insulating phantoms.

Transepithelial Electrical Resistance

Epithelial and endothelial cell lines form selectively-permeable physiological barriers (e.g., intestinal walls). These tissues are a collection of cells that form intercellular junctions across the barrier that control paracellular and transcellular diffusion and transport between the basolateral and apical sides of the cells, as shown in Figure 1.7. The behavior of the

8

intercellular junctions is of primary concern for researchers as they play a major role in the

pathology of many disorders. Barrier dysfunction manifests itself in a variety of ailments,

including psoriasis neurodegeneration and inflammatory bowel diseases like ulcerative colitis

that affect the gastrointestinal tract [14][15].
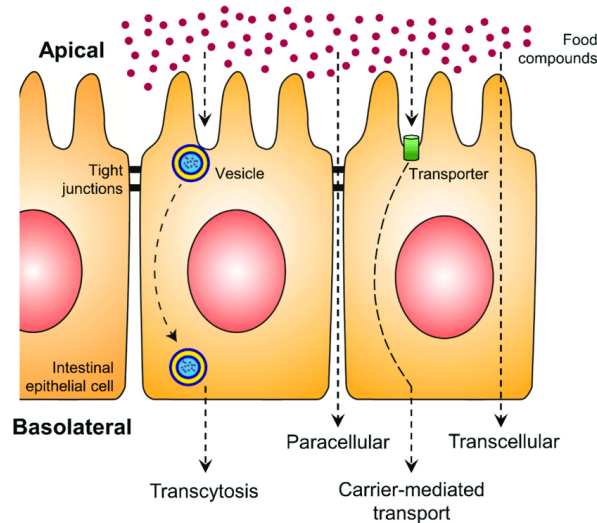
Figure 1.7 Cross sectional view of epithelial layer. Shown are the the paracellular gap that makes up tight junctions as well as the important role that epithelial tissue plays as a barrier between the apical and basolateral membranes [13].

TEER is a specific application of EIS to measure epithelial tissue grown in a monolayer.

Contrary to EIS, typical TEER systems will use a single frequency DC/AC measurement system

[15]. TEER systems provide direct measurements of characteristic electrical properties of the

epithelial layer, including cell layer confluency, thickness, tight junction formation, and

morphology [9]. In the context of this work, the traditional method of TEER measurements is a

single frequency EIS application across a monolayer of epithelial tissue focusing on real

impedance data and ignoring cellular reactance.

Researchers tend to simplify the model of a cell and cell monolayer as an RC circuit for

TEER problems. At the cell level, Figure 1.5, the membrane forms a parallel RC connection

where the lipid bilayer separates the intracellular and extracellular matrices. The intracellular

and extracellular matrices are generally represented as conductive with a resistance of R_i and R_e, respectively. Further simplification of the model for a tissue barrier can be seen in Figure 1.5. At low frequencies below 10 kHz, the conductive extracellular matrix has less impedance so the majority of the current flow is between the cells, through the resistor, R_{TEER}. At higher frequencies above 10 kHz, the capacitive layers of the cell, $C_C L$, contribute less impedance, and current flows through the cells rather than the intercellular junctions, Figure 1.5.

At low to mid frequencies, the paracellular pathway contributes significantly to the TEER measurement, Figure 1.6, so small fluctuations across the monolayer can have a significant impact on the measurement. Higher frequency stimuli have an advantage in overcoming the effects of electrode capacitive effects and revealing morphological properties of the cell-layer [16].

These junctions are of primary concern because they are largely responsible for the regulation of transport across the epithelial layer. In inflammatory diseases, these tight junctions break down and become leaky, which reduces the resistance of R_{TEER} and decreases the measured impedance of the tissue barrier. Such cellular atrophy may occur from a lack of short-chain fatty acids that act as an energy source for colonocytes (intestinal epithelia). As inflammation affects this tissue layer, more proinflammatory macromolecules exploit the paracellular pathway and have access to the basolateral compartment, further compounding the inflammatory effect in a vicious cycle [17]. Research has shown that the tissue response to inflammatory molecules can reduce TEER values as much as 37% within 24 hours [18].

In TEER applications, epithelial models are recreated with in vitro models, referred to as OoC. Figure 1.8 shows the setup of a tissue sample for TEER measurements. Cell tissue is cultured on a permeable membrane insert, commonly polyethylene terephthalate (PETE), also known as polyester, or polydimethylsiloxane (PDMS), where access to the apical and basolateral media compartments allows the insertion of chopstick electrodes, the operation of which is seen in Figure 1.8. Each chopstick will have a pair of electrodes, one for current

injection and the other for voltage measurement in what is termed a four-terminal system. A

four-terminal system is advantageous over a two-terminal system because it can reduce the

double layer capacitance of the electrodes that reduce system sensitivity to TEER

measurements at low frequencies, reducing C_{el} in Figure 1.9 [19][20][3].
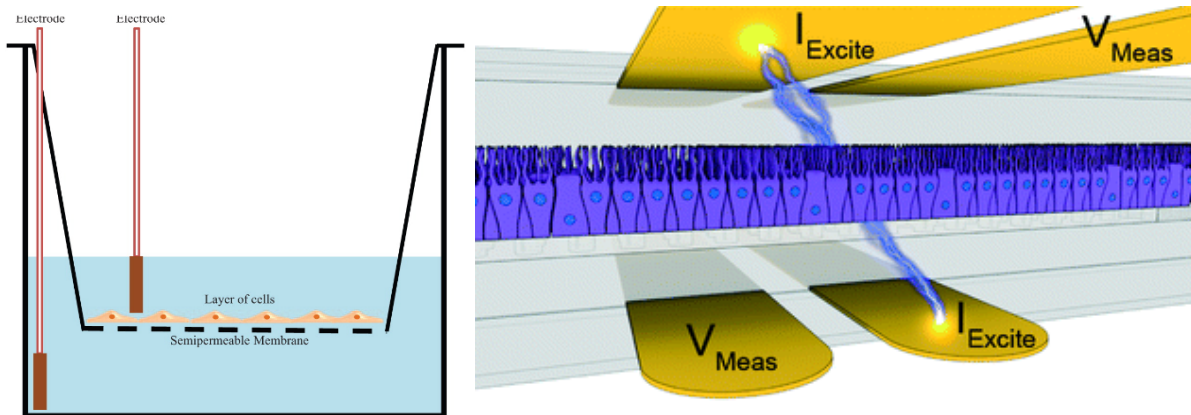
Figure 1.8 Chopstick representation of traditional EIS systems. Left, simplified chopstick setup.
Electrodes are inserted into the system to access the apical and basolateral compartments of the cell
layer [15]. Right, representation of current injection to the system across the tissue layer [21].

TEER measurements are attractive for their simplicity to set up and interpret, but they

have a few noteworthy limitations. The two main limitations are the use of chopstick electrodes

and the so-called "weakest link" rule.

TEER measurements with systems that utilize a chopstick electrode setup are prone to

measurement variability. Measurements taken in one setting are susceptible to changes from

variations in depth, the angle of immersion, and disturbances of the cells. This leads to poor

reproducibility among measurements and difficulty in comparing results between studies.

Chopstick electrodes also fail to deliver uniform current densities across larger tissue cultures,

limiting their use to often proprietary membrane inserts [14][15]. Research has been conducted

to limit the variability of chopstick electrodes with short circuited multi-chopstick systems. These

have been reported to deliver more homogenous current across membranes and lower the

impedance of the electrodes [9]. Chopstick electrodes provide rudimentary TEER measurements, but the field needs more reliable technology for accurate TEER reporting.

In a conformal tissue monolayer, different regions will have different junction thicknesses due to dome formation and cellular movement. Subregions may not exhibit tight junction formation for tissue at earlier stages, and this leads to high permeability [22]. TEER measurements are susceptible to a loss of information in these settings as the electrical resistance corresponds to the highest level of permeability in this layer, known as the "weakest link in the chain." Small imperfections in the tissue can lead to low TEER readings that are not entirely representative of the overall sample. The work of Odijik *et al*. reports that even a 0.4% gap in cell coverage can cause an 80% drop in measured TEER [23]. This demonstrates how easy and common variability of measurements are throughout the field and the need for a better method of measuring TEER.

Towards better TEER measurements, integration of multiple electrodes into a measurement model has improved spatial TEER measurements in localized areas of OoCs. Multielectrode systems offer spatial sampling of OoC systems that provide insight into tissue coverage distributed across the permeable membrane's surface. Rahman *et al*. devised a device, inspired by EIS, that would measure cellular adhesion in a multielectrode system. Measurements were taken over 70 hours, in which no replenishment of culture media was performed. To this end, they recorded an increase in impedance at the electrode surface as the cells proliferated and spread. Consequently, a decline in impedance was recorded as non-viable cells lifted off the surfaces when nutrients were depleted [16]. These measurements are reconstructed to reveal a unique impedance spectra for each electrode, which demonstrates the viability of spatial correction in TEER to reduce the weakest link effect.

The primary means of obtaining spatial information is microscopy, but the work of Renous *et al*. provides some of the earliest evidence towards the efficacy of spatially aware TEER measurement systems that scan an OoC system. The system used a four-terminal

system with two fixed electrodes and two scanning electrodes that moved across the upper channel. The scanning electrodes can be moved to any point in the channel to record impedance data. The results in damaged layers of cells indicate a strong capability to resolve distinct permeability changes across the tissue, a large advantage over traditional TEER systems [22].

Incorporating continuous measurements into a TEER system has also been used to eliminate the effects of non-conformal cell coverage. Real-time detection systems and more advanced models were designed by Liu *et al*. to measure TEER during cell proliferation. By taking calibration measurements of a blank insert and early measurements during proliferation, they were able to create a more representative "whole-region TEER model" that was able to measure the distinct stages of barrier formation between settling cells, cell proliferation, and tight junction formation after growth inhibition, which is an antiproliferative signal when critical cell density is reached [3]. The integration of continuous measurements has thus been shown to further eliminate traditional TEER measurement variability.

Another consideration of TEER systems is the impact that the permeable membrane has on measurements. TEER values are generally area corrected, but the pathways of the permeable membrane prove to be a source of non-biological variations [9]. Lo *et al*. analyzed the contribution of these membranes. Their analysis shows that TEER measurements contain contributions from the transcellular and paracellular pathways, Figure 1.7, but also a significant contribution from the current flow restriction of the permeable membrane. Epithelial cells adhere tightly to their substrate and this can double the measured TEER compared to ECIS measurements [24]. Some systems work to eliminate the effect of the membrane by integrating the membrane into their calculations. Figure 1.9, shows the model that Van der Helm *et al*. use in their model calculations. Note the addition of the electrode elements, acting as the contact impedance between the media and electrodes, as well as the permeable membrane elements that are factored into the impedance simulations [19].
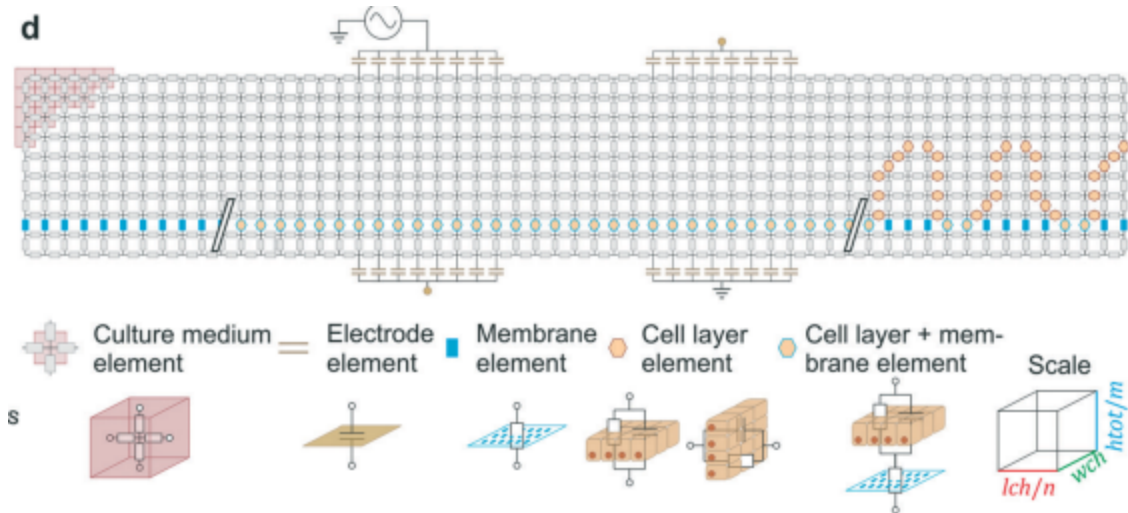
Figure 1.9 Electrical mesh model of monolayer components. Detailed models reduce error in measurements by taking all variables into account, such as electrode capacitive layers [19].

Other systems will require a calibration phase where measurements are taken across the permeable membrane without tissue to establish a baseline [14][15], yet other systems are being developed to measure epithelial cells without the membrane. Nicolas *et al*. developed a system called the OrganoPlate, which uses a gel tubule to allow for direct electrical contact of probes to the basal and apical sides of the epithelial culture.

The addition of EIS techniques to TEER systems provides a more accurate representation of TEER values. As previously described, the electrical properties of cell barriers are expressed at different frequencies, so the addition of a frequency sweep with an EIS system is one way to minimize sources of error in TEER systems. A commercially available system, cellZscope, already implements this into their measurement system.

Of the applications of EIT, in vitro tissue cultures have not been a major source of research interest. EIS and TEER are the main methods of monitoring a tissue culture over time. As the electrical properties of the culture dominate at different frequencies, it is important to sample a large frequency bandwidth of 100 Hz to 100 kHz, which requires more time per measurement frame at low frequencies [9].

The proposed device is a multielectrode, continuous impedance measurement system designed to detect spatial changes in impedance for applications in epithelial OoC studies. The device will improve upon the current state of the art in two ways. Firstly, through tomographic imaging, researchers can use this device to spatially understand the development of an in vitro tissue culture over time. Secondly, the distributed design of the device is intentionally compact to work within an incubator to reduce environmental impacts on the culture-under-test (CUT) such as temperature fluctuations or contamination. This will eliminate the need to remove cultures from an incubator to take measurements during the duration of tissue development.

Chapter 2 - Transepithelial Electrical Resistance System Hardware Design

Classical designs of TEER systems utilize a pair of chopstick electrodes to separate the current drive and voltage sense electrodes. Commercially available systems, like the EVOM TEER meter Figure 2.1, require the electrode blades to be inserted into the well plates to allow access to the apical and basal surfaces of the CUT. Higher quality systems provide multiwell measurement in parallel, like the cellZscope or OrganoPlate, with similar chopstick electrode systems in fixed positions.
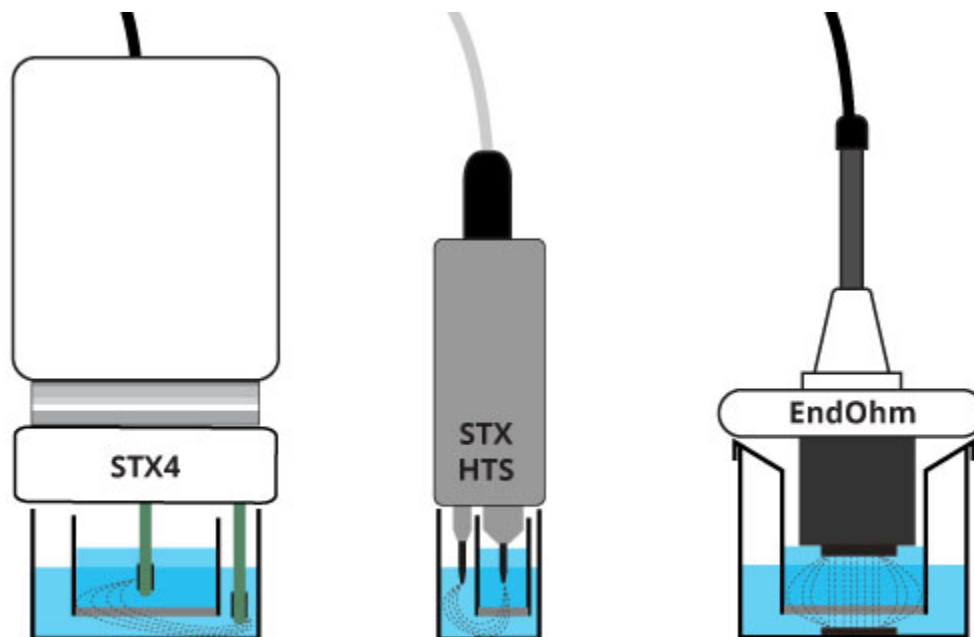
Figure 2.1 EVOM Chopstick electrode Variants.

Through high sample rates as low as 1 second per well and robotic automation, these systems make sampling tissue resistance in multi-well plates convenient, but these systems are still susceptible to the weakest link effect. By increasing the coverage area and quantity of electrodes in the system, the proposed TEER system will offer higher sample accuracy and will offer insight into spatial coverage densities across the culture.

In a large electrode system, an ideal setup would have a current drive and voltage sampling circuit at each electrode. The design footprint is a major consideration as the proposed

system is intended to operate within an incubator. Distributed systems accomplish two things. First, electronic components mounted close to electrodes minimize capacitive effects in leads, a significant source of measurement error. Error levels have been reported to be less than 0.1% with distributed systems [25]. Second, it reduces the overall footprint of the design, which is easier to manage and integrate into bigger experiments. The proposed design is a fully distributed system occupying a footprint of 12.7x15.2 cm^2, Figure 2.2, with future optimizations minimizing the size further. Given the size and complexity of an ideal circuit, multiplexers offer the advantage of current injection and voltage measurement selection at any electrode with minimal hardware.
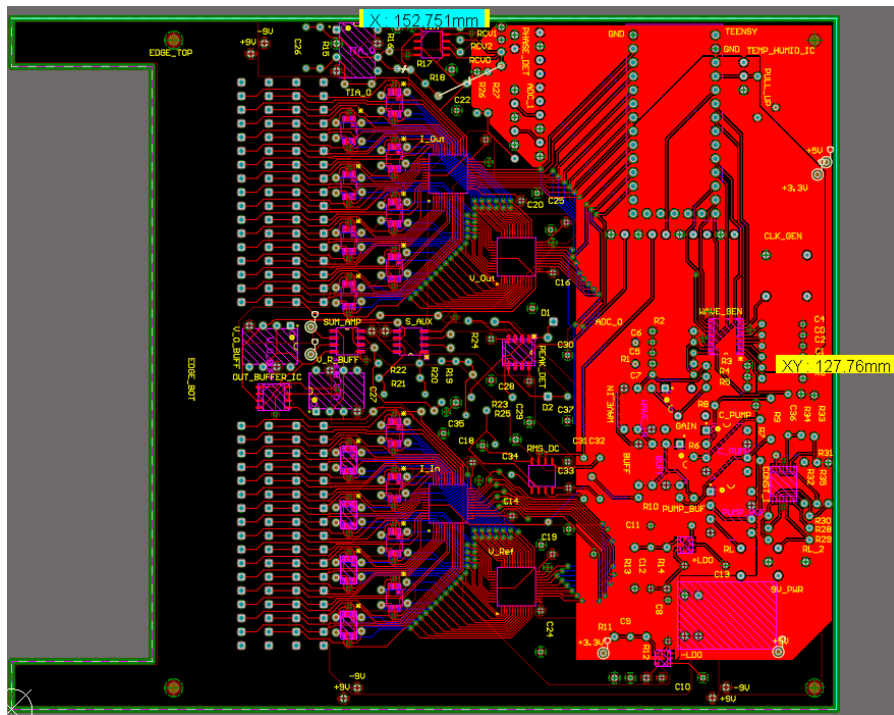
Figure 2.2 Second prototype of TEER system on a PCB. The system is distributed on a four-layer PCB to minimize the overall footprint and allow for flexibility during debug and redesign with multiple test points and redundant through-hole connections for testing alternate hardware.

The proposed system will utilize parallel electrode plate arrays with electrode configurations between 8 and 64. The purpose of which is to identify the ideal quantity of electrodes required for the most significant improvement in image reconstruction versus

measurement time. As was the case for cylindrical systems in Figure 1.3, an increase in sensing electrodes has an inverse relationship with the reconstructed image. Higher electrode counts lead to minimal improvements in image quality, while the frame rate decreases quadratically. The increase in complexity serves to validate the system under a progressively complex electrode system to find the right balance and to allow for future reconfigurations.

A high-level description of the intended use of the system is shown in Figure 2.3. For two parallel electrode plate arrays, an electrode on each plate is selected as a current carrying electrode. For each current electrode configuration, a voltage measurement is taken at each other electrode. Once each current carrying electrode pattern is completely measured, then one frame of the image is complete. Consider a system with N electrodes on the top and N electrodes on the bottom plates. There are N^2 current patterns, and for each current pattern, there are $2(N-1)$ measurements. For a complete frame, $N^2(2N-2) = 2N^3 - 2N^2$ measurements must be taken. In a 4x4 electrode configuration, 96 measurements are needed, and a 32x32 electrode configuration would need 63488 measurements for a single frame. Time optimizations in firmware are discussed later that can minimize the time required for each frame acquisition, but the bulk of the minimization will be determined by EIDORS simulations to determine the tradeoff of electrode count versus image quality, discussed in Chapter 3.
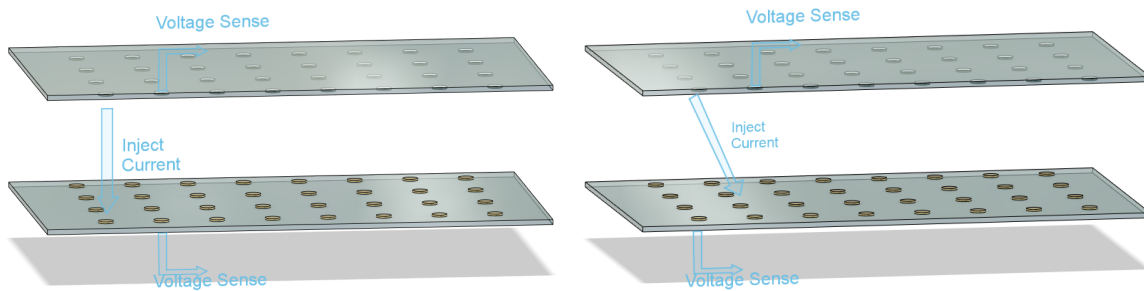
Figure 2.3 Current injection and voltage measurement technique on parallel planar electrode arrays. Voltage measurements are ignored for current carrying electrodes to minimize electrode capacitance in impedance measurements.

Microcontroller

Control of the system was accomplished with a Teensy 4.0 USB development board from PJRC with an ARM Cortex-M7 proccessor. This board has 40 digital I/O pins making it ideal for control of peripheral devices with digital inputs, like the programmable frequency generator AD5930, and analog to digital converters ADS1115. The board has ports for both SPI and I2C communication protocols, allowing flexibility for interfacing multiple peripherals. 5 V and 3.3 V pins allow this board to power each component in this distributed design.

Firmware was designed for the development board to control the two main TEER measurement routines, a process described in Figure 2.4. The firmware calibration process is highlighted in red. This phase sets the minimum settling time delay based on the minimum measured voltage value for a representative selection of channels. The highlighted blue section is the main measurement phase that samples each electrode voltage for each current injection profile. Completion of this function sets the minimum settling time and toggles the CTRL pin to increment the frequency profile stored in the programmable frequency generator AD5930.
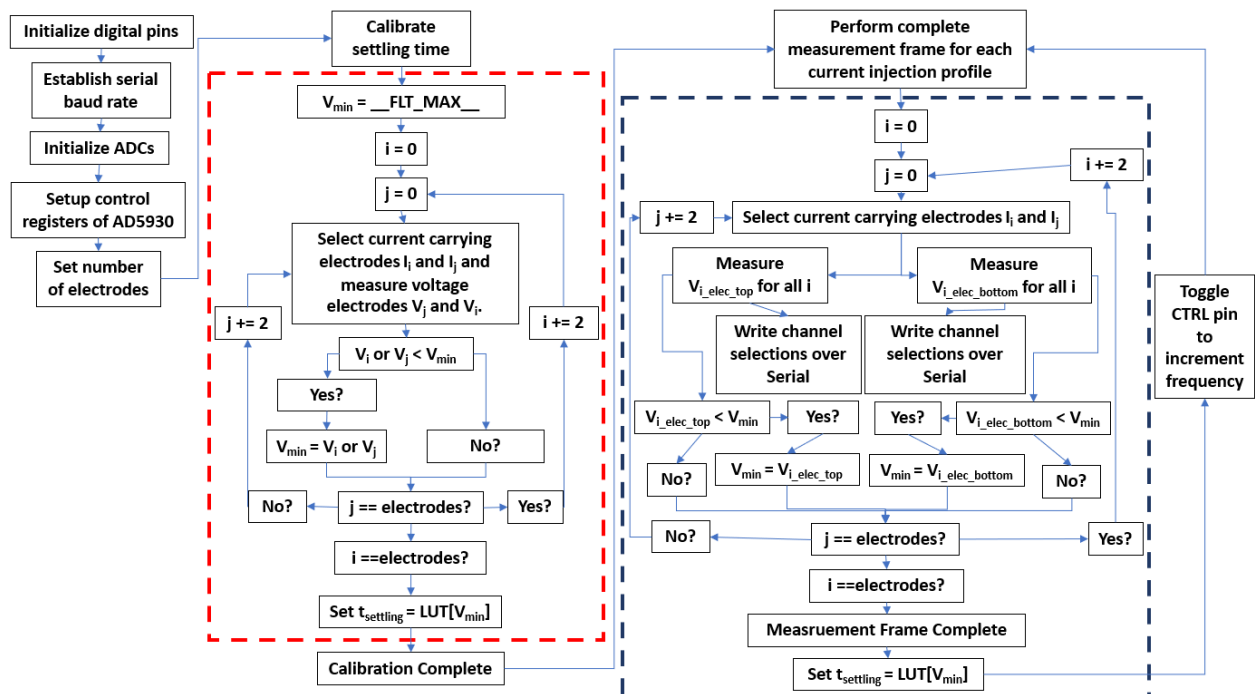
Figure 2.4 Firmware flowchart for setup and measurement.

The Teensy development board communicates directly to a host PC. Once the firmware iterates through the setup phase, it will print continuous channel configurations with measurements over a serial connection. Serial data is collected externally through a Python script that converts the data into a reusable CSV file format that is in turn read into the MATLAB script for reconstruction. At the present time, these operations are done manually by the system operator, but future designs will automate this task.

Programmable Frequency Sweep Generator

In the electrical model of the epithelial cells, different properties of the tissue are expressed at different frequencies. To increase the resolution of the data, the system is designed for EIS, implementing a frequency sweep of the chamber. For this, we will need a Voltage Controlled Current Source (VCCS) that makes use of a waveform generator and a Howland current pump. The purpose of the waveform generator is to produce a constant voltage signal with steady amplitude over the entire frequency range [26].

To accomplish this, we employ an AD5930, a monolithic programmable frequency sweep generator, used in biological EIT applications [6][27]. This is a low cost IC component that is capable of generating output frequencies up to 25 MHz. It can be operated off the 3.3 V or 5 V pins, but uses the 3.3 V to reduce power consumption and heating. The 3.3 V pin has a maximum output current of 250 mA, well below what is used by the additional circuitry. The microcontroller is easily programmed with a three wire SPI interface.

Firmware was designed for this project to operate over the full frequency sweep from 100 Hz to 100 kHz, with 1 kHz increments where the first increment is 1.1 kHz [37]. Frequency generation is a critical design decision. The circuitry interfaces into the balanced resistor bridge of the Howland current source, so a minimal source impedance is required to prevent imbalances. A direct digital synthesis (DDS) device like the AD5930 fulfills this requirement and is an ideal component to interface into the Howland current source [28]. For details on setting up the starting frequency F_{START}, please refer to "AD5930 F_{START}" in the Appendix.

The AD5930 offers significant versatility with the CTRL pin that allows external control over frequency increments. Managing the timing of the hardware with the proper settling time of four multiplexers, the RMS-to-DC converters, and the peak detector proved to be difficult, compounded by the increment interval programmed into the control register, t_{int}. Through external toggling of the CTRL pin, the firmware could dynamically sample the voltages and change the rate of data acquisitions when frequencies are higher. As lower frequencies require more time between measurements, dynamically sampling and comparing the input voltage allows the system to choose the minimum required time to perform a stable measurement. The slowest component is the RMS-to-DC converters, which have frequency and input level dependent settling times. Once a voltage value is held constant on the output, it is sampled, and the frequency profile is incremented. This happens at a faster rate as frequencies increase and signals settle faster across the averaging capacitor, C_{AV}, on the RMS-to-DC converters.

The control register of the AD5930 is programmed first, the exact settings can be changed with a rewrite to the control register, which functions in the same way as toggling the INTERRUPT pin. Two consecutive writes are required to program the control register, in which time the binary values 0b0000_0110 and 0b1111_1111 will be stored in the control register address, 0b0000. The rest of the control register data indicates that the F_{START} and Δf registers will be configured as two 12-bit registers of MSB and LSB data to allow easier reconfiguration during operation, as 24-bit rewrites have more resource overhead. The DAC is enabled on the device to ensure a full output sweep is created. This increases power consumption, but is essential for creating a sinusoidal signal. SINE/TRI is also set to 1 to enable sinusoidal signal output. The MSBOUT pin is unnecessary for testing and set to 0. The system does not use a digital output waveform, so this value is set to 0. If a square wave output is desired, similar to that used by an EVOM device, this bit can be set to 1. The output is expected to be continuous, so CW/BURST is set to 1. INT/EXT BURST and INT/EXT INCR are both set to 1 to allow external frequency increments from the CTRL pin. MODE is set to 0 to ensure the proper shape

21

of the waveform increments is sawtoothed rather than triangular. SYNCSEL and SYNCOUTEN are both set to 1 to allow for more in depth debug of the state of the waveform. If the system was not controlled externally, this would be a useful setting to allow sampling of the sweep state. For more details on setting the registers, see [27]. The frequency sweep is set from 100 Hz to 100 kHz, with step increments of 1 kHz to isolate the frequencies dominated by cellular electrical properties, shown in Figure 1.6. This is intended for future applications in OoC tissue cultures to measure the response relevant to different tissue properties. The validation phase of the system limits the frequency to 1 kHz by restricting digital toggling of the CTRL pin.

Voltage-Controlled Current Source

A prerequisite of an EIT system is a precision current or voltage source. There are several reasons for this necessity, one of which is safety. A constant current source applied to a living subject must strictly operate within a range of 0.1-10mA to comply with safety standards defined by IEC 60601-1 [1][26]. Lower currents are used in conjunction with low frequencies, and in EIS specific works, the current may be even lower at 10 µA [3][19][22][29]. Another factor in the consideration of precision VCCS is the ill-posed nature of the problem. Constant sources keep measurements consistent throughout the electrode sweep and reduce the need to account for measurement inconsistencies across the system. There will be inconsistencies in the operation of the VCCS and designers may work around this by adding circuitry to measure the current source in conjunction with the voltage and correct the results to be ideal. Dynamic methods have been reported to adjust output according to measured current or feedback adjustments to keep the current source ideal [25].

There are many ways to design a VCCS, but the consensus among literature is the implementation of a Howland Current Source. At its simplest, a Howland current source utilizes a single op amp with a balanced resistor bridge of four resistors. When considering a VCCS, the most important factors for enhancing sensitivity and accuracy are the SNR and the stability of the current source. For an analysis of other VCCS designs, see [26].

The Howland current source can be seen in Figure 2.5. To understand improved

Howland current sources, it is necessary to understand the operation of the unmodified design

through circuit analysis.

Solving for i_o:

$$i_o = Av_i - \frac{v_L}{R_o},$$

where

$$A = \frac{1}{R_1}, \quad R_o = \frac{R_2}{\frac{R_2}{R_1} - \frac{R_4}{R_3}}.$$

Under ideal conditions, $R_o \to \infty$, given the conditions of the balanced bridge, $\frac{R_4}{R_3} = \frac{R_2}{R_1}$. Thus,

the output current i_o is independent of the load, R_o given a balanced resistor bridge [30].
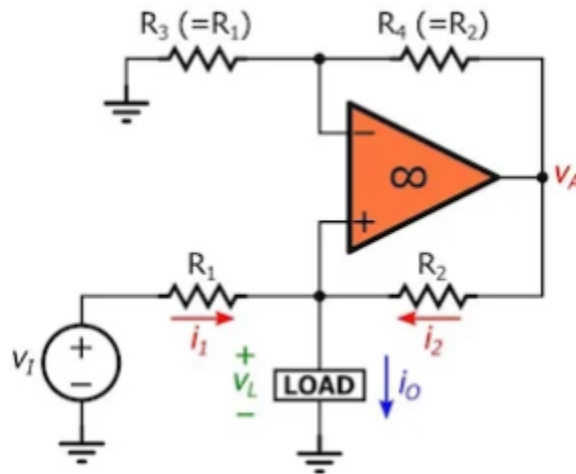
Figure 2.5 Basic Howland current source analysis schematic [30].

In the works of Tucker *et al.* and Khalighi *et al.* it was found that an improved Howland

current source could be designed with the addition of a single resistor to the positive feedback

network of the resistor bridge. The addition of R2 in Figure 2.6 reduces power consumption in

the circuit which reduces heating imbalance of the resistors that make up the balanced bridge

and compensates for resistor mismatch in the resistor bridge [26][28][31]. For additional

information on the effects of resistor mismatch, see [30]. The primary method of handling

resistor mismatch is with the addition of a potentiometer across the output of the primary op amp. The addition of this potentiometer allows users to quickly adjust the potentiometer and balance the bridge. Another, simpler method is hand sorting of resistors based on measured value. This method was reported to reduce differential common-mode voltage from 42% to 8% and was conducted in this work [25].

The analysis of the improved Howland current source is identical under the condition

$$\frac{R_4}{R_3} = \frac{R_2 + R_5}{R1} .$$
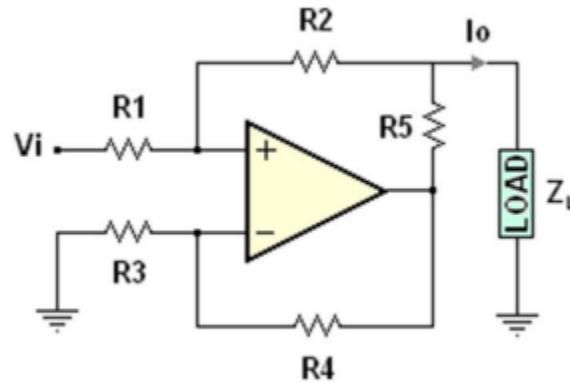
Figure 2.6 Enhanced Howland current source. Note the addition of a single resistor R_5 that is used to reduce heating imbalance of the balanced resistor bridge [26].

Outside of simulation, the actual performance of the improved Howland current source is governed by the capability of the op amp. The maximum load that the network can drive is given by

$$Z_L^{max} = \frac{|V_L|}{I_L} ,$$

where $|V_L|$ is the maximum load voltage where the current source works linearly and is given by

$$V_L \leq V_{sat} - \frac{R_2 + R_5}{R_1} \cdot V_i ,$$

where V_{sat} is the saturation voltage of the op amp [26][28].

24

Further improvements can be added to the Howland current source. It was shown by Khalighi *et al*. that a dual, triple op amp based floating current source could supply constant current under increased load at frequencies above 100 kHz. This dual configuration also demonstrated improved output impedance values of 1.06 MΩ at 300 kHz, nearly a ~3.5x increase compared to that of the improved Howland current source in Figure 2.6. It was determined that this design would occupy too much area on the PCB and other methods were viable to increase the output impedance. The work of Tucker *et al*. demonstrated that the addition of a few passive components in the improved design was enough to increase the output impedance to 3.3 MΩ at 455 kHz. The choice of VCCS for this work was an improved triple op amp Howland current source reported by Khalighi *et al*., given the simplicity of the circuit and ease of adding passive components to increase the output impedance.

Ansory *et al*. documented the hardware design and software development in a reproducible manner that served as a model for initial development of a Modified Howland current source [32]. A notable flaw with the system was the VCCS could not handle the loads of the proposed system. Sapuan *et al.* described a similar VCCS but used a voltage buffer before the VCCS double op amp to keep the AC current constant and isolated from the frequency sweep generator circuitry of the AD5930. The benefits of this VCCS are a wider frame of stability regarding frequency and load, detailed in Appendix Figures A.2-A.5 [33]. After rigorous testing, this design was abandoned and exchanged for the triple op amp model due to large swings in the output current that would draw too much power. Simulations showed ideal operation of the Modified Howland current source, but implementation always failed, regardless of interchanged hardware. This caused more current to pass through the multiplexers than was intended, in turn drawing current from the +2.5 V LDO that would make its operation unstable and decrease the dynamic range of the multiplexers.
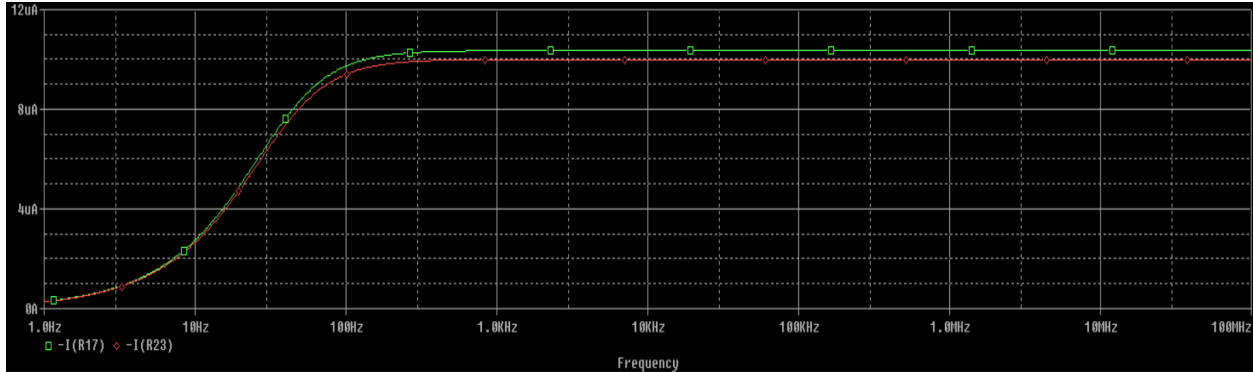
Figure 2.7 A comparison of the simulated output current of the two VCCS. The green trace is the model reported by Sapuan *et al*., and the red trace is the triple op amp model. Both show ideal output current across the entire frequency range.

There have been other designs that optimize system throughput with a dual or multiple source, such as the popular ACT3 system [34], or injecting an AC current composed of multiple frequencies and breaking down the measured voltage with Fourier decomposition [35]. At the cost of complexity and extra hardware overhead, it was decided to keep the current source as single ended in this work.

For the single-ended current source, one terminal was tied to a virtual ground at the input of the transimpedance amplifier (TIA). Boone *et al*. noted significant measurement errors from common-mode signals that arise between the measurement electrodes and the reference electrode from the complex current flow around the impedances in the body. This is a particularly significant source of error, and although an ideal floating source would introduce no common-mode signal, a real floating source would still introduce common-mode signals. For this reason, it was determined that the simplicity of the single-ended source with a terminal at zero volts was sufficient for the design. Similar to the functionality of the ACT3 system, the virtual ground is established first in each multiplexing iteration. This serves to gate the output current which ensures more accurate voltage measurements [34].

The triple op amp Howland current source was validated first through simulation. The design was created using the default op amp model in PSPICE. The resistor bridges are set to

26

represent an ideal system with a balanced bridge consisting of 2 kΩ resistors as shown in Figure 2.8. The magnitude of the output current was maintained at 10 µA by setting R_{29} to 30 kΩ to comply with values reported in [19][22][29]. Resistors R_3 and R_4 are chosen to satisfy a gain required to amplify the output of the waveform generator to 1 V. This is done to allow ease of amplification throughout the system. In the physical design, these components are replaced with potentiometers to allow for reconfiguration of the current source as needed to balance the resistor bridge.

In the simulation, the TIA was added at the output of the load for direct comparison to the same system that was prototyped on the breadboard. Similarly, the output buffers that sample the voltage across the load resistor, instrumentation amplifier, and peak detector were added to more closely simulate components in the immediate design.
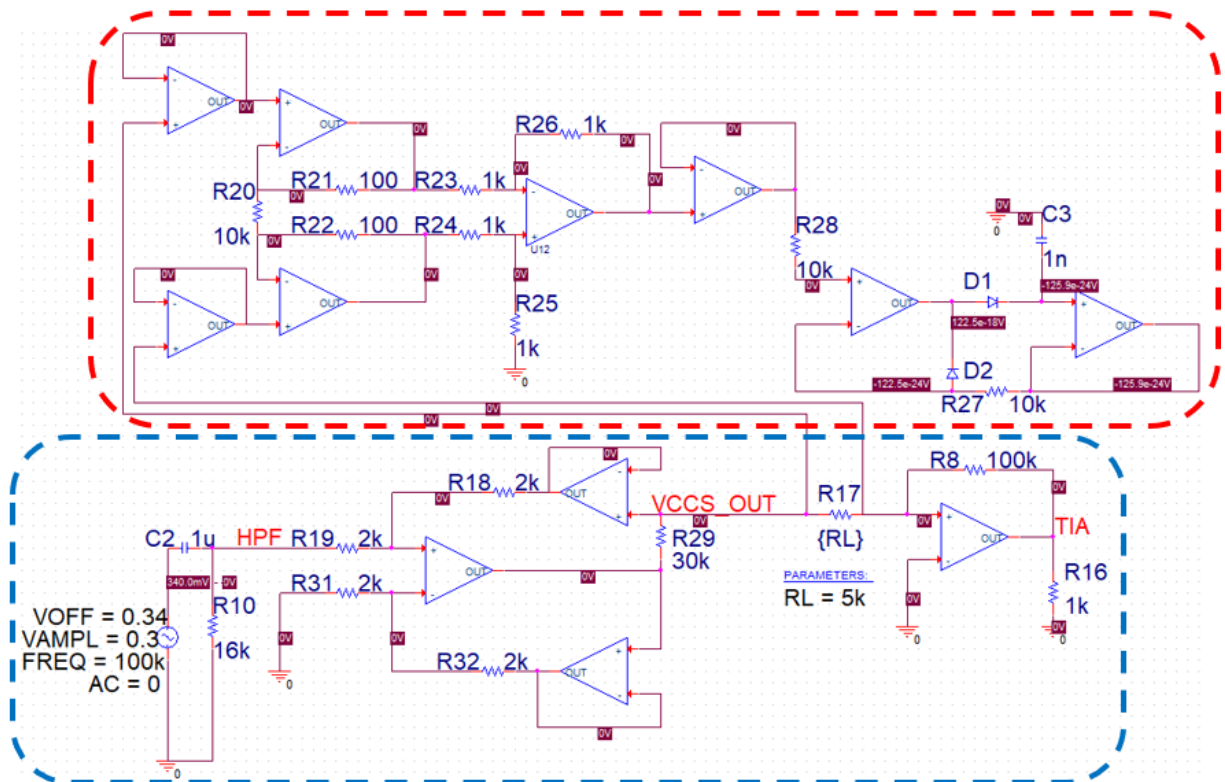
Figure 2.8 Schematic representation of the current injection and voltage sampling circuits. PSPICE model of triple op amp current source (blue). Schematic includes connections to a TIA, as well as a differential measurement across the load converted to a digital value by a peak detector (red).

27

Resistive load values were tested with values of 100 Ω, 1 kΩ, 5 kΩ, and 10 kΩ to

validate the design presented by the work of Khalighi *et al*. and ensure the system worked at

higher resistive loads that were performed in their testing. The frequency band of 1-100 kHz

was similarly tested to ensure that the system suffered minimal performance issues, see Tables

A.1-A.4 in the Appendix.

In a similar theme as many of the subsystems on the PCB, the VCCS was designed with

a primary system of 3 LM741 op amps to model the functional architecture during the

breadboard validation phase. A redundant system using an ADA4062-4ARUZ quad op amp

SMT IC was added for testing other VCCS in the event the triple op amp model failed. This SMT

device also reflects the actual footprint that would replace the bulky through-hole LM741 op

amps in future iterations of the device. 2 kΩ resistors were hand sorted for the resistor bridge

and R_{29} was selected to be 30 kΩ from equation $I_L = \dfrac{R_2}{R_1 \cdot R_5} \cdot V_i$ from [26]. With an input

connection from the AD5930 programmable frequency sweep generator, both VCCS circuits

output 10 µA of current for test loads. Loads are verified with onboard potentiometers that are

variable between 1-10 kΩ.

Analog Multiplexers

Signals are efficiently multiplexed through four ADG732, 32 channel analog multiplexers.

Firmware controls the switching behavior through a binary selection of the five address lines, A_0,

A_1, A_2, A_3, A_4 and latches by the $\overline{WR}$ pin. The multiplexers work equally well to multiplex or

demultiplex the current and voltage on 32 different electrodes. For proper transmission of the

AC signals, the multiplexers run on a +/-2.5 V dual supply [36].

There are disadvantages to using an analog multiplexer such as the ADG732. In high

precision applications, the channel mismatch limits accuracy at high frequencies where very

small impedance measurements would be expected [35]. The nature of the break-before-make

switching action also imposes the need for settling time on each transition, to allow for floating

voltages on each channel to settle, as discussed in the RMS-to-DC converter section.

Voltage Buffers

To increase the input impedance of the measurement electrodes, voltage buffers are

added as close to the electrodes as possible. The proximity in the proposed PCB system also

reduces the length of high impedance paths [38][39]. For this design, AD8244 Precision FET

Input Quad Buffers are used to minimize the PCB footprint of the 64 buffers and for the high

input impedance of 10 TΩ that would minimize the current on the input pins [40].

Power Supplies

Multiplexers operate off of a +/-2.5 V voltage rail. This requires two low dropout voltage

regulators (LDOs), TPS72325QDBVRQQ1 and TPS73225MDBVREP. All op amps in the design

operate off of a +/-9 V power supply from a 410-293-B Digilent PowerBRICK that takes a 5 V

input from the Teensy development board [41-42].

Measurement Circuit

The voltage measurement was handled in two ways during development. The first

method used a differential amplifier stage cascaded into a precision peak detector stage to

replicate common methods seen in similar devices [46]. It was ultimately decided that the

differential amplifier and peak detector were not needed. A differential amplifier is useful when

measurements are done in a standard pattern, such as that of the adjacent method in cylindrical

EIT systems. In the proposed planar system of electrodes, it was unclear how those

measurements would relate to the EIDORS software and the proposed Python reconstruction

script.

RMS-to-DC converters replaced the differential amp, peak detector circuit. RMS-to-DC

converters were chosen to eliminate the risk of errors from signal droop across the capacitor

(C_{HOLD}) in Figure 2.9. At high frequencies, the droop becomes significant in the precision peak

detector and the simulated design has a minimum measured value of 0.341 V, or a 66%

measurement error at 100 kHz. Given the timing challenges in the design, it was determined that eliminating error associated with this droop was necessary. Increasing C_{HOLD} to 10 µF decreased the error to 62% and it was determined that the diodes would be unable to handle the higher frequency ranges of the TEER system altogether.
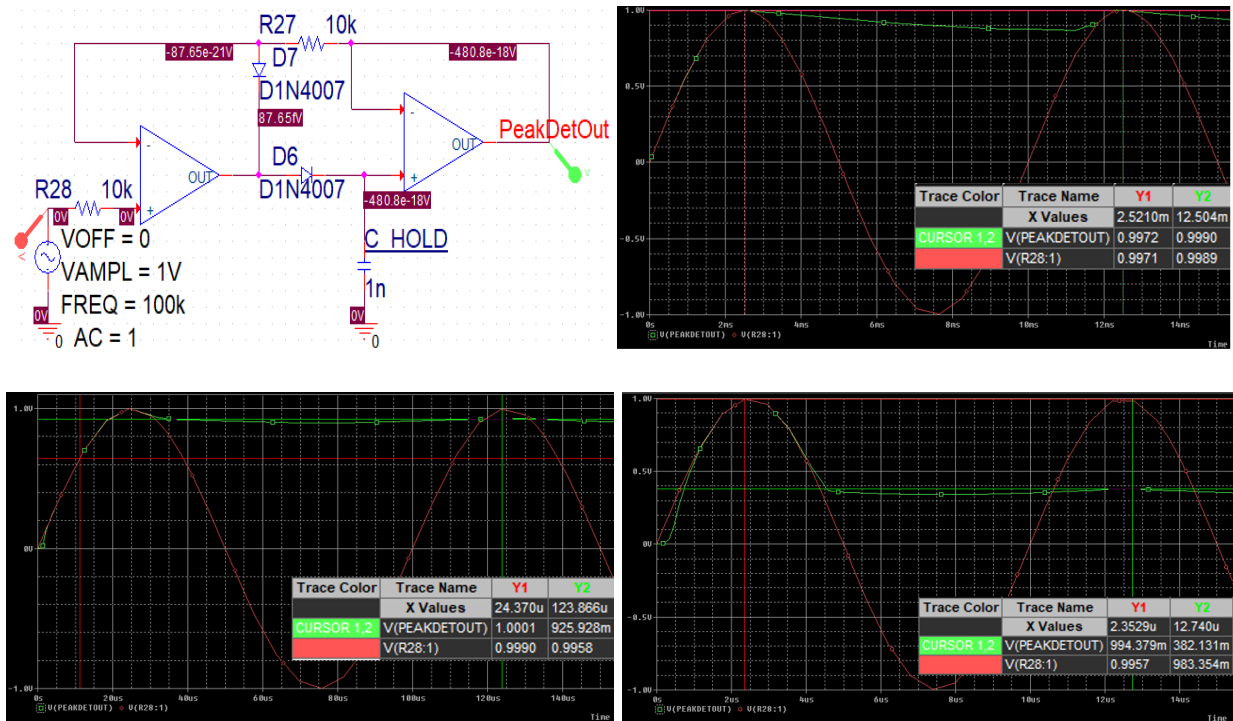
Figure 2.9 Peak detector circuit analysis. Peak detector circuit, top left, with simulated droop at 100 Hz, top right, 10 kHz, bottom left, and 100 kHz, bottom right. Significant droop is detected at high frequencies, increasing the measurement error.

An RMS-to-DC converter will give the RMS value of a sine wave with high consistency. For this design, the voltage signals are first passed through bandpass filters and amplified with a non-inverting amplifier, Figure 2.10, to an appropriate V_{RMS} before acting as inputs to two AD736, True-RMS-to-DC Converters. The bandwidth of the bandpass filter is 2.99996 MHz, with a low frequency cutoff point of 40 Hz and a high frequency cutoff of 3 MHz. The low frequency cutoff at 40 Hz was carefully selected to maximize the attenuation of 60 Hz, which is the most likely frequency of noise in the system, while minimizing the attenuation of the signal at the lowest measured frequency of 100 Hz. To increase the roll-off of the bandpass filter, a 6th-order

Butterworth Filter was designed with a Sallen-Key combination of a 3rd-order high pass filter cascaded into a 3rd-order low pass filter. The high frequency cutoff is similarly selected to minimize attenuation of a 1 MHz signal, to allow for flexibility in future designs that require a higher frequency range. Finally, the signal is amplified through the non-inverting amplifier stage with a gain of 210. The feedback resistor in the amplifier stage is implemented with a 200 kΩ potentiometer to allow flexibility in the design and testing phases while saline solutions and permittivity phantoms are used instead of epithelial cell cultures. It is important to note that saline solutions have their limitations since they may corrode electrodes and their conductivity is highly temperature sensitive [47].
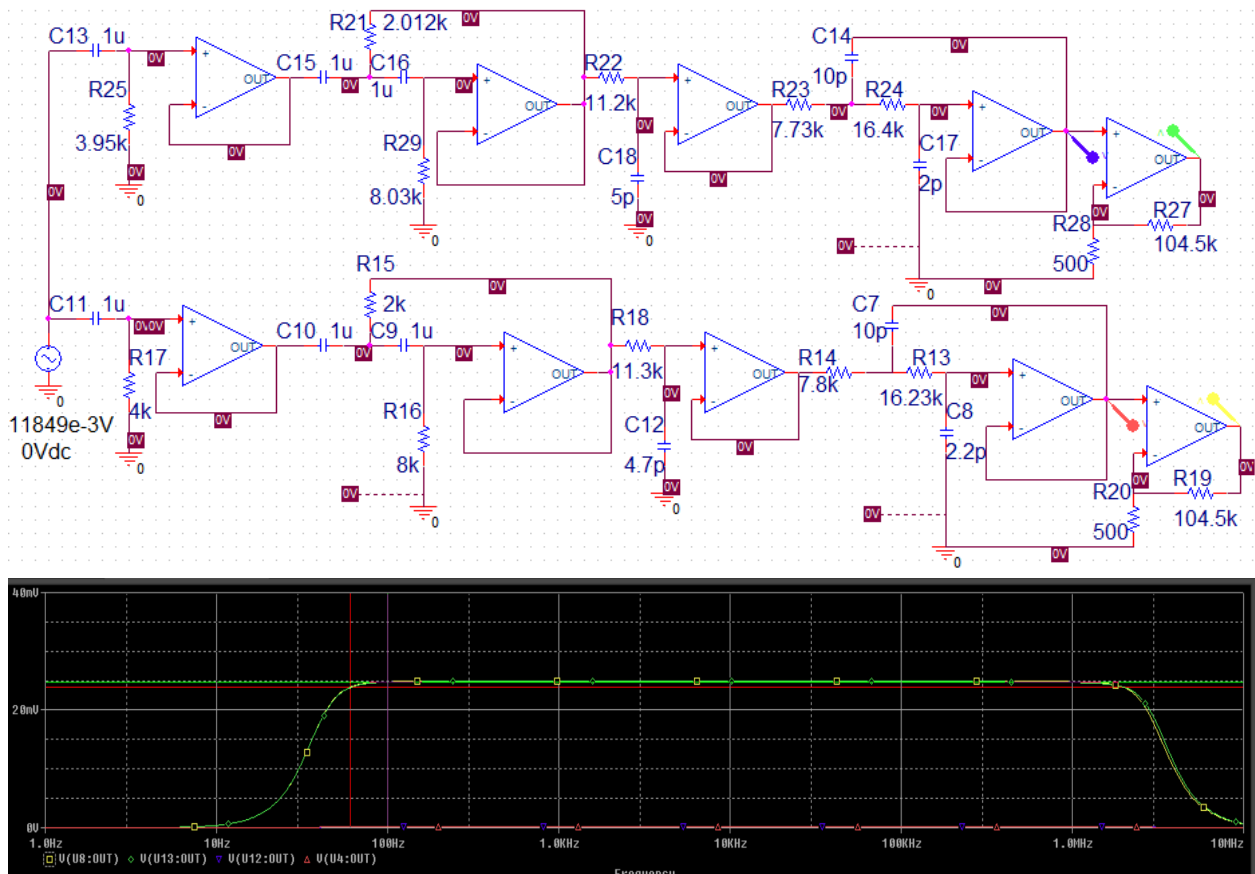
Figure 2.10 6th-order Sallen key Butterworth bandpass filter. The filter is designed with cutoffs at 40 Hz and 3 MHz (top). Simulation of bandpass filter with ideal and real electrical components show little difference in passband (bottom).

In a TEER system, impedance measurements are area corrected to describe a resistance across a surface area or $\Omega \cdot cm^2$. To predict the values that the system must be capable of measuring, it is necessary to first consider the expected TEER values of a healthy epithelial barrier and a leaky epithelial barrier. For Caco-2 cells, the generally accepted values are 50-100 $\Omega \cdot cm^2$ for leaky layers, 300-400 $\Omega \cdot cm^2$ for intermediate cell layers, and 2000 $\Omega \cdot cm^2$ up to even 4000 $\Omega \cdot cm^2$ for healthy barriers [15]. It is possible to calculate the expected measured values for V_{MIN} and V_{MAX} corresponding to a leaky tissue layer and tight tissue layer, respectively.

$$TEER = A_{surface} \cdot R_{NET}$$

$$A_{surface} = 15.4\,mm \cdot 27.4\,mm = 421.96\,mm^2$$

$$4000\Omega \cdot cm^2 = 4.2196\,cm^2 \cdot R_{max}$$

$$R_{max} = 947.9572\,\Omega,$$

where $A_{surface}$ is the area of the electrode planes and R_{net} is the real resistance of the tissue and media. 15.4 mm and 27.4 mm are the width and height, respectively, of the proposed TEER electrode array, in Appendix Figure A.6.

Similarly for 2000 $\Omega \cdot cm^2$, $R_{max} = 473.979\,\Omega$, and a minimum measured value of 50 $\Omega \cdot cm^2$ for a leaky layer, $R_{min} = 11.849\,\Omega$. The expected voltage range of these TEER values given a current of 10 µA from Ohm's Law, $V = IR$, $V_{max} = 0.0094796\,V$ and $V_{min} = 0.00011849\,V$. These values are lower than what the ADS1115 ADC can measure with high accuracy, so gain is chosen to set them at appropriate levels. The current maximum voltage measured in the system is 1.8 V from the AD8302 V_{MAG} and V_{PHASE} [48], so a maximum voltage of +/-2.048 V can be measured by the ADC. The effect of this voltage cap is a minimum voltage per bit calculated by $V_{bit} = V_{max}/2^{15} = 62.5$ µV/bit, where the ADC has a 16-bit resolution, with the MSB acting as a sign bit, so an effective 15-bit resolution. Setting the Programmable

Gain (PGA) of the ADS1115 to GAIN_TWO also sets the upper limit to the gain of the measured TEER voltage signal.

$$\frac{2\,V}{0.009479572} = 210 = Gain$$

$$V_{min} \cdot 210 = 0.024864\,V, V_{max} = 2\,V$$

The AD736 was selected because it is a monolithic true RMS-to-DC converter with high precision and low power consumption. The device has a low error rate for waveforms with crest factors between 1 to 3.

$$CrestFactor = \frac{V_{PEAK}}{V_{RMS}},$$

which is 1.4142 for sine waves. The device is AC-coupled to handle low input signal levels, as low as 100 µV. The AD736 is also reconfigurable to measure the average rectified value, the absolute value, or the true RMS-to-DC value of an input signal. The device has low reading errors over the majority of the frequency range of the proposed system, with a 1% reading error exceeding 10 kHz for input amplitudes between 20 mV to 1 V$_{RMS}$ or for the systems sinusoidal inputs, $V_{PEAK} = \sqrt{2} \cdot V_{RMS}$, 28 mV$_{PEAK}$ to 1.4142 V$_{PEAK}$ which covers the range of expected TEER values [49].

The AD736 is designed to utilize the low impedance input on pin one to take advantage of the wide range of input signal levels with low error. Figure 2.11 shows that a connection to pin one will allow high precision measurements of the TEER input signal from 20 kHz at the lowest expected TEER value to over 100 kHz for the maximum expected TEER input signal. This does leave room for conversion errors at lower input levels, which will all still be under 10% at 100 kHz.
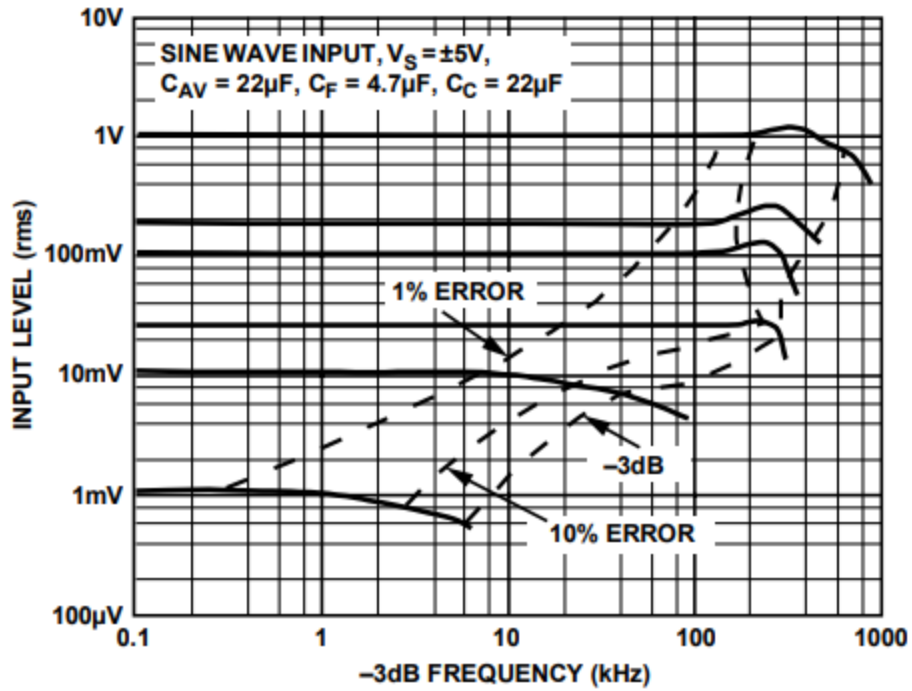
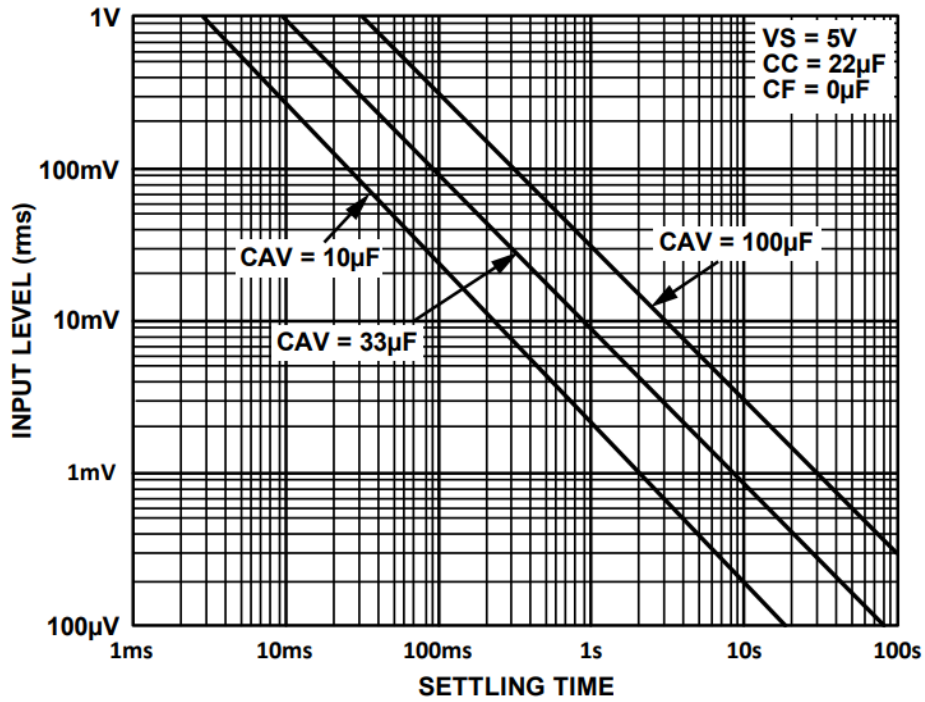**Figure 2.11** AD736 error reading for increasing input levels [49].

Figure 2.12 Settling time vs input level curve for common C_{av} values. For this design, C_{av} is 33 µF

to balance settling time with accuracy [49]

The averaging capacitor of the system was specifically chosen to balance settling time and a low frequency cutoff. According to Table 6 in the AD736 datasheet, for a low frequency cutoff of 20 Hz, the settling time will be 360ms for an input range of 0 mV to 200 mV with an averaging capacitor, C_{av}, of 33 µF. From Figure 2.12 from the datasheet, we see that the settling time decreases as input levels increase, indicating that 360ms will be the highest settling time that will limit the frame acquisition rate of the TEER system. From the datasheet, the coupling capacitor, C_C, is determined from the equation

$$F_L = \frac{1}{2\pi \cdot (8000)(C_C)}$$

and the datasheet advises using a value F_L equal to one tenth the lowest measured frequency, 100 Hz in the TEER system's case, to reduce amplitude error to 0.5% of the reading. This equates C_C to 1.989 µF which is implemented on the board as a 2.2 µF capacitor.

The four multiplexers feature break-before-make contacts that prevent connections between the old and new signal paths. This introduces possible errors in the measurement circuit and the need for the RMS-to-DC converter to resettle on the new signal before being read. This is handled dynamically in the firmware. At the end of each frame, the minimum voltage measured by the previous RMS-to-DC conversion is stored, and using Figure 2.12 of the AD736 datasheet, the new settling time is obtained from a Lookup Table (LUT) storing the intersection points given C_{av}=33 µF.

Operation of the AD736 were validated using a Digilent Analog Discovery waveform generator to output AC voltages of magnitude: 20 mV, 100 mV, 200 mV, 1 V, and 2V for frequencies of 100 Hz, 1 kHz, 10 kHz, and 100 kHz. The results of measured voltage and percent error are plotted in Figure 2.13. Errors are below 5% up to 10 kHz, but the error becomes dramatic at high frequency and lower input voltages. Lower input voltages are compensated for through amplification via the non-inverting op amp gain stage of Figure 2.10.

Future designs should employ higher quality RMS-to-DC converters to further minimize
measurement error across the entire frequency range.
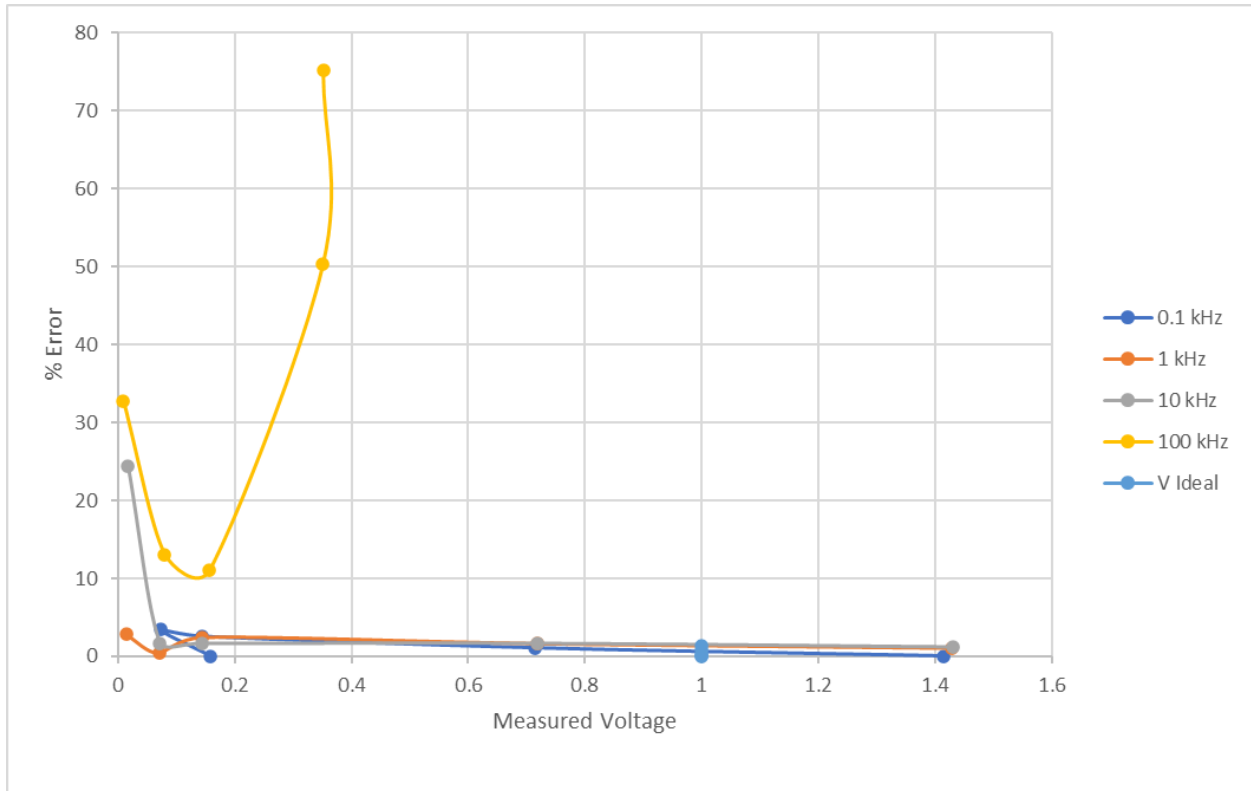
Figure 2.13 Measured error based on input level to RMS-to-DC converter.

Disconnections among electrodes lead to measurement errors from incorrect signal
output of the voltage buffers. With a disconnection of all the voltage measurement electrodes on
the multiplexer associated with the current injection plane, the output voltage waveform is
clipped and excludes important information of the negative half of the AC sine wave seen in
Figure 2.14. Errors are largely reduced by even a single proper connection, Figure 2.14, but this
demonstrates the importance of proper connection throughout the system. The degradation of a
single electrode has the potential to introduce significant measurement errors propagated
through the RMS-to-DC converter circuit.
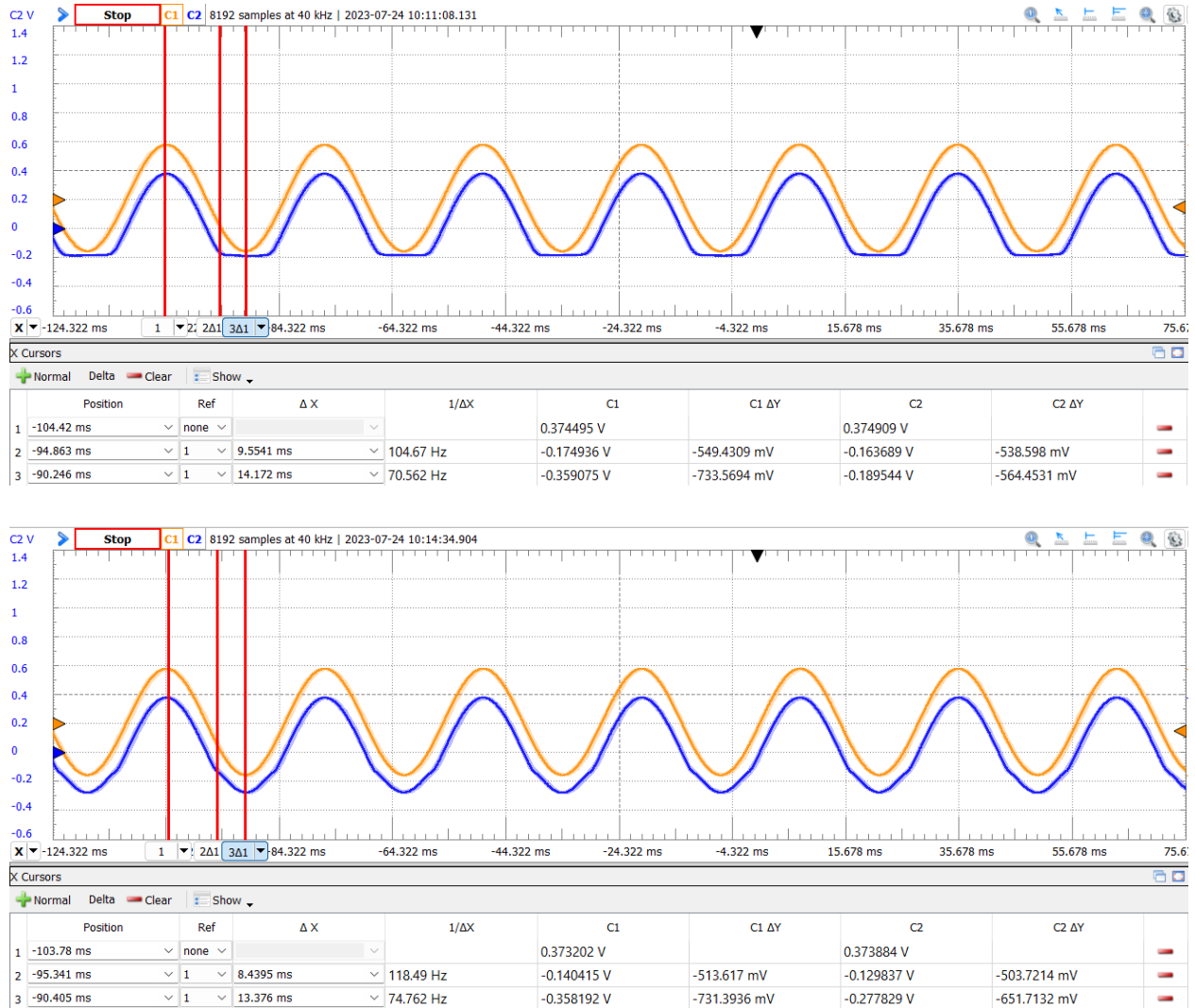
Figure 2.14 Output signal from electrode malfunction. Multiplexer signal clipping due to voltage buffer disconnections (top). A single measurement electrode is reconnected to the multiplexer (bottom).Orange traces represent the input signal to the multiplexer, and blue traces are the output signals from a voltage multiplexer.

Analog to Digital Converter

For this application, 2 ADS1115 ADCs are used [51]. These components have a programmable data rate of 8 samples per second (SPS) up to 860 SPS. The maximum sampling rate is lower than the minimum settling time of the RMS-to-DC converters, ensuring that the ADCs will capture the sampled data before channels are switched. Samples show variance within a few bits, which can indicate differences of hundreds of μV. To compensate for

this, the firmware computes an average of 100 samples. Unlike the data acquisition algorithm of

Zamora-Arellano et al., no samples are ignored in the measurement firmware, as the settling

time delay ensures that the transitory state of the floating voltage is compensated for.

Transimpedance Amplifier

An LM741 op amp-based TIA was used in this design to act as a virtual ground for the

reference current multiplexer and for phase difference calculations, Figure 2.8 [44]. With the

removal of the AD8302 phase detector in the current design, the TIA has no functional use

besides the virtual ground connection.

Temperature and Humidity Sensor

A DHT11 temperature and humidity sensor was integrated into the design to provide live

health updates of the system [45]. Future iterations of the design are intended for use within an

incubator in a sealed chamber to limit the circuit's exposure to the humid environment.

Monitoring of the chamber's humidity will allow the user to add desiccant or ensure other means

of humidity compensation are maintained for the longevity of the hardware.

Phase Detector

Among the measurement instruments employed, a phase detector was initially used in

tandem with the differential amplifier. It has been shown that relative permittivity reconstructions

are just as insightful as electrical conductivity images [47]. This system uses an AC waveform,

so phase detection is a useful metric when considering the capacitance of the tissue layer. An

AD8302 breakout board was ideal for this application as it is capable of outputting the phase

difference between two signals, one from the output of a voltage sensing multiplexer and the

other from the TIA. The maximum output voltage is 1.8 V, which is another reason why the

maximum gain of the ADCs is set to GAIN_TWO.

In the final iteration of the TEER platform, the AD8302 was removed. The AD8302

proved to be a recurring issue on the PCB as disconnections to the inputs would lead to major

increases in the voltage of the +2.5 V LDO, up to 3.6 V which is outside the +10% deviation of

the rail. In addition, direct comparison of the two waveforms was no longer needed once the differential amplifier was removed. Upon further review of phase sensitive systems, it was discovered that phase is more useful in systems that analyze materials of different permittivities within the same target body. As this system is targeted at applications with tissue monocultures, a phase-sensitive system was deemed to be out of the scope of this design [50]. Boone *et al*. also report that measurements of resistance reduce measurement error and at lower frequencies, the complex impedance is mostly resistive. The system was simplified to only measure the magnitude of the real parts of the signals.

Validation Testing

This design was first validated with multiple breadboards acting as submodules, Figure A.1. For schematic details, see the GitHub repository [37]. Validation of each submodule worked without failure as described, but noticeable power issues were encountered upon assembly of the PCB device. For exact details on debugging power issues, please refer to the Appendix section "Power Issues."

Chapter 3 - Software Design

Image Reconstruction

Thus far, a platform has been created to inject currents through an analog multiplexer and measure boundary voltages through a demultiplexer. The signal is then fed through an RMS-to-DC converter stage to the ADCs. What must happen next is image reconstruction. To find out what each measurement means in the scope of the entire measurement frame, we must solve the EIT *forward problem*. The forward problem describes the relationship between design parameters and measurements. These parameters include electrode shape, orientation, size, quantity, depth of penetration, body irregularities, etc. [52]. Oftentimes, solving the forward problem is used to model the target body geometry and optimize measurements through simulation. In this work, tests are conducted on the electrode and body parameters to determine the ideal testing environment that yields the highest spatial resolution of inclusions.

During image reconstruction, solutions to the forward model are used to predict the voltage measurements of a homogenous body. The second EIT problem, the *inverse problem*, compares the measured data to the predicted data and computes the perturbation that is associated with the inclusion. The inverse problem begins with measurements and maps the relationship to parameters, hence it is the inverse of the forward problem. Through this mapping, the inverse problem recovers a unique solution for σ, discussed in depth later, an internal conductivity distribution that is different from the homogenous background conductivity σ_0 of the forward model. The resulting internal conductivity distribution of the inverse problem is plotted within the body defined by the forward problem, completing the image reconstruction process. When systems become complex, computer simulation with finite element methods (FEM) solve these two problems well [52].

In the world of EIT, a widely used open-source package is Electrical Impedance Tomography and Diffuse Optical Tomography Reconstruction Software (EIDORS). Thanks to the work of Vauhkonen *et al*. and Polydorides and Lionheart, there are MATLAB packages available

for researchers to solve forward and inverse problems within 2D and 3D systems [53][54]. EIDORS is used extensively for its effective computation of the Jacobian using MATLAB and its inherent intuitive design for novel applications and flexible code base. There is commercial software like COMSOL Multiphysics and open-source software that perform the same function as that reported by Jehl *et al*., a C++ based numerical solver based on DUNE [55]. Their results show a 2x computational improvement over EIDORS, but lack intuitive code that can be broken down and reconfigured to suit new applications. More complicated EIT systems would benefit from this package as the computation time becomes noticeably higher with each addition of complexity in an EIDORS model.

Forward Problem

Two common methods are used to solve the forward model, that is, analytically and numerically via FEM. In the case of simple, 2D shapes like a resistive mesh, analytical methods work well and aid in understanding the underlying principles of current density, surface voltages, and application-specific limits. When shapes become irregular, an FEM is a more common method for understanding EIT systems. These models can be useful for understanding the optimal shape and placement of surface electrodes, the limits of detection, and can even incorporate noise into the models to determine the sensitivity of the system given different SNRs [52].

For the implementation of a forward model, research into planar electrode EIT systems for applications in mammography were utilized [11][12][56]. The platform structure is displayed in Figure 3.1. Here, the tissue of interest is pressed between the electrode planes and currents are injected from the top electrodes and voltage measurements are recorded at non-current carrying electrodes. These systems are analogous to that proposed in this TEER system. Their efforts into systems that resolve the spatial location of a cancerous inclusion show high sensitivity and depth detection.
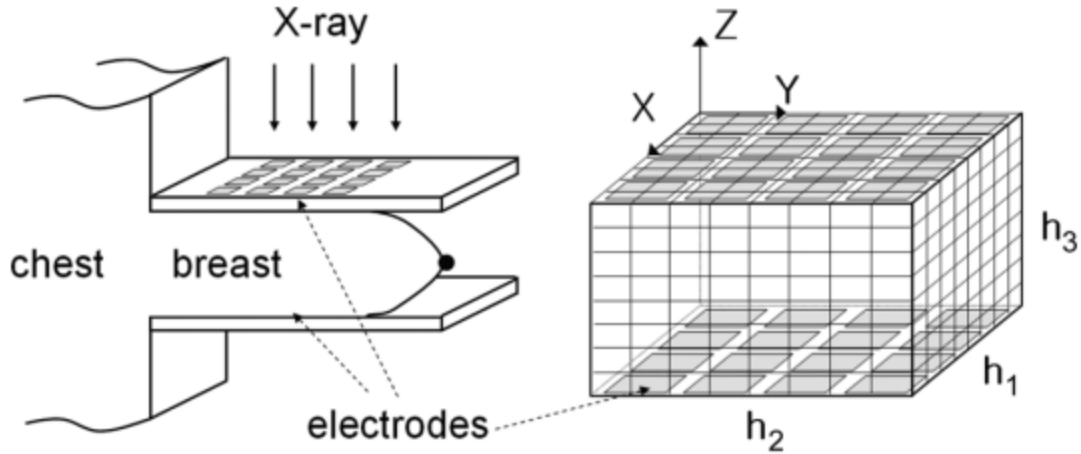
Figure 3.1 Mammography application of planar EIT system [11].

In solving the forward problem, boundary conditions are necessary to simplify the CUT or body. These simplifications reflect ideal conditions that can be assumed for the system to significantly reduce computational time while marginally degrading the image reconstruction. To predict the surface voltages, the forward problem solves for the current density distribution after a current is applied to the surface electrodes. Given boundary conditions that the voltage $u \to 0$ as $\sqrt{x^2 + y^2 + z^2} \to \infty$, the forward problem is well-posed [56]. This condition stipulates that the voltage decreases as the radius from the surface increases and that the current is conserved in the body.

Another set of boundary conditions can be applied to the electrodes to reduce the complexity of the calculation. For simple models, a continuum model can be used that assumes there are no electrodes and the current is uniformly applied at the surface. Another condition, used in the Python reconstruction script, is the gap model that assumes a uniform current applied at the surface under each electrode. The shunt model and complete electrode model come the closest to modeling real-world electrodes with capacitive effects at the electrode surface and impedance formed between the electrode-tissue gap [2]. For this work, the gap model was used to best balance simplicity of computation and real-world representation of the planar electrode arrays. The gap method approximates the current density $j(x, y)$ by

$$j(x,y) = \begin{cases} \frac{I_l}{A_l} & : \quad \text{for (x,y) on } e_l \\ 0 & : \quad otherwise \end{cases}$$

$$V_l = \frac{1}{A_l} \int_{el} U(s)ds,$$

where I_l is the current on the lth electrode, A_l is the surface area of e_l, V_l is the voltage of the

lth electrode, and $U(s)$ is the surface voltage [11].

The forward model relies on solving for the surface voltages given a current density

distribution on the surface of the body. Four equations solve for the current densities on the top

and bottom planes for each applied current vector.

$$j_{n,m}^* = \frac{4}{h_1 h_2} \sum_{l=\alpha*}^{\beta*} \frac{I_l}{A_l} \iint_{el} \cos\frac{nx\pi}{h_1} \cos\frac{my\pi}{h_2} dxdy$$

$$j_{0,0}^* = \frac{1}{h_1 h_2} \sum_{l=\alpha*}^{\beta*} I_l$$

$$j_{0,m}^* = \frac{2}{h_1 h_2} \sum_{l=\alpha*}^{\beta*} \frac{I_l}{A_l} \iint_{el} \cos\frac{my\pi}{h_2} dxdy$$

$$j_{n,0}^* = \frac{2}{h_1 h_2} \sum_{l=\alpha*}^{\beta*} \frac{I_l}{A_l} \iint_{el} \cos\frac{nx\pi}{h_1} dxdy$$

These equations are computed for each voxel, Vox$_{n,m}$, for each set of current vectors. It

is clear that these equations can be quickly optimized in software since one electrode per plane

is used as a current carrying electrode. Every other electrode on the top and bottom plane has a

current of 0. In the Python script, these vectors are precomputed for each current vector and are

used to solve for the homogeneous body voltage, $V_{l,0}^k$ in [11].

Inverse Problem

The inverse problem is nonlinear or ill-posed. There are many ways to solve the inverse

problem, such as linear back projection or iterative algorithms, but regardless of the technique,

an FEM is used with the aim to find the perturbation at each point of the mesh [57][58][59]. Early EIT systems used 2D FEM models for their reconstruction, but thanks to the work of groups like Polydorides *et al.*, 3D FEM models are available to quickly solve complicated simulations that are representative of their real-world counterparts. For the Python script application, the algorithm proposed in [11] was implemented.

At a high level, the desired output is a conductivity matrix $\sigma(p)$ given the assumption that a spatially varying conductivity σ differs slightly from a homogenous conductivity, σ_0, by a small perturbation, η. This is where the ill-posed nature of the problem is best understood. An inclusion within the body may have large spatial conductivity changes in its immediate vicinity, but this change is seen as a very small change in conductivity at the surface during voltage measurements. For this, we must remember that the body is governed by Maxwell's equations and $\nabla \cdot (\sigma(p)\nabla \mathrm{U}(\mathrm{p})) = 0$ inside the body B, or that the divergence of the magnetic field from an applied current inside the body is 0. This means that the current density is contained entirely within the body B. From this, we can understand the concept of perturbation $\eta(p)$ from the lens of Kirchoff's Laws. The current density must be conserved within the body, so the goal of the inverse problem is to identify the voxels within the body where more or less current passes. To solve for the perturbation matrix η we must solve matrix $A_{x,k,r}$ and the vector $D_{x,k}$,

$$A_{x,k,r} = \int_B \Phi_r(p)\nabla \mathrm{U}_0^{\mathrm{x}} \cdot \nabla \mathrm{U}_0^{\mathrm{k}} dp$$

$$D_{x,k} = \sum_{l=1}^{L} I_l^k V_{l,0}^x - I_l^x V_l^k$$

where x and k are current vectors applied to the electrodes, $V_{l,0}^x$ is the homogenous body voltage calculated in the forward problem, and V_l^k is the voltage measurement for the unknown conductivity distribution. Afterwards, the conductivity distribution is calculated as $\sigma(p) = \sigma_0 + \eta(p)$. Detailed steps can be found in [11][12][56].

Regularization is typically used in an inverse model. Regularization techniques act as a filter of the inverse model matrix and smooth the weighting of prior information. Common regularization methods include Bayesian techniques, least-squares minimization of the NOSER algorithm, or Tikhonov regularization, but what is common among all is the importance of tuning a smoothing parameter [12][58][60]. In this work, the regularization methodology described in [11] was used. This regularization method involves solving the linear system

$$[A^T A + \epsilon \mathrm{Diag}(A^T A)]\eta \ = A^T D$$

With a regularization parameter $\epsilon = 0.01$

Implementation

The implementation of a reconstruction algorithm was done in two ways: through a Python script implementing the algorithms described in [11] and through the EIDORS package. The Python script was developed to take advantage of the specificity of a reconstruction algorithm designed for planar systems. EIDORS is a much more generalized reconstruction package, which has the potential to do reconstruction well for common EIT systems, like cylinders, but is less documented for planar systems. Despite initial success with the Python script, the decision to use EIDORS was made after simulations on representative test bodies showed reasonable spatial reconstruction, see Figure 3.2. For a detailed description of the Python script, see "Python Image Reconstruction Script" in the Appendix.
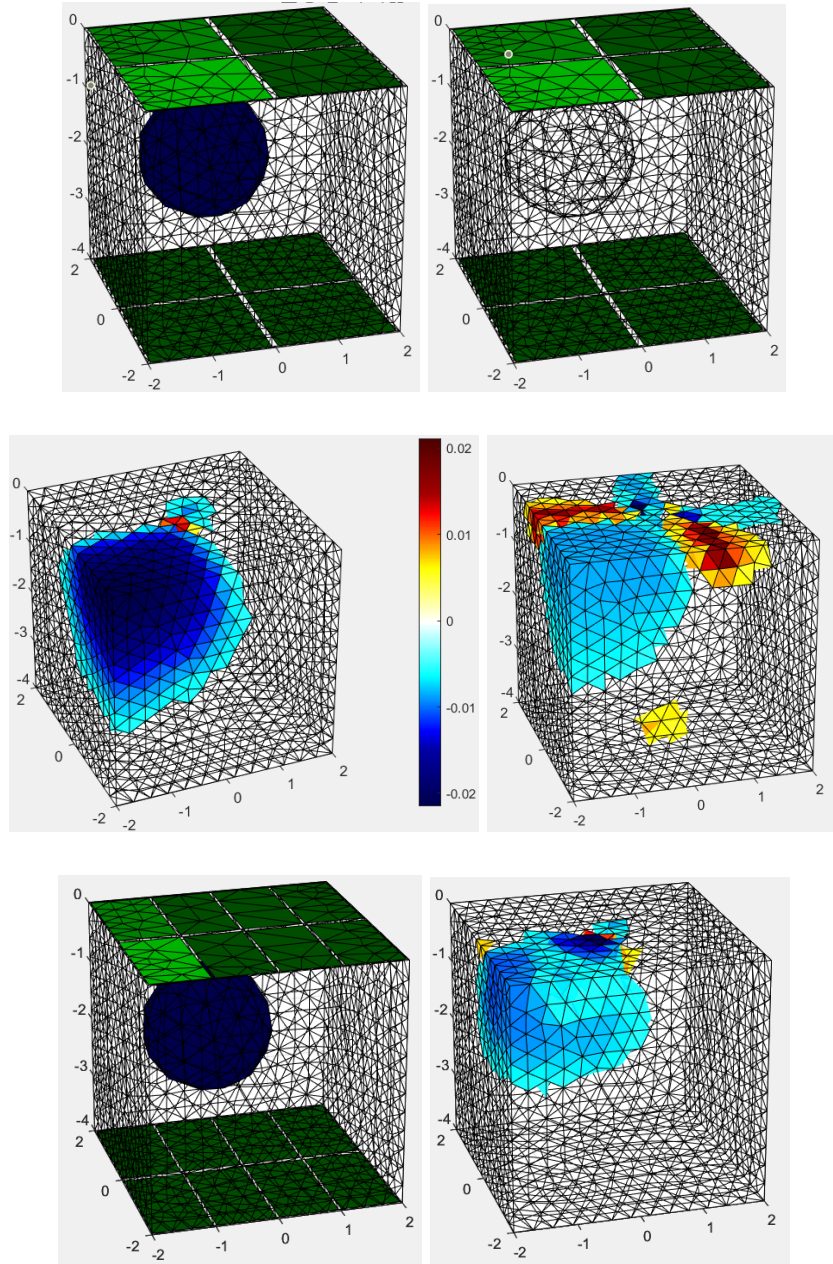
Figure 3.2 Verification of EIDORS efficacy for planar electrode arrays. Top left, FEM model with non-homogenous inclusion under the first electrode on the top plane. Top right, homogenous body with FEM nodes set to background conductivity for reconstruction. Middle left, Laplace regularization used in reconstruction. Middle right, NOSER regularization. Bottom left, electrode count is doubled to test the image enhancement from higher electrode counts. Bottom right, correct orientation of spherical inclusion, with fewer artifacts.

Modeling of the OoC system geometry is a prerequisite to image reconstruction. Without a known geometry, data will not relate to an appropriate model, which will affect the calibration of the image reconstruction algorithm [46]. EIDORS simulation of each system parameter is required to determine the optimal geometry for this application, such as electrode count, size, and distance between plates. Simulations to detect the spatial location of planar bodies were successful. In the following simulation figures, cool areas indicate an area with lower conductivity compared to the background which is clear. Hot colors indicate areas with higher conductivity. As a low conductivity inclusion is tested, all hotter colored areas are known to be image artifacts, as there are no high conductivity objects to reflect these reconstructions.

A range of electrodes and geometries were tested. For a planar inclusion, electrode configurations of 4x4, 8x8, 16x16, and 32x32 were successfully created, showing the spatial improvement that each increase in design complexity can impart on the final reconstructed image. These figures show a clear tradeoff between electrode count and the resulting reconstruction, similar to the findings of [61]. The best reconstruction, when considering computational overhead versus the final image, is a 16x16 electrode system like that in Figure 3.5 and Figure 3.8, able to correctly identify the spatial depth and orientation of a conductive inclusion. Each system had a high level of detection for inclusions near the electrode plane when comparing Figures 3.4, 3.5, 3.6 with Figures 3.7, 3.8, and 3.9, suggesting higher efficacy in TEER systems closer to one plane rather than evenly distributed nearer the midpoint between planes.

Another important factor in the reconstruction process is the regularization algorithm used. Each figure shows two reconstructions, one corresponding to a Laplacian regularization and the second to a NOSER regularization. Even in this case, it is not definitive as to which reconstruction is best suited for a set of measurements. In a 16x16 electrode configuration, a Laplacian regularization shows a more distributed reconstruction for a deeper inclusion compared to an inclusion closer to the planar surface, Figure 3.8 and Figure 3.5 respectively.

The opposite is true for a 32x32 electrode system, Figures 3.9 and 3.6, implying that each reconfiguration of the design requires systematic testing to define the best reconstruction procedure.
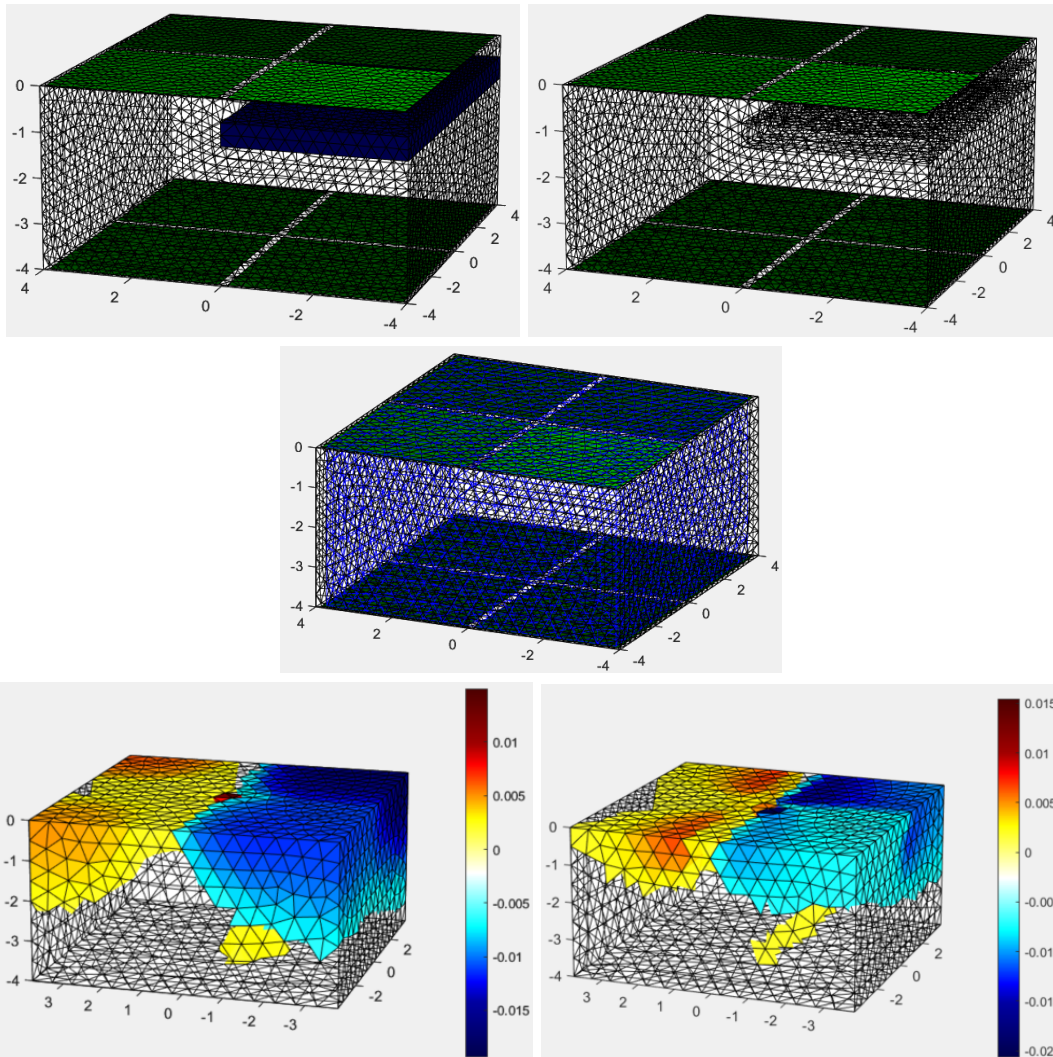
Figure 3.3 Planar inclusion detection in 4x4 electrode configuration. Top left: 4x4 electrode system with planar insulating inclusion. Top right: inclusion set to background conductivity for forward solver. Middle: coarse mesh used for mapping inverse solution to forward model. Bottom: System correctly predicts the inclusion depth and orientation, but the reconstruction accuracy is diminished by presence of artifacts. In the figures, cool areas indicate an area with lower conductivity, measured in $S \cdot m^{-1}$, compared to the background which is clear. Hot colors indicate areas with higher conductivity. There is a small difference in reconstruction from different regularization techniques: Laplace (bottom left), NOSER (bottom right).
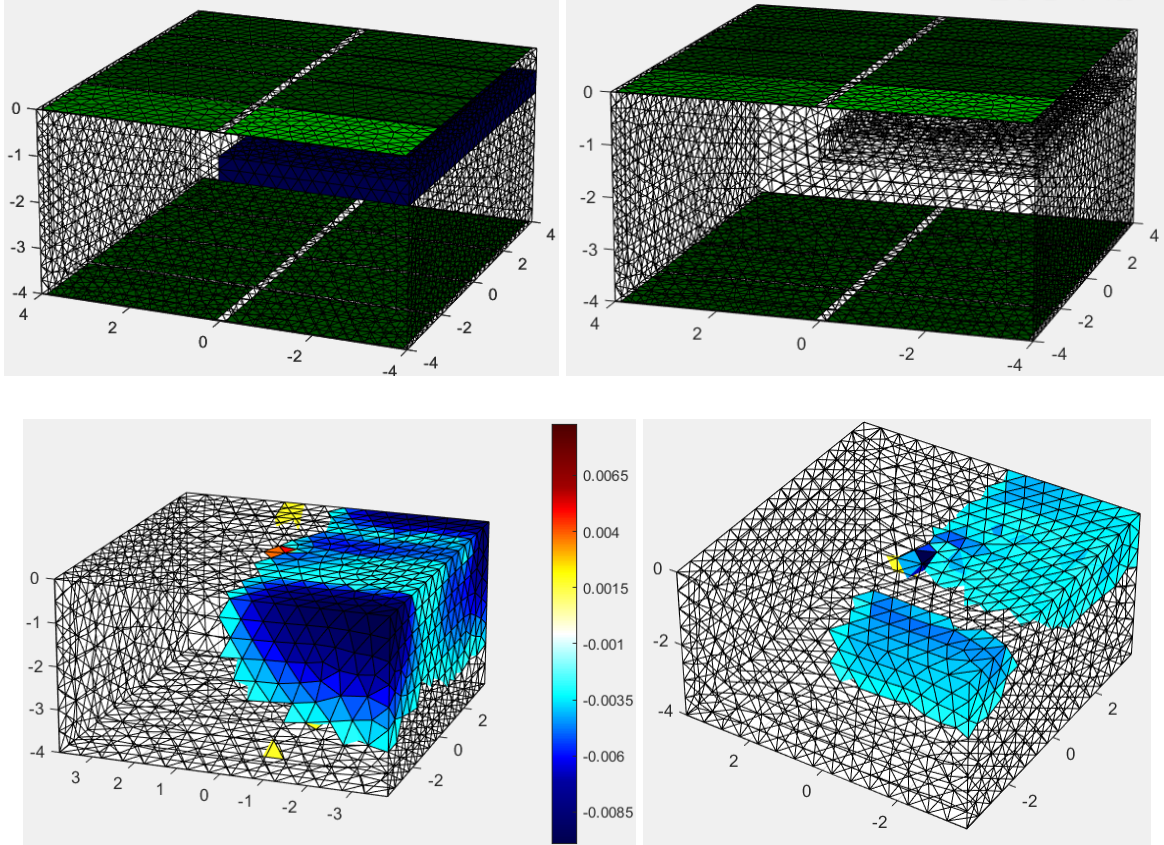
Figure 3.4 Enhanced detection in an 8x8 electrode chamber. Compared to a 4x4 electrode system, there is a significant decrease in artifacts.
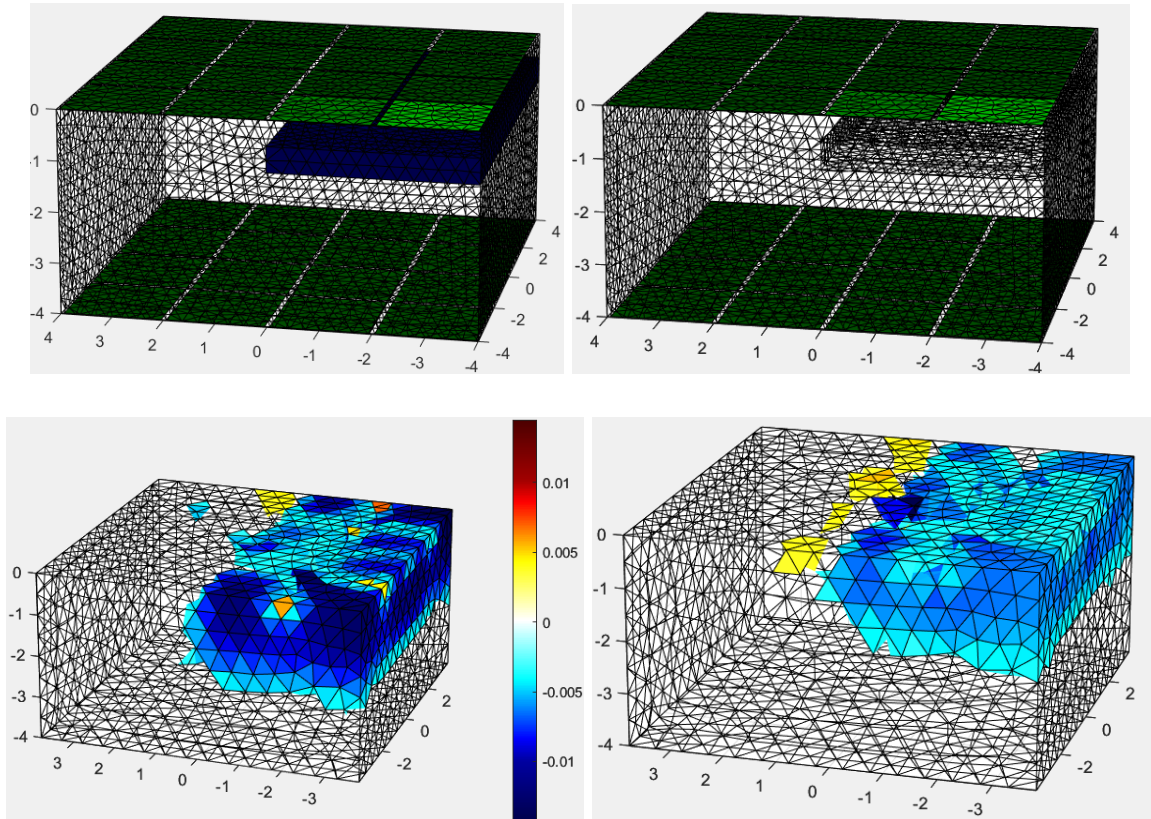
Figure 3.5 Increased detection in 16x16 electrode chamber. Fewer artifacts are seen in the reconstruction and the shape of the inclusion is better resolved.
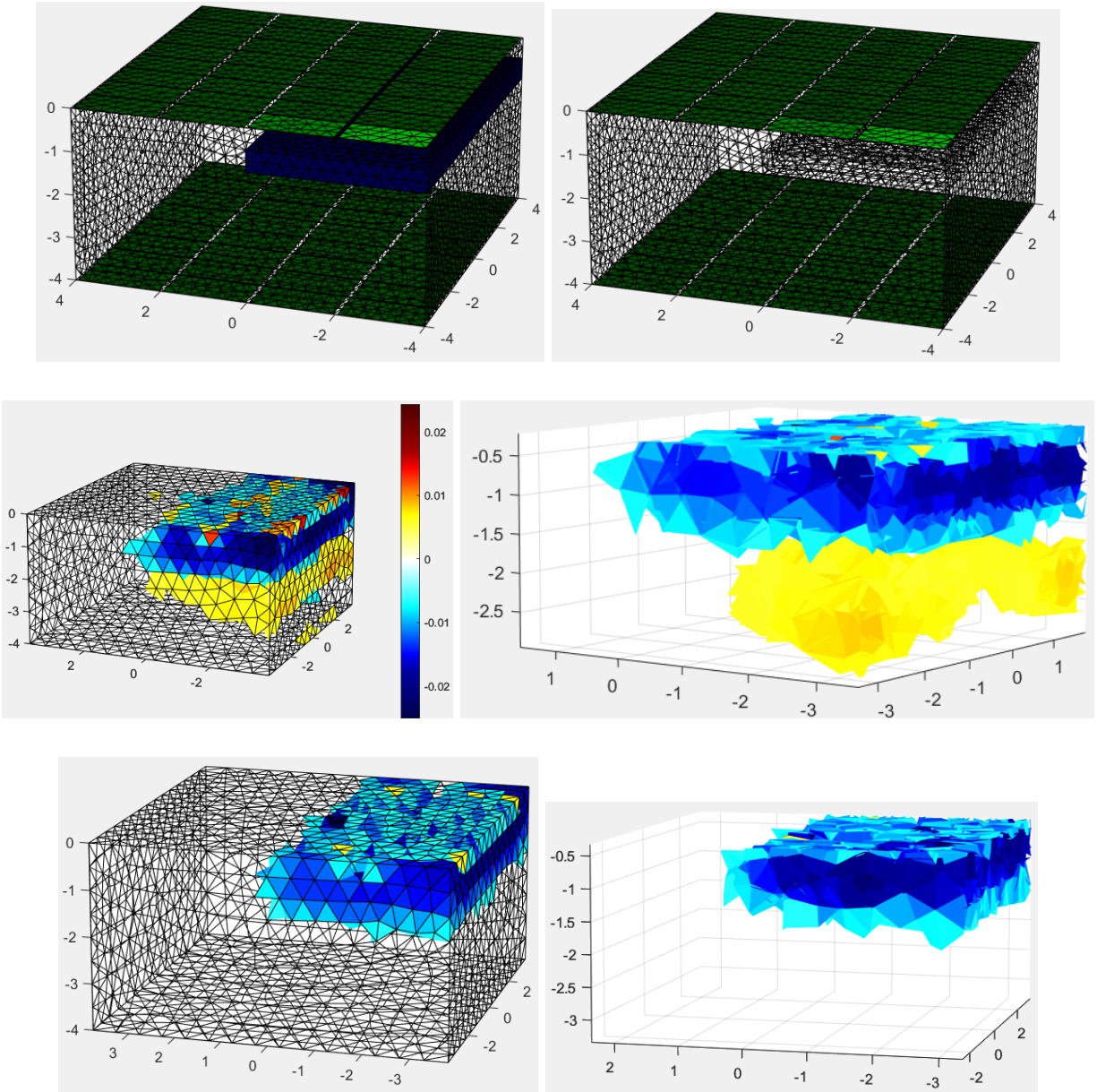
Figure 3.6 32x32 electrode arrays spatial detection. The reconstruction has the highest spatial detection of the chamber models using a NOSER regularization technique (bottom). More artifacts are depicted than a 16x16 electrode chamber with a Laplace regularization (middle). This reconstruction is the most accurate, but demonstrates a small increase in overall detection at the cost of significant computational complexity. Higher electrode systems inhibit quick image reconstruction.
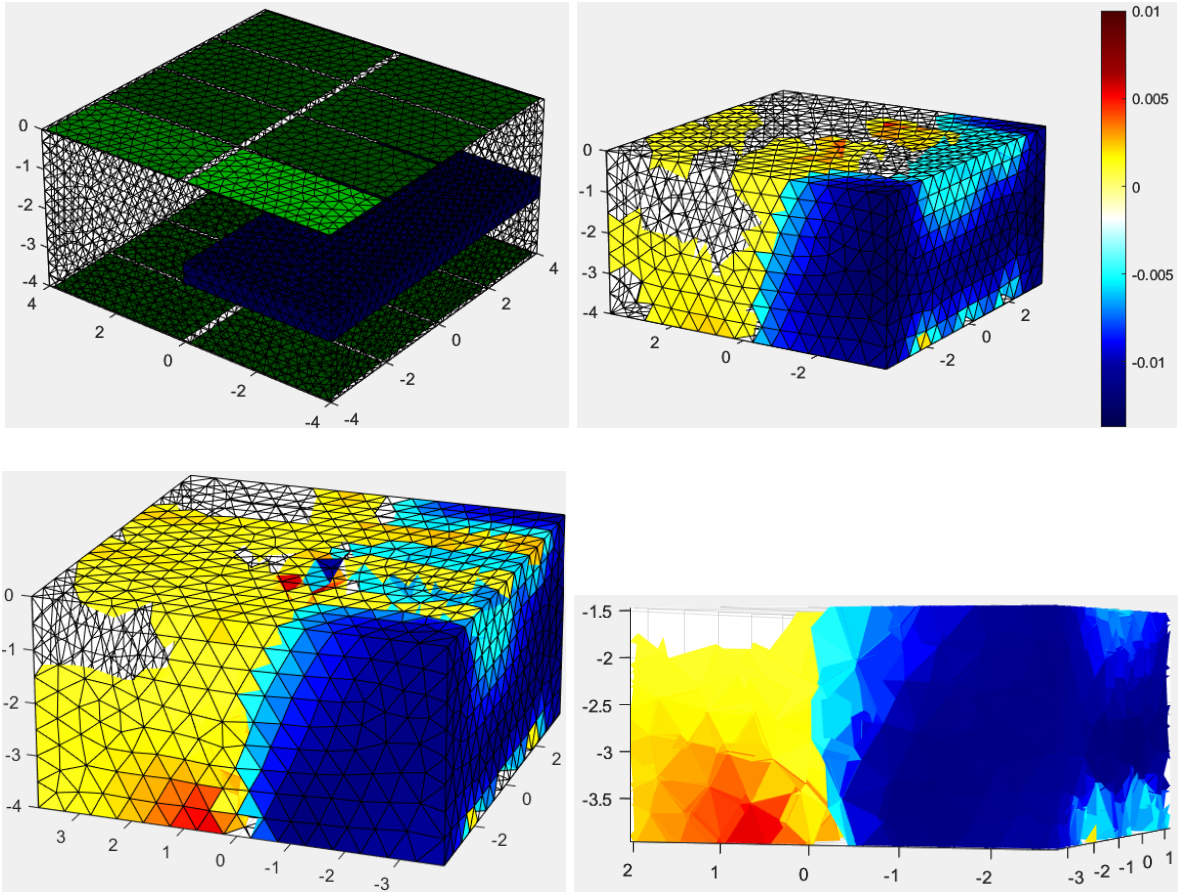
Figure 3.7 Depth detection of 8x8 electrode system. Inclusion is centered in the middle of the chamber to test depth detection of 8x8 electrode setup. More artifacts are present in the reconstruction and the clarity of the image has significantly decreased.
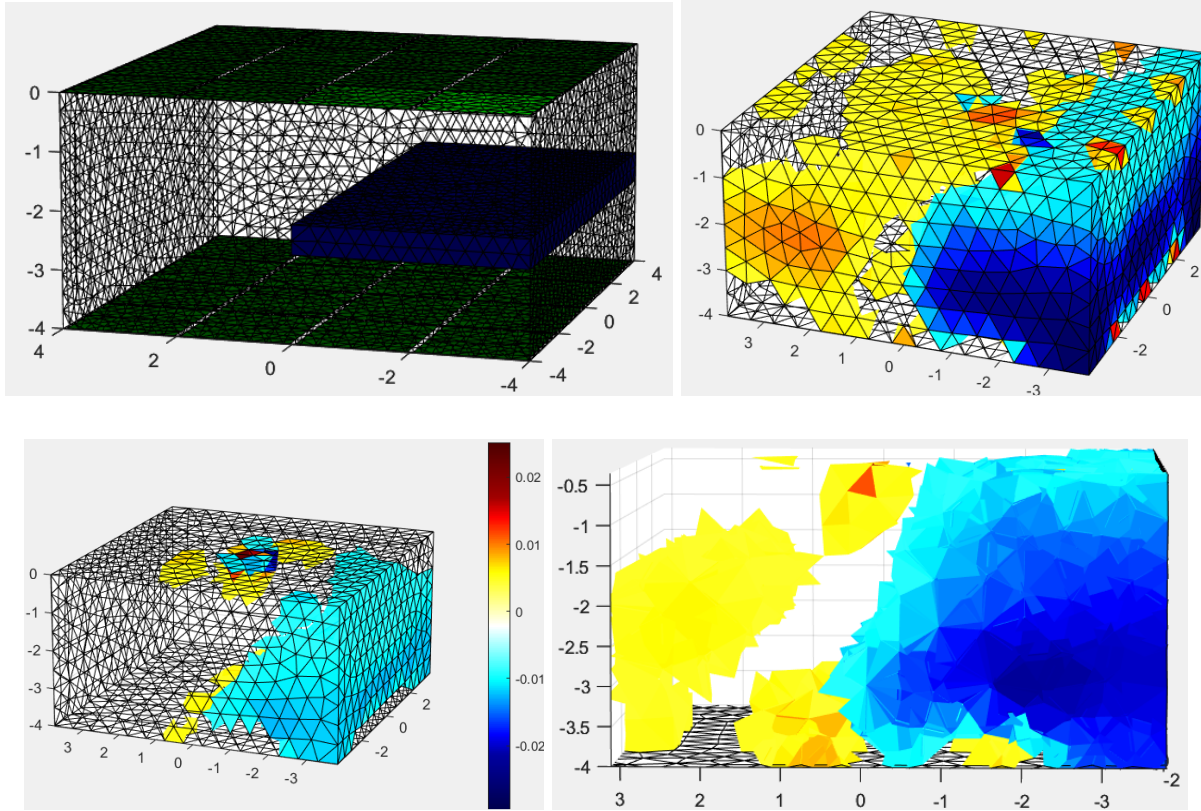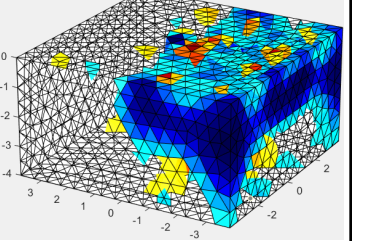
Figure 3.8 16x16 electrode chamber depth detection simulation. Smoother inclusion reconstruction than an 8x8 system, but still suffers from a high amount of image artifacts.
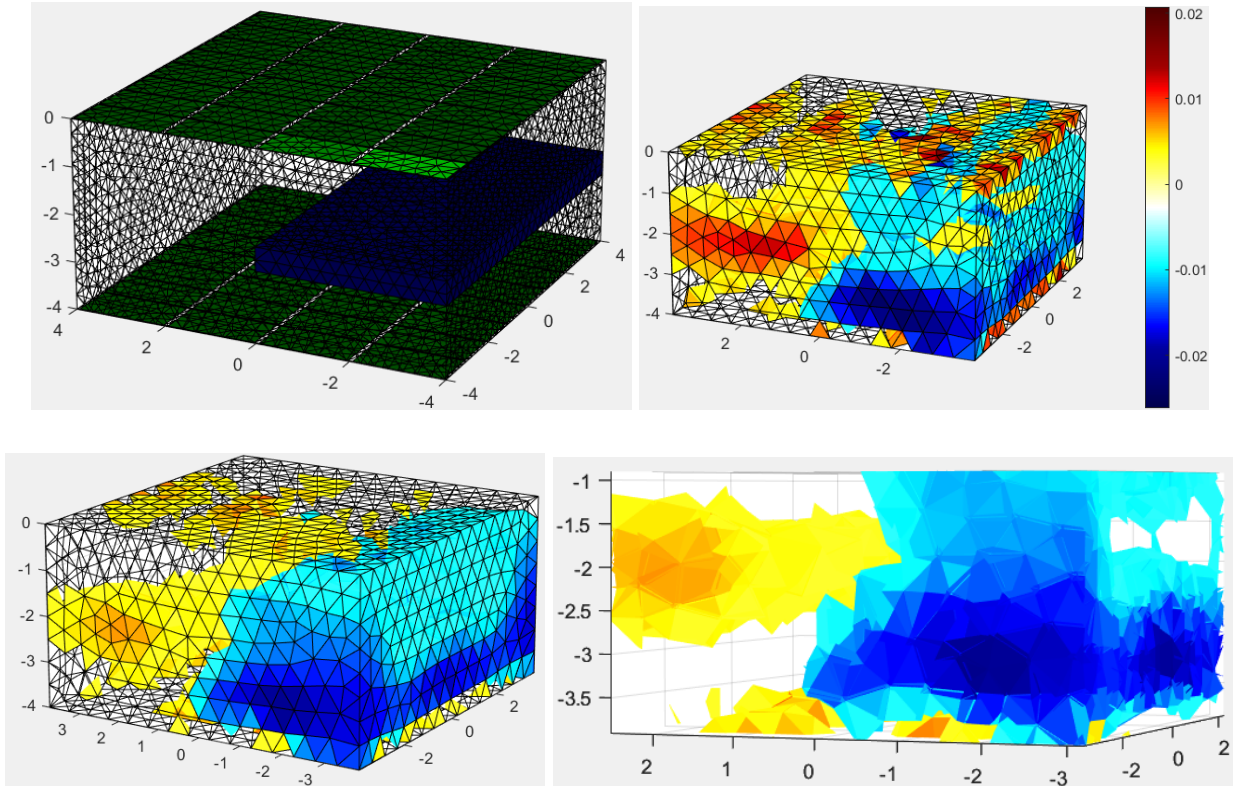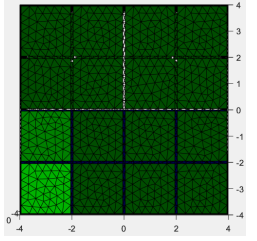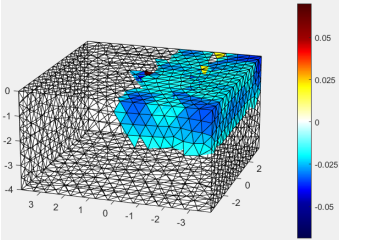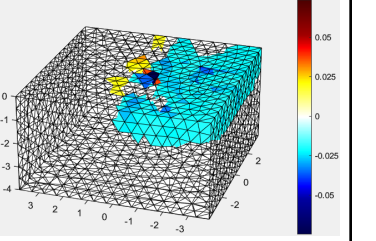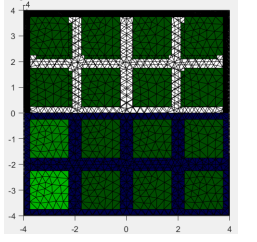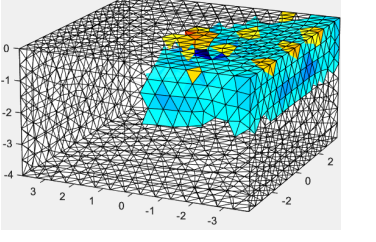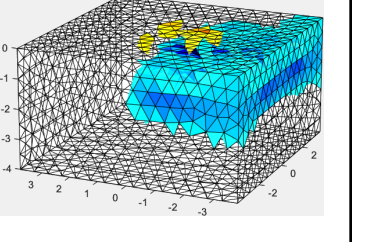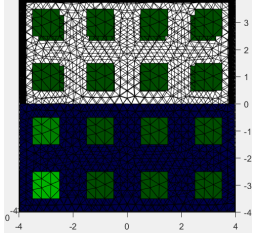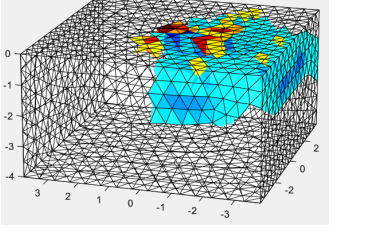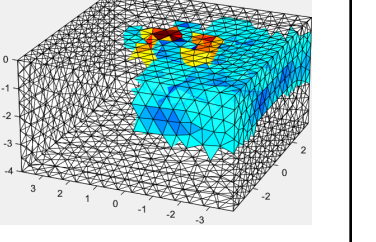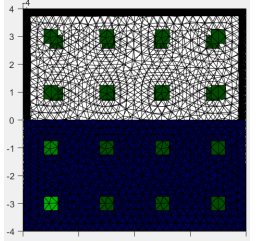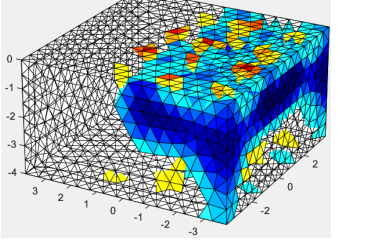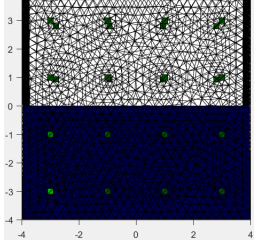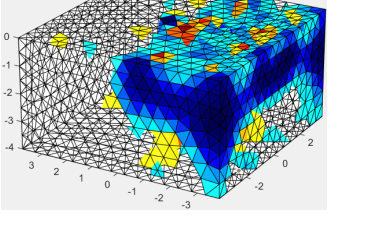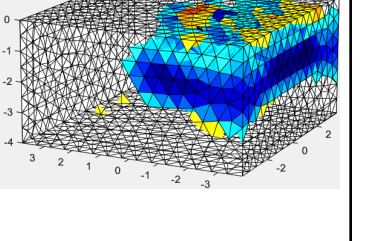
Figure 3.9 32x32 electrode chamber depth detection simulation. 32x32 electrode chamber exhibits diminishing detection versus a 16x16 electrode system. Depth detection shows a high resolution for the location of the inclusion but the reconstructed image suffers from an abundance of unwanted artifacts.

In designing the test platform, it was important to consider the number of electrodes and the distance between plates. The simulations in Figures 3.3-3.9 demonstrate these effects, but more stringent testing is required to determine the optimal electrode-tank setup. Taylor *et al*. report that maximizing the number of electrodes to capture more information of the permittivity distribution comes at the cost of smaller electrodes which have worse signal-to-noise ratios [57]. The tradeoff between the number of electrodes and the reconstructed image quality has been simulated, but the ideal electrode size also requires simulation. Ren *et al*. [61] document the significance of distance between the plates. Electrodes are most sensitive to the area perpendicular to their face and closest to the center, and less sensitive around the electrode and when the distance between plates increases. EIDORS simulations were used to optimize electrode size and depth of reconstruction for planar inclusions.

Simulations consisted of 16x16 electrode plates, with a top area of 64 units^2. For the electrode model, sizes were chosen with a varying length by width dimensions of 1.95 units x 1.95 units, 1.5 units x 1.5 units, 1.0 units x 1.0 units, 0.5 units x 0.5 units, and 0.2 units x 0.2 units. A planar inclusion that occupied half of the internal cross sectional area with a height of 0.5 units was placed 0.5 units from the surface to optimize the sensitivity of the top plane of electrodes for these tests. Two regularization algorithms were used, Laplacian and NOSER.
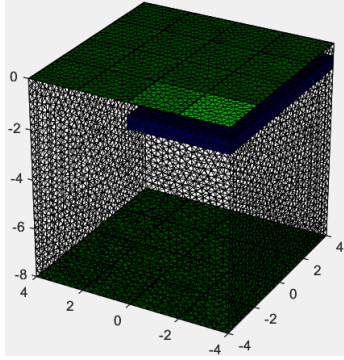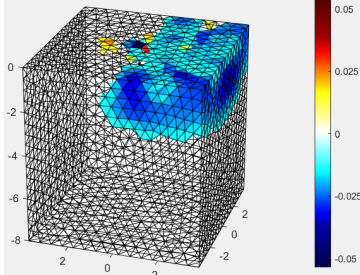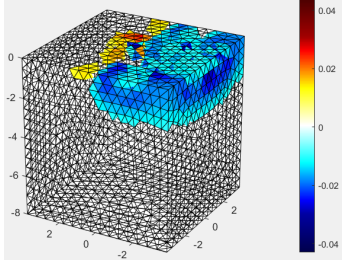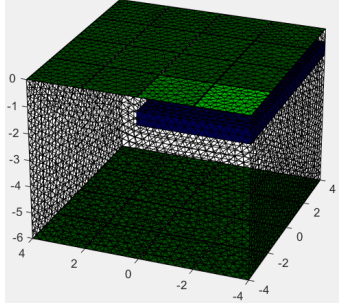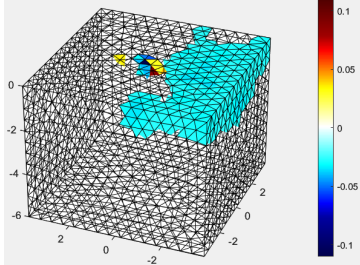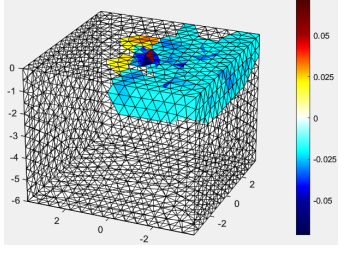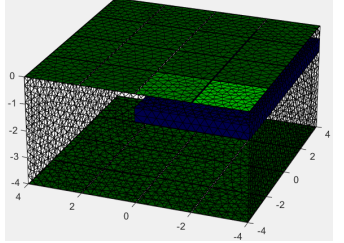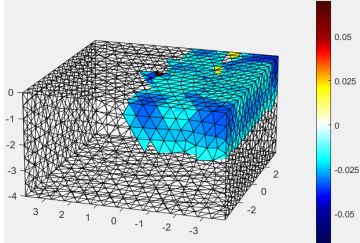
Table 3.1 Influence of decreasing electrode size on image reconstruction fidelity.

(Units x Units)	Electrode Configuration	Laplacian Reconstruction	NOSER Reconstruction
1.95x1.95			
1.5x1.5			
1.0x1.0			
0.5x0.5			
0.2x0.2			
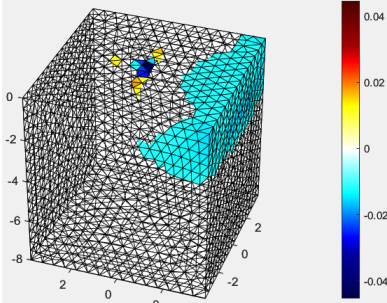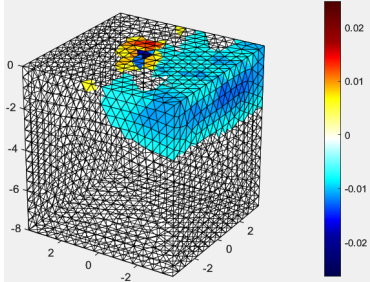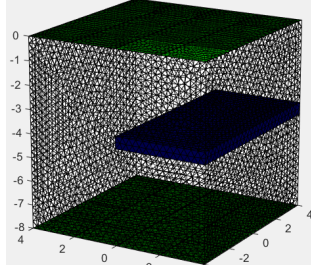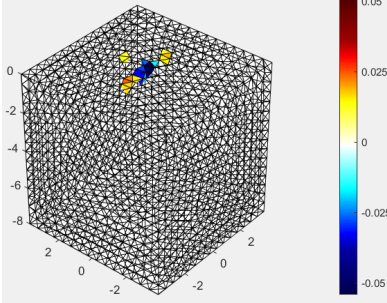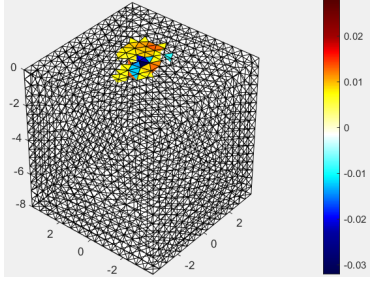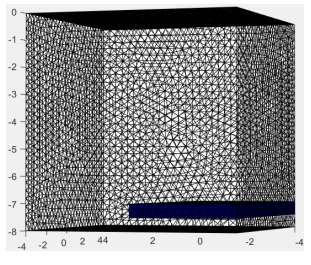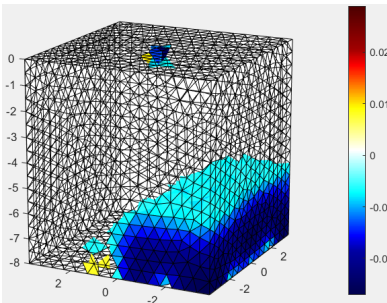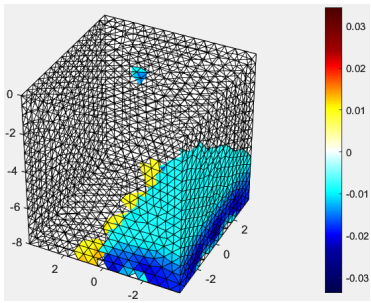
From Table 3.1, it is evident that larger electrodes detect the inclusion with the most spatial accuracy. Smaller electrod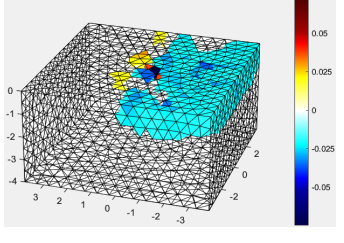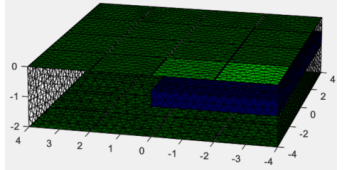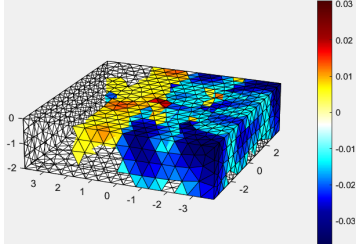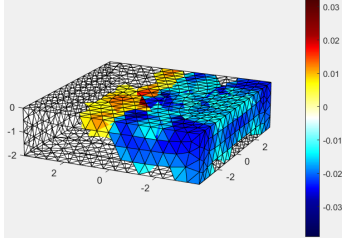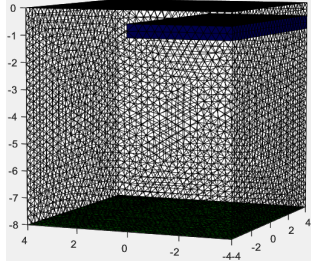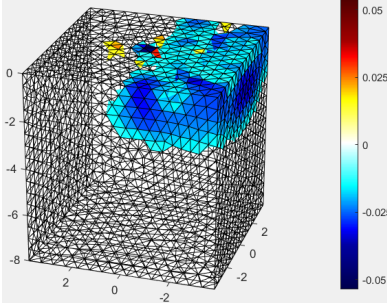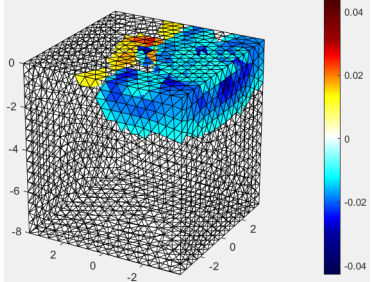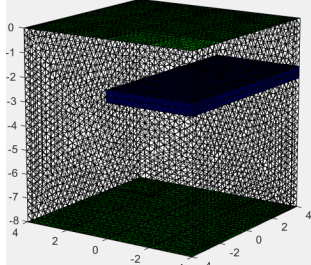es are able to reconstruct the inclusion with the correct conductivity, but the proportions of the inclusion are incorrect. Artifacts, seen in lighter colors, distort the reconstruction and the inclusion is reconstructed as a larger body. After several iterations with added noise, it was decided that 1.95 units x 1.95 units square electrodes had the most consistency in their reconstructed image.

The depth of the test chamber was also investigated. Using 1.95 units x 1.95 units electrodes, the square plates were placed at distance ratios (height:length) of 1:1, 0.75:1, 0.5:1, and 0.25:1 to determine the optimal distance between plates. From Table 3.2, the ratio of 1:1 has the best overall accuracy for resolving the inclusions shape, depth, and conductivity. Ratios of 0.75:1 and 0.5:1 have similar results but fail to reconstruct the exact shape and conductivity. It would appear that parallel plate electrode planes are more agnostic of depth considering the lack of artifacts in most of the simulations and the general shape of the reconstructed inclusion, which is consistent with findings from parallel plate EIT systems [62]. In a cylindrical setup in Figure 1.2, it is clear that the cross and opposite measurement patterns have the most in common with the proposed system. When looking at the areas of sensitivity in these two patterns, the most sensitive area is directly adjacent to the electrode, but nearly constant across the chamber. Table 3.3 clearly shows that the image reconstruction quality is best near an electrode plane. For these reasons, the test system was set at a depth-to-length ratio of 1:1 with inclusions near an electrode plane. A system with a ratio of 0.5:1 like that shown in Figure 3.8 does show better detection of objects nearer the middle of the chamber compared to the 1:1 simulation. For this application, the ratio was set at 1:1 because the test chambers are easiest to produce in that configuration and the detection at the electrode surface is consistent with the reconstruction accuracy of Figure 3.5 in a 0.5:1 system.

Table 3.2 Testing different chamber depths effect on image quality.

Height: length	Electrode configuration	Laplacian Reconstruction	NOSER Reconstruction
1:1			
0.75:1			
0.5:1			
0.25:1			

Table 3.3 Analysis of inclusion depth versus reconstruction clarity in 16x16 electrode chamber.

Depth	Electrode configuration	Laplacian Reconstruction	NOSER Reconstruction
1/8th			
1/4th			
1/2			
7/8th			

Simulations in EIDORS had limitations. Complex geometries and high electrode counts proved difficult for the mesh generation software to create. For example, Figure 3.10 shows the large amount of mesh points required to generate a simple permeable membrane of 4x4 pores.
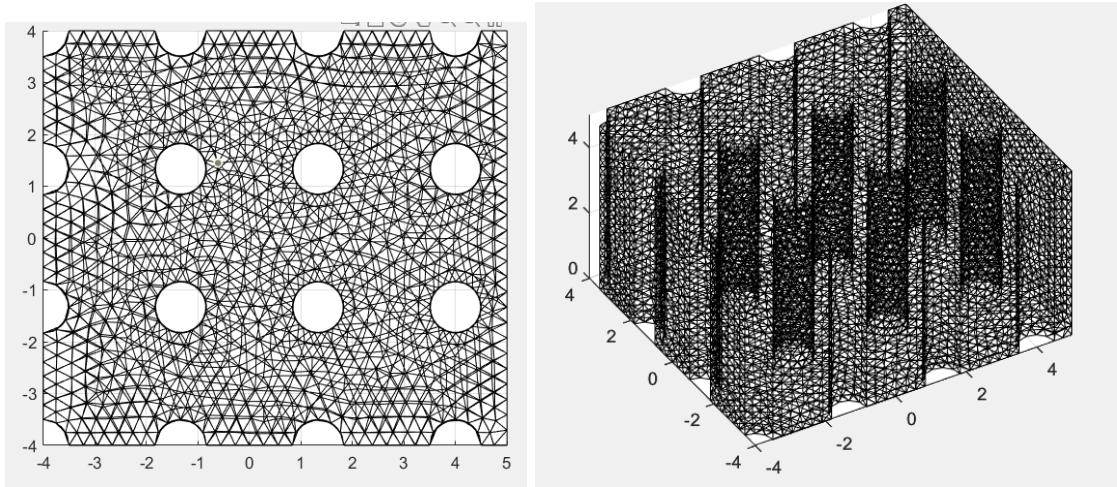
Figure 3.10 Netgen mesh of a thin porous membrane. Cylindrical shapes add significant complexity to MATLAB simulations.

The increased complexity of the mesh carried over significantly to the process of reconstruction. Consider the system in Figure 3.11 that recreates an 8x8 planar electrode array with a permeable membrane and a thin conductive plate representing a tissue monolayer. MATLAB fails to simulate the design during the reconstruction phase as the matrices involved would require over 50GB of memory. To compensate for this, simplified simulations are performed on planar and round inclusions excluding the permeable membrane as shown in Figure 3.2. Future iterations of the reconstruction software should consider switching to more efficient EIT reconstruction software such as the C++ numerical solver developed by Jehl *et al*.
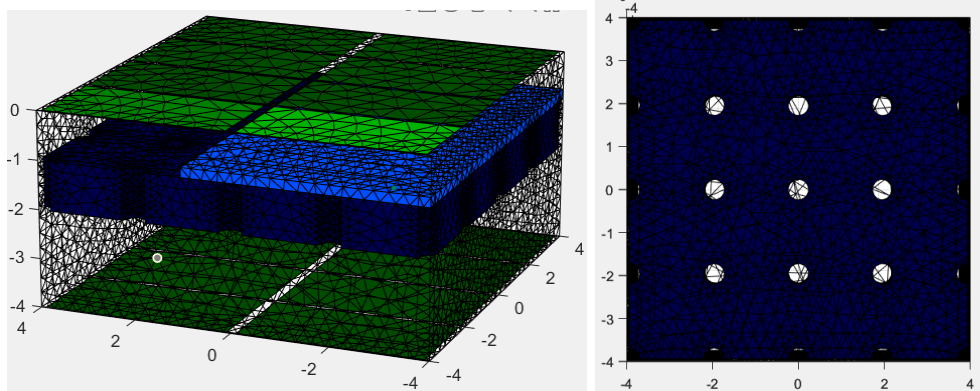
Figure 3.11 Mesh generation of planar inclusion resting atop permeable membrane mesh.

For the first validation test platform, electrodes were made as large as possible to increase the sensitivity to the area immediately in front of the electrode surface. The surface area of the plate is 16 cm^2 and the distance between plates in the two test systems is fixed at 40 mm, Figure 3.12. Electrodes are configured in 2x2 arrays.

Data was imported to EIDORS in a similar manner as the Python script. Serial data was imported from the CSV file, but it had to first be processed into a format that would comply with the forward model structures in EIDORS. For this, we employed the algorithms developed by Zamora-Arellano *et al*. [46] that provided a foundation for using imported data in EIDORS. For an implementation, see importHomoAndInclusionData.m in the GitHub repository [37]. For each design, a custom EIDORS mesh model must be created, which has to be done from implicit knowledge of the test body. The stimulation and measurement patterns are extrapolated from the CSV data file and these define the stimulation profiles used by the EIDORS forward models. With the forward model defined, a course mesh is defined to map the inverse model to the forward model. From this point, the regularization parameters are defined, which is a task that is unique to each system and must be rigorously tested for. Finally, an inverse solver method reconstructs the image from the homogenous test data and the inclusion test data provided in the CSV files. The first validation of the system can be seen in Figure 3.12, which depicts a PDMS insulating phantom covering most of the current carrying electrode plane.
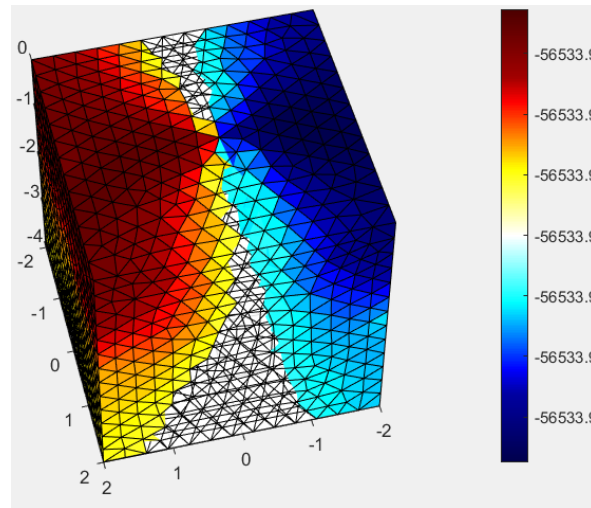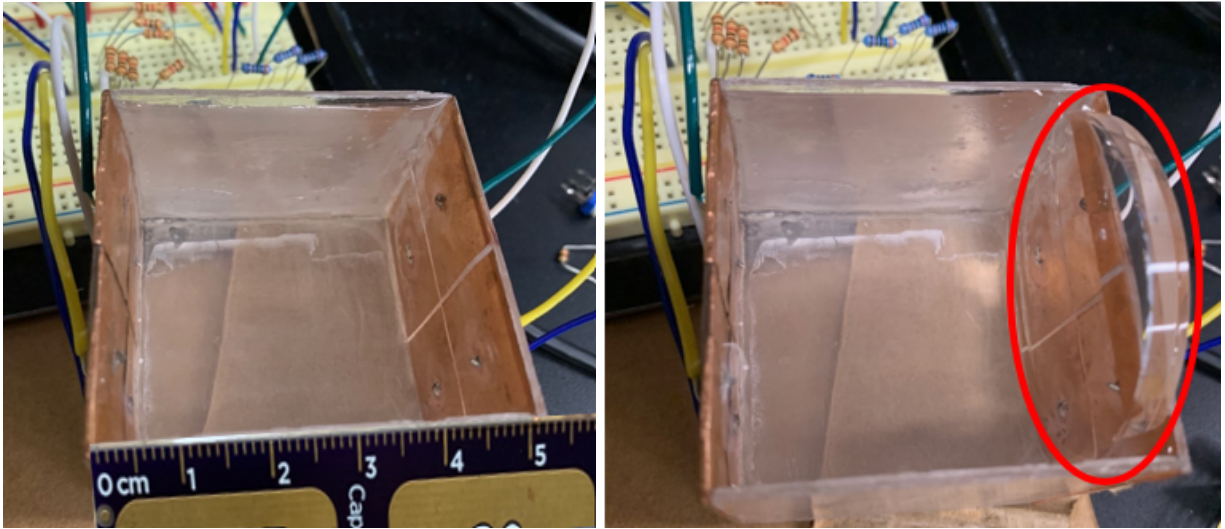
Figure 3.12 Prototype validation tank. Top left, homogenous tank with conductive saline solution. Top right, inclusion on the rightmost electrode plane (top plane). Bottom, the first reconstructed image from the system. The insulating inclusion is properly oriented on the rightmost electrode plane. The reconstruction does have issues as a large high conductivity inclusion is also depicted on the opposite electrode plane. For an analysis of the conductivity range, see "Effects of the Ill-Posed Inverse Problem" in the Appendix.

An important decision in voltage measurements is the inclusion or exclusion of current carrying electrodes. As has been discussed, the current carrying electrodes produce an electric double layer that impacts the impedance, primarily at low frequencies. Excluding these measurements reduces the effect that electrode contact impedance has on the measurements

[19][63]. The unknown contact impedance dominates at low frequencies, seen in Figure 1.6. In the final reconstruction, the decision has a significant effect on the reconstructed image shown in Figure 3.13. Both figures use the same dataset from Figure 3.12, but whenever a current carrying electrode is detected, that electrode data is ignored. Due to the ill-posed nature of the problem, the difference in data has significant effects on the reconstructed image [46]. This small change in data representation has led to the reconstruction placing the inclusion across the face of the top electrode plane or isolated to the top half of the plane, losing half of the reconstruction clarity. This effect is similarly seen with simulation data, in Figure 3.14, indicating that this effect is not due to measurement errors but the contribution of the electrode contact impedance.
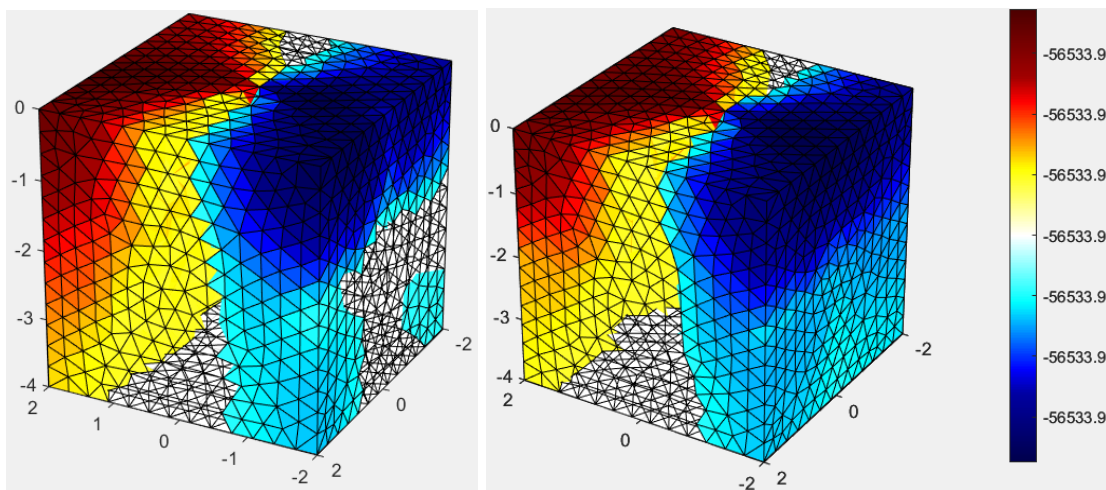
Figure 3.13 Effects of including current carrying electrodes in voltage measurements. Left, reconstruction with current carrying electrode data. Right, current carrying electrode data is removed from the dataset. Half of the inclusion shape is lost in the reconstruction using current carrying electrodes.
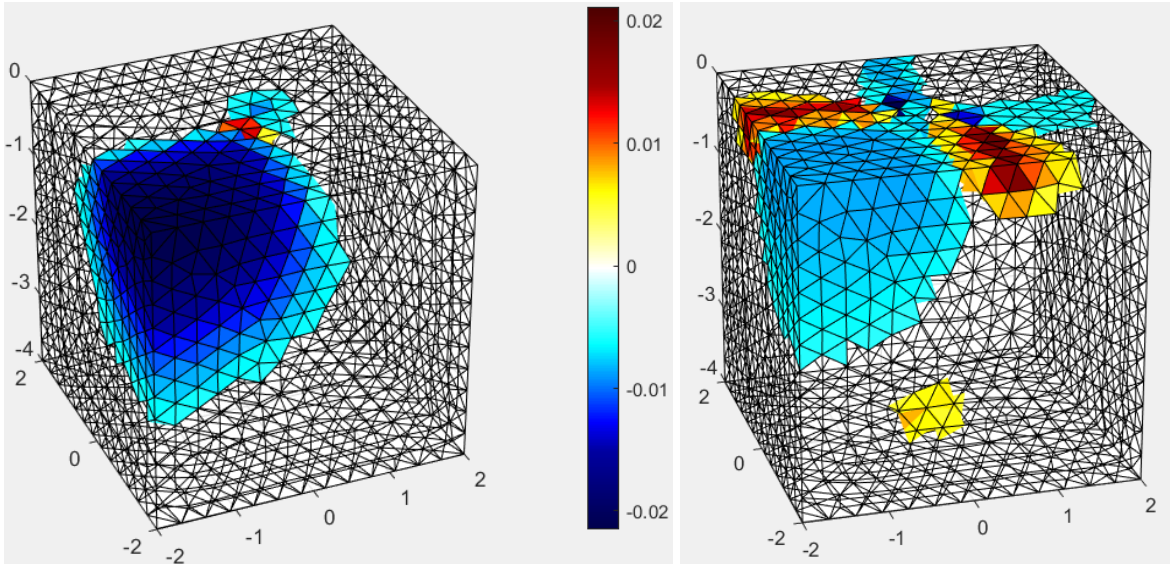
Figure 3.14 Simulation of current carrying electrode data impact. Left, reconstruction with current carrying electrode data. Right, current carrying electrode data is removed from the dataset.

Proof-of-concept testing was performed with a system consisting of 2x2 electrode planes with an area of 6.76 mm^2, spaced at 40 mm. Measurements were first taken from a homogenous saline solution of 160 mM KCl solution with a conductivity of 20 mS·cm^{-1}. PDMS inclusions and conductive bodies were then added to the test chamber and reoriented to test the systems sensitivity to minor location changes. While there is evidence that orientation is detected, it is the location that proves to be difficult for the model to detect.

Figure 3.15, shows different reconstructions of an inclusion on the bottom plane shifted to cover one side of electrodes, then the other. These figures emphasize two points: sensitivity and orientation detection. Sensitivity is the overall reconstruction accuracy to the inclusion's conductivity and orientation detection is the accuracy that the reconstruction is in the correct location, is the correct size, and is the correct shape. This is illustrated in Figure 3.15 as the middle reconstructions include current carrying electrode data and the rightmost reconstructions ignore that data. In the top reconstructed images of the inclusion, a PDMS rectangular phantom was placed on one side of the chamber and shifted to the other side on the next measurement. The bottom plane is correctly dominated where the inclusion is placed, but there is poor

detection of the orientation of the object which does not move between reconstructions. This demonstrates higher sensitivity for these reconstructions, but poor orientation detection. In the bottom figures, the reconstruction is more aware of the orientation but less sensitive. Primarily, the object is reconstructed on the wrong plane. This clearly lacks spatial sensitivity, but the orientation of the reconstructed inclusion is centered on the correct side of the x,y plane, shifting from (-1,-1,0) to (1,1,0).
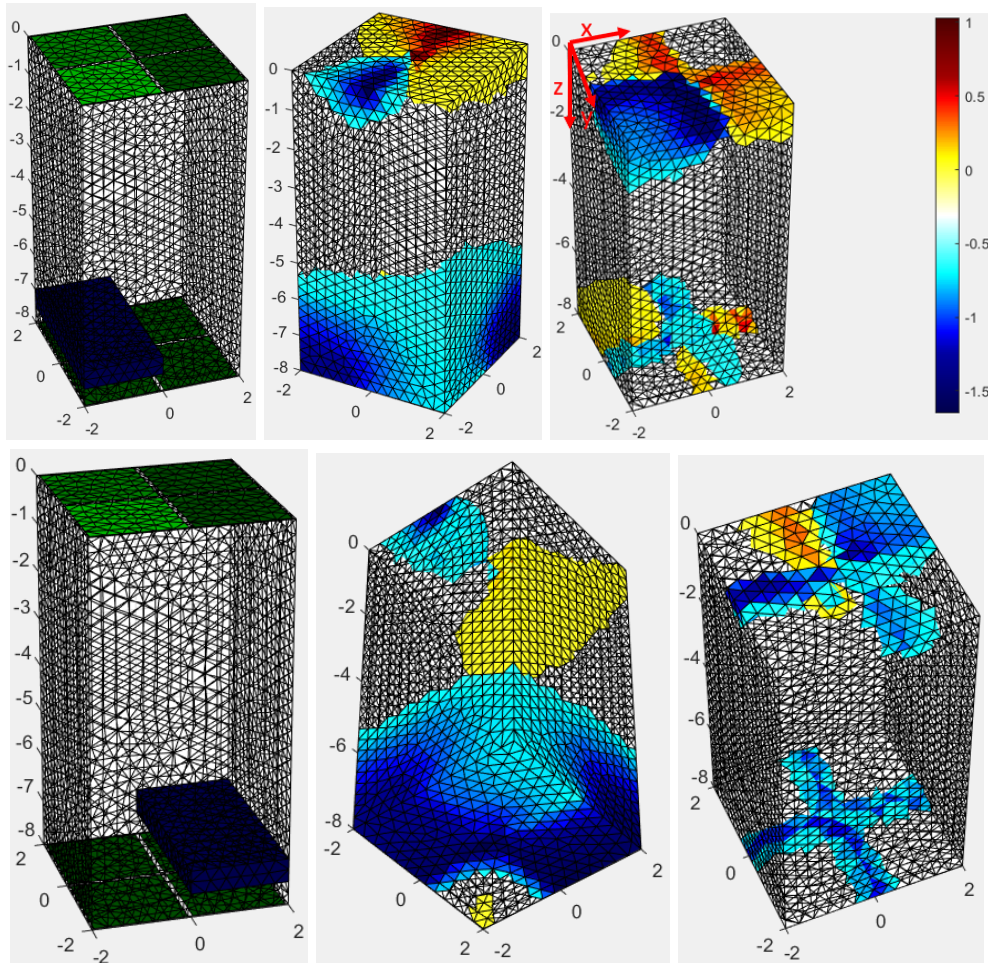
Figure 3.15 Deeper chamber test with actualized EIT platform. Left, inclusion orientation within the chamber. Inclusion is placed on bottom plane at z = -7. The inclusion is shifted from left to right between tests. Middle, reconstruction with current carrying electrode data. The sensitivity accuracy is correct but the orientation does not change between measurement frames. Right, current carrying electrode measurements are removed. The reconstruction has better orientation detection but has worse sensitivity. The inclusion is on the correct side but is half the size with more artifacts.

When the PDMS inclusion is moved to cover the top electrode plane, the reconstruction algorithm is more sensitive and has higher orientation detection. In Figure 3.16, the inclusion is correctly predicted on the top electrodes plane, but with few artifacts. In an ideal reconstruction, only the large blue inclusion would be present, but due to the lack of measurement electrodes in a 2x2 electrode system, the reconstruction is more sensitive to errors (e.g., AD736 conversion errors). There is a tradeoff in improved orientation detection. Movement of the inclusion resulted in a similar image, indicating low orientation detection on one half of the plane, but higher sensitivity to objects near the electrode plane.
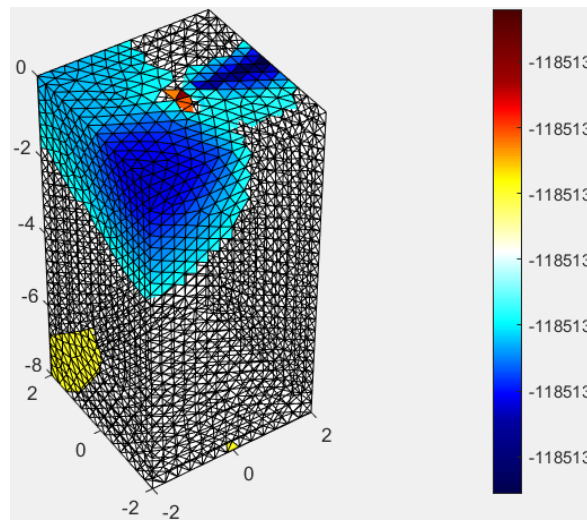
Figure 3.16 Spatial detection of inclusion on the top plane covering the leftmost electrodes.

Further testing was conducted on shallower chambers, with 2x2 electrode planes with an area of 6.76 mm^2, spaced at 26 mm, or 1:1 depth-to-length ratio chambers. Unfortunately, reconstructions with bodies in the middle plane were inconclusive. As will be explained, hardware issues plagued the design and prevented higher electrode count systems from being utilized. These results indicate that the TEER system has the best sensitivity near the electrode planes, reflecting the reconstructions in Table 3.3. Modifications to the present system can be implemented to fully realize spatial detection in deeper areas of the tank, such as a lower ratio of chamber depth-to-length (e.g., 0.5:1). A fully realized system would naturally be inclined to

have the target inclusion closer to one electrode plane to take advantage of higher sensitivity

closer to electrodes.
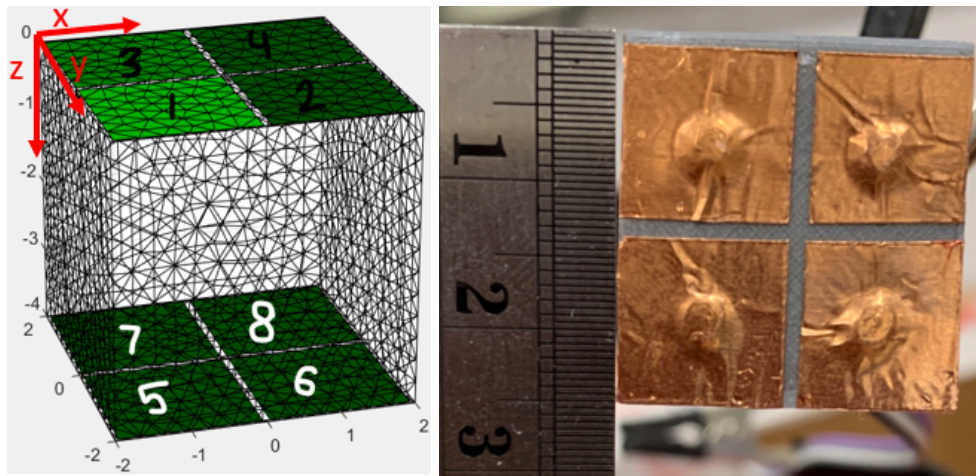
Figure 3.17 Real electrode channel location compared to reconstruction model. Left, the reconstructions

do not display the electrode locations, so the reference x,y,z axis will be added. Right, the 2x2 electrode

plane and measurement scale.
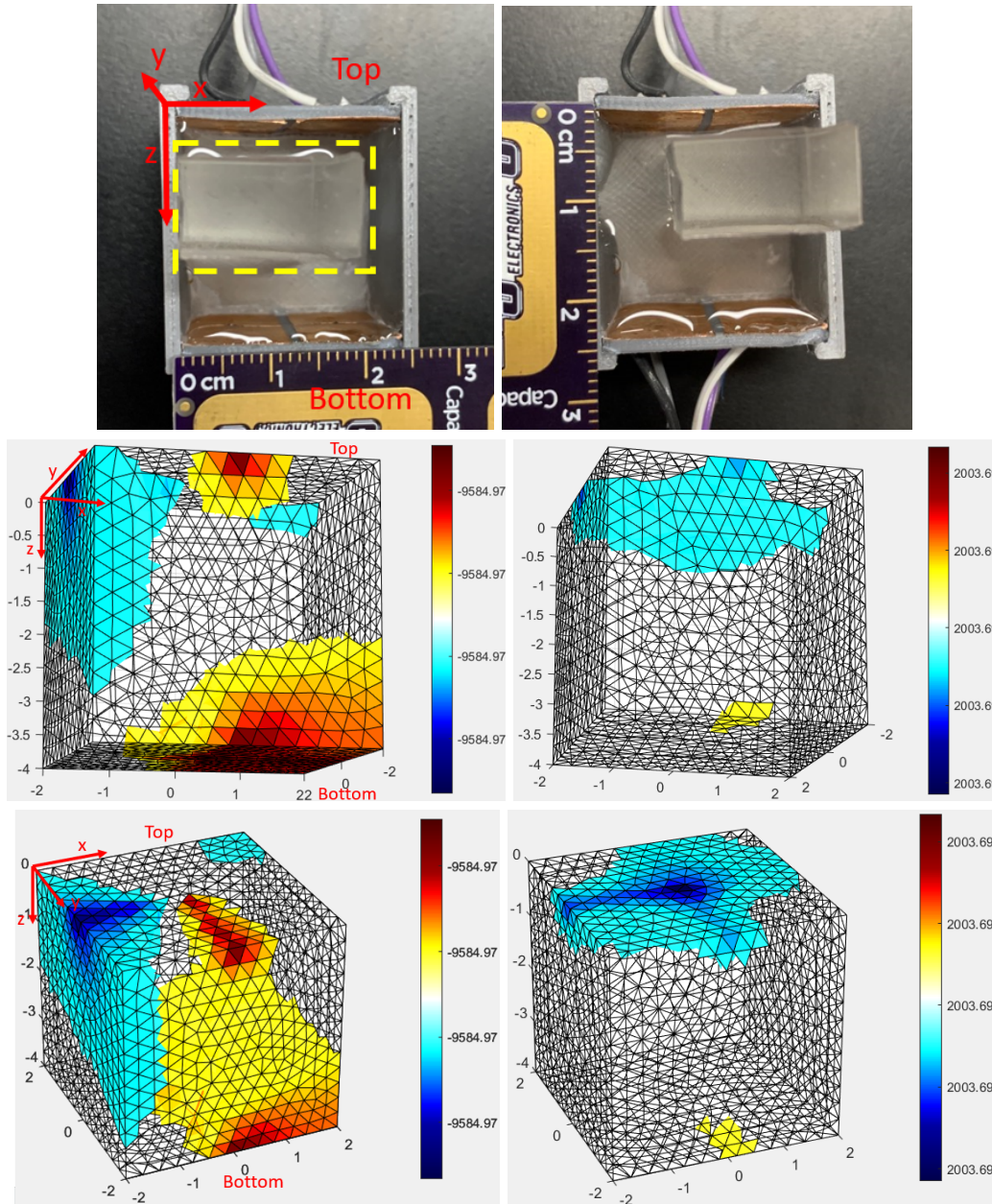
Figure 3.18 Large PDMS inclusion in 4x4 electrode chamber. Top left, Insulating PDMS inclusion, outlined in yellow, is placed near the top electrode plane. Top right, PDMS phantom is moved to the opposite side on the top plane. Middle left, phantom is detected on the correct side of the tank for this reconstruction with the correct conductivity. The spatial detection is inaccurate and reconstructs an incorrect shape. The reconstruction is oriented to resemble the testing tank image. Middle right, phantom orientation is incorrect but the reconstructed inclusion has a lower conductivity to the background which reflects the testing setup. Bottom: The reconstructions are shifted to better visualize the top plane to represent the orientation of the inclusion.

Further experiments were conducted with more complex electrode planes. Three bodies were designed with 2x2, 3x3, and 4x4 electrode planes. Testing with the 2x2 planes proved to be the system's limit as reconstructions in higher electrode systems were dominated by artifacts with poor sensitivity and orientation detection for the inclusions. Throughout the design process, repeated soldering and desoldering of components during the debug phase had damaged voltage buffers and connected electrodes. This resulted in high voltage measurements at the ADCs that caused malfunctioning when certain functions were called in the firmware. Even with redundant circuitry, measurements were too variable when connected to electrode planes with more electrodes. For in depth information on the hardware debug related to the ADCs, see "Transient Issues in Current Injection and Analog-to-Digital Conversions" in the Appendix. To work around the issues, a waveform was generated with a Digilent Analog Discovery waveform generator which acted as the input to the VCCS and the output was a constant 7.0 μA_{RMS} at 1 kHz and 50 mV_{pp}. This proved to keep the system stable and addressed the current spiking problems.

Spatial reconstruction was successful for a copper test strip inserted into the test tank. Figure 3.19 shows the location of the strip, centered between the electrodes, midway into the tank, and offset from the top electrode plane. The EIDORS model successfully recreates the image with the proper spacing, depth, and orientation of the strip. The reconstruction fails to accurately portray the strip's conductivity, as it should have hotter colors associated with a more conductive material. Unfortunately, the system is limited by the available electrodes, and significant variance is seen in reconstructions. The reconstruction process begins to express more artifacts when the strip is justified to the left and right sides of the tank, Figure 3.20, showing better detection on the left side over the right, a consistent outcome from previous experimentation.
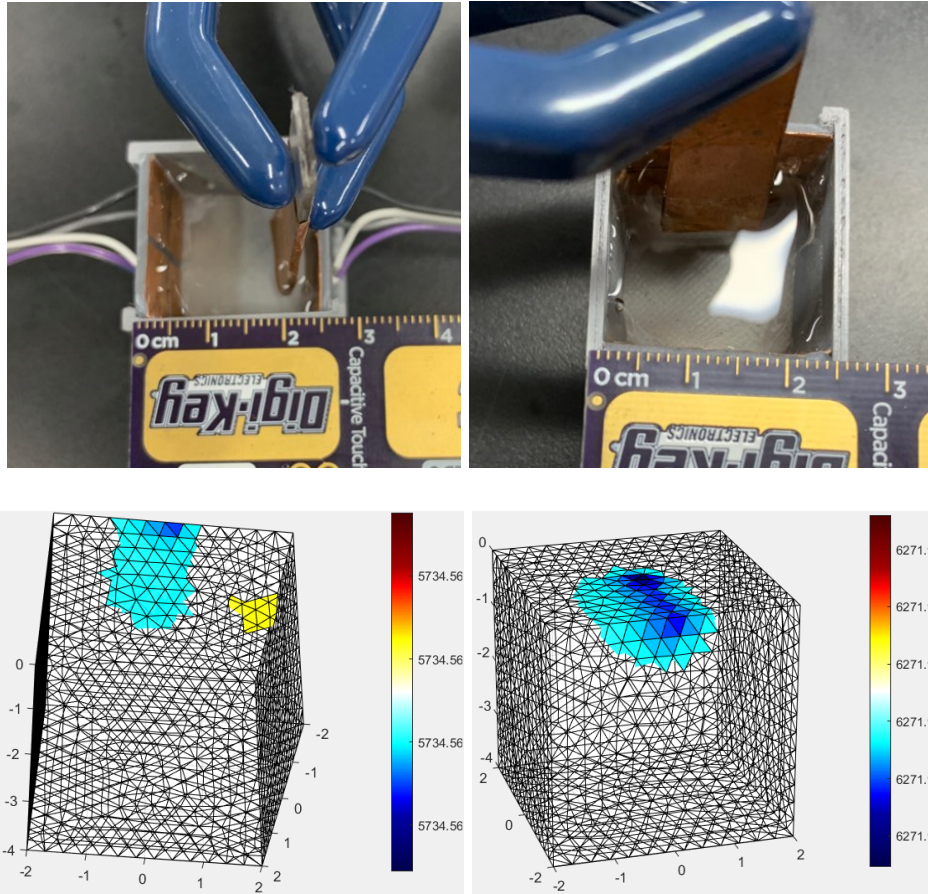
Figure 3.19 Improved spatial detection with conductive strip. Top, The layout of the conductive copper strip in the testing tank. The strip is placed halfway between electrodes and close to the top plane. Bottom, correct spatial detection of the orientation and depth of a conductive strip inserted into the chamber. The left image reflects the testing chamber layout and the right image displays the reconstruction when viewed from the top electrode plane.
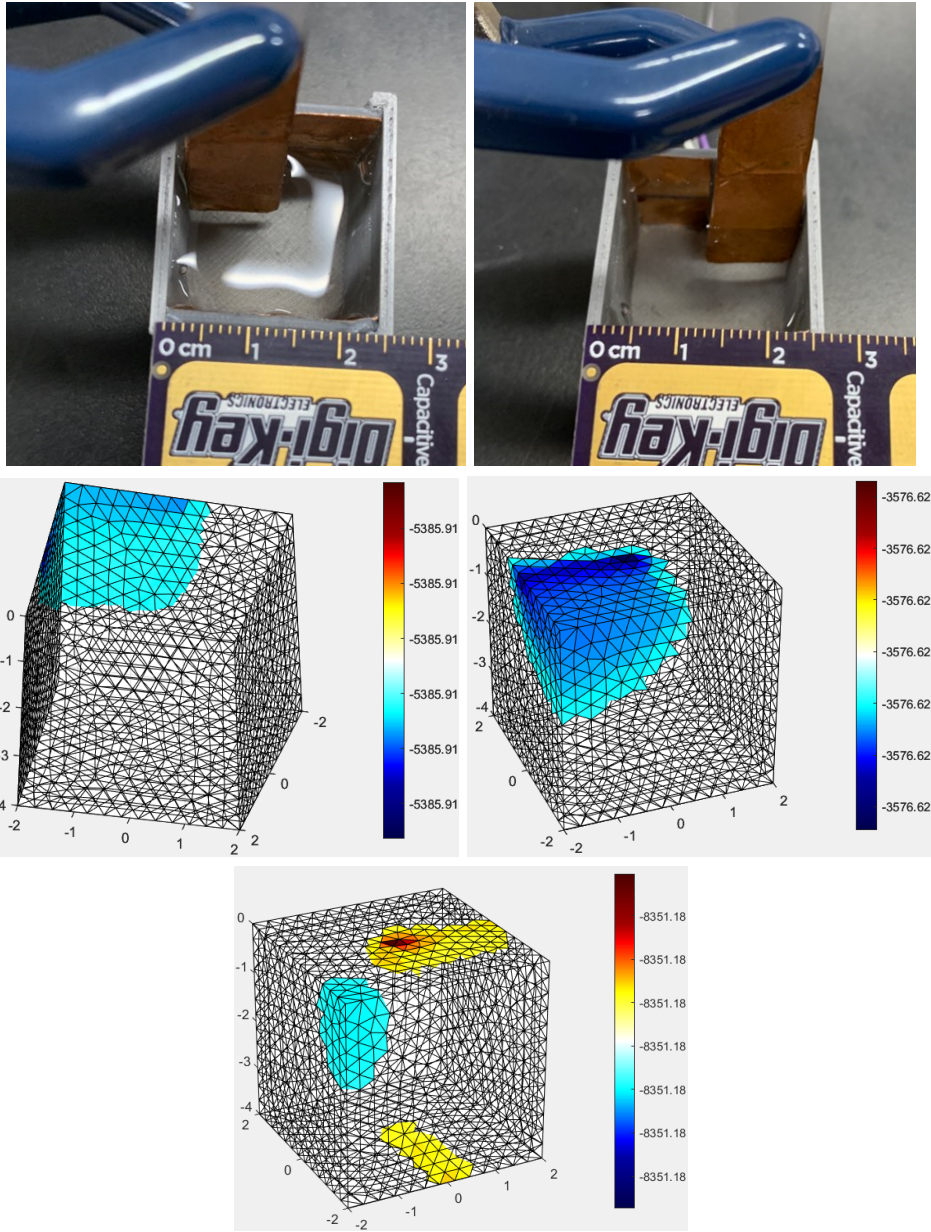
Figure 3.20 Reorientation of conductive strip shows decreased detection nearest the chamber sides. Top left, conductive strip is inserted in the top plane, justified to the left and offset from the plane. Top right, similarly oriented strip, but justified right. Middle left, reconstructed inclusion is on the correct plane under the correct electrodes but the entire length of the strip is not correct as it does not extend to the bottom of the chamber. Middle right, reorientation of the reconstruction to be viewed from the top electrode plane. Bottom, poor reconstruction accuracy is seen when the inclusion is justified to the right side of the chamber.

Testing with a round inclusion, Figures 3.18 and 3.21, reveals an image close to the simulated inclusion in Figure 3.2. The ball is correctly oriented at (-1, -1, 0), but the large amount of artifacts detract from the image accuracy of reconstruction. Similarly, Figure 3.21, reconstructs an inclusion on one edge of the system, displaying the system's poor reconstruction for objects justified to the right side of the chamber.
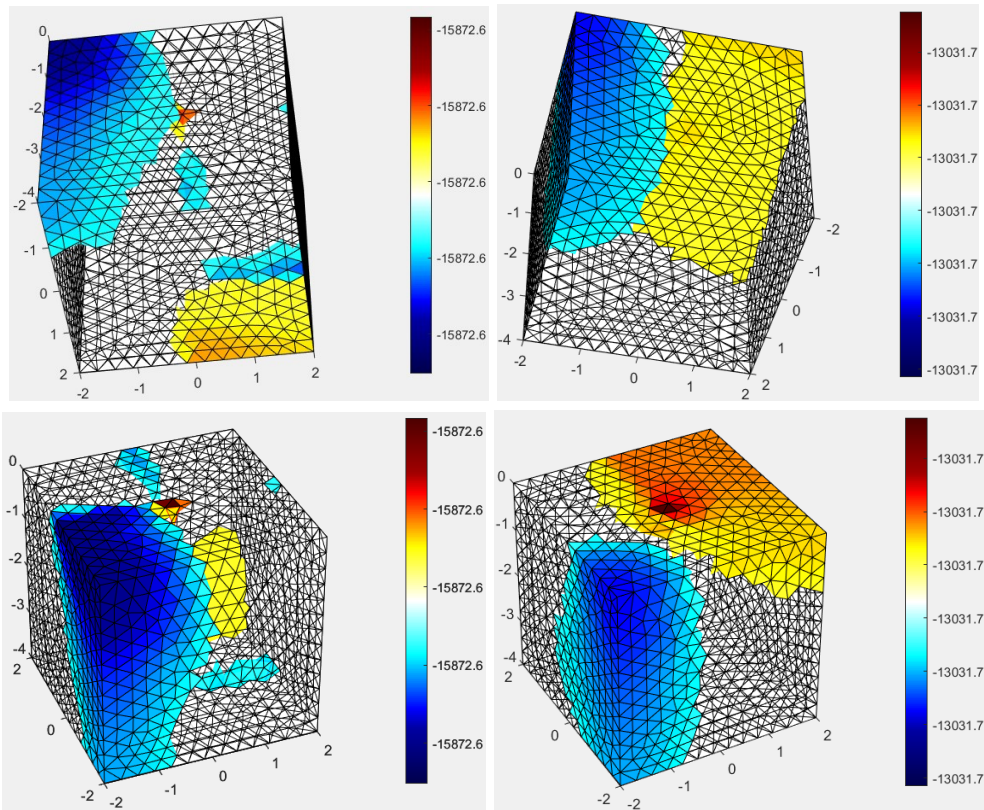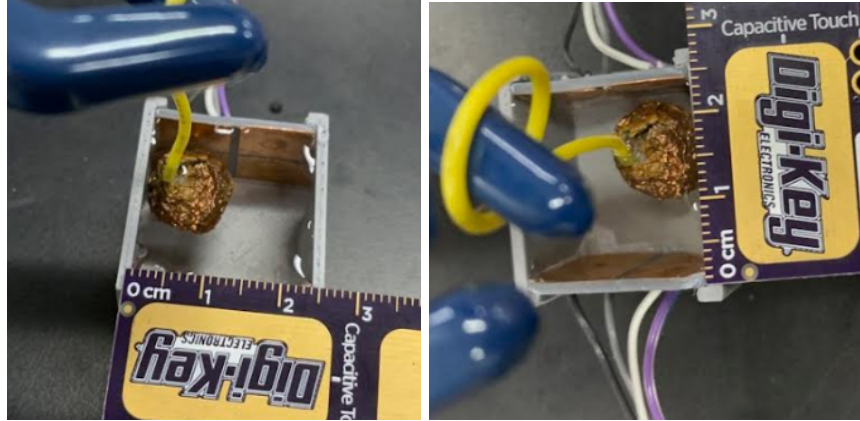
Figure 3.21 Reconstructions with conductive spherical inclusion. Top left, spherical inclusion near top electrodes, under electrode 0. Top right, inclusion is moved to the opposite side of the chamber under electrode 2. Middle left, reconstruction shows good spatial detection of the spherical object, but does not reconstruct the shape accurately. Conductivity is also misrepresented in the reconstruction. Middle right, the reconstruction shows a planar inclusion on the correct side of the chamber. The conductivity reconstruction is correctly represented but the shape and depth of the inclusion are inaccurate. Both images are displayed to reflect the actual testing tank figures. Bottom, the reconstructions are reoriented to be viewed from the top electrode plane.

Testing was conducted near the bottom plane too. Spatial detection was poor for the conductive strip inserted a shallow distance into the chamber. The reconstruction in Figure 3.22 shows the correct quadrant of the chamber, but the inclusion is displayed on the wrong side. This is not the case when the strip is inserted deeper into the system, where the strip in Figure 3.23 contacts the bottom of the chamber and covers both electrodes. The reconstruction is rotated to display a bottom-up view. In this figure, it is evident that the conductive strip is represented as an inclusion oriented halfway across the bottom plane, which reflects the real-world location. High variability in the performance of the system can be reduced by more precise measurements, but the first step is increasing the electrode count. This reconstruction affirms the viability of this system for larger inclusions. Minor spatial detection is yet to be realized, but major spatial changes have successfully been measured and displayed by the system.
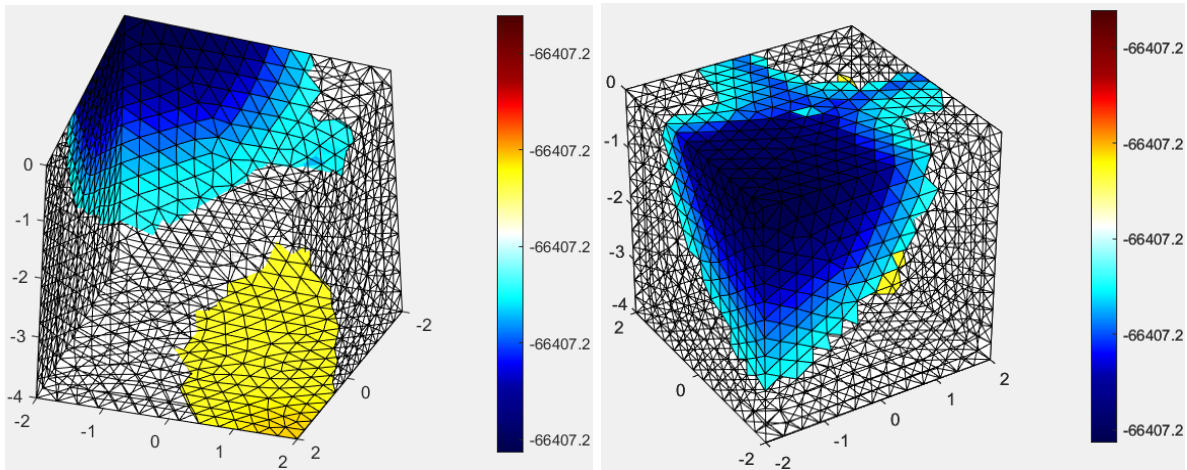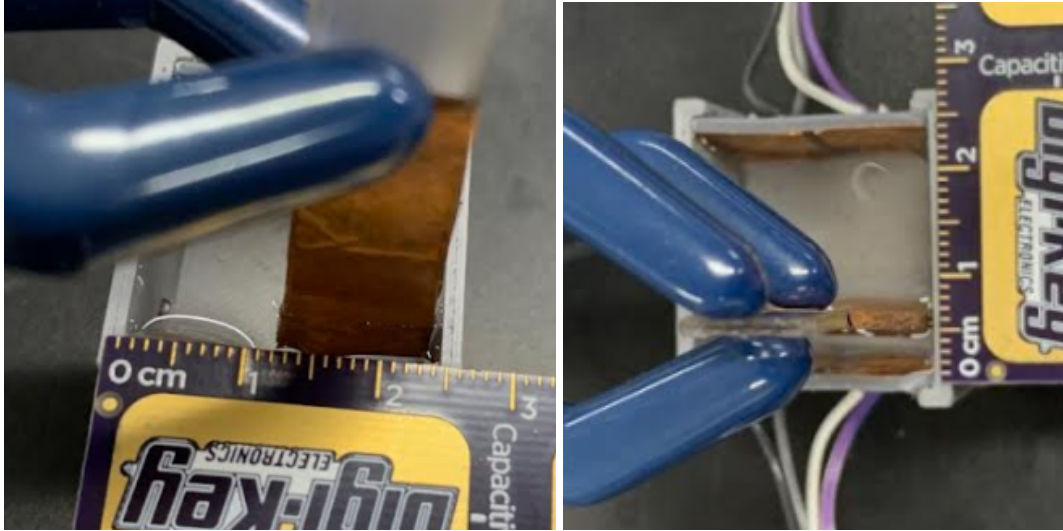
Figure 3.22 Single electrode covered on bottom plane. Top, the conductive strip is oriented directly in front of electrode 5. Bottom, the reconstructions show the correct shape of the inclusion, but inaccurately display the depth and conductivity. The right figure is oriented for viewing from the top electrode plane.
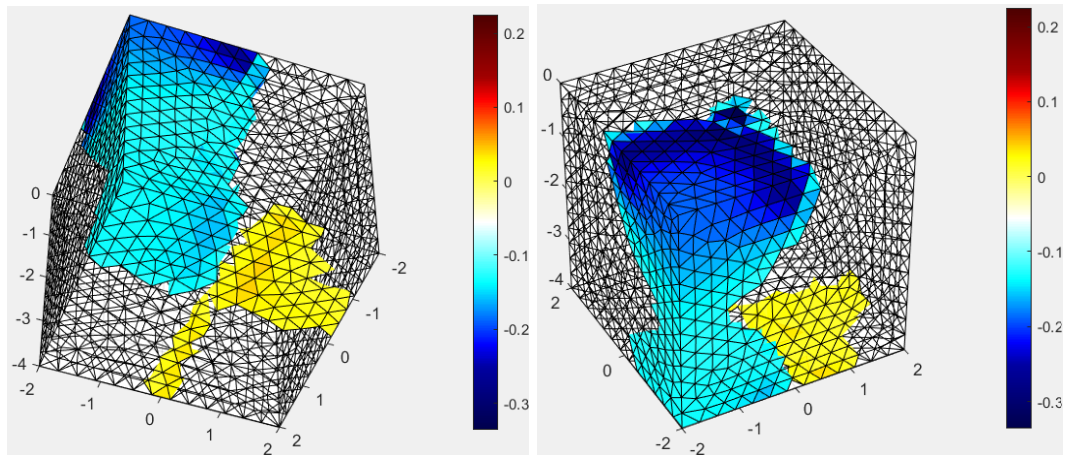
Figure 3.23 Conductive strip is inserted deeper into the testing chamber. Top, the strip is inserted to the maximum depth of the chamber. Bottom left, the view of reconstruction for conductive plate in front of electrodes 5 and 7 on the bottom plane. Bottom right, the same figure but oriented for viewing from the top electrode plane

Chapter 4 - Conclusion

In this work we have shown the potential of an entirely distributed TEER system capable of tomographic imaging. The proposed device functions entirely from a 12.7x15.2 cm^2 PCB and reports data with only a USB serial connection. This device demonstrates spatial resolution of conductive and insulating samples for a variety of orientations even with a limited number of electrodes (2x2 array). Future works will expand on this work by increasing the electrode count for higher resolution imaging, higher frame capture times, and operation within an incubator for lower variability in OoC samples.

This hardware design application was affected by hardware failures that required testing and debugging at every stage. More stringent testing of hardware outside of simulation is necessary to determine the efficacy of each component, as small hardware issues have a compounding effect on the reconstruction process. Even disconnections of one electrode or failures of a single voltage buffer stage can have significant adverse effects. Through all of this, we have completed the design of a system capable of crude spatial resolution for inclusions between parallel planar electrode arrays. Despite the issues that prevented high precision image reconstruction, this work clearly demonstrates the viability for a TEER system to reconstruct the spatial location of inclusions with the potential for significant image improvements.

Future Directions

The current system could be improved to provide higher rates of data throughput. As the system currently functions, it takes ~30 minutes for full data acquisition in 3x3 electrode systems. This is a worst case scenario as we increased the delay time for each channel to ensure settling between channel switching. There are many timing optimizations that can be made and it is expected that future iterations will have a higher frame rate that can reasonably accommodate higher electrode counts.

Improvements to the measurement system are possible. Currently, the system performs two RMS-to-DC measurements per iteration, but many more single-ended conversions can be made. With the current system, up to eight conversions can be made, essentially taking an entire voltage sample from an eight-electrode configuration at once. There are other alternative measurement schemes. In prior literature reviewed, differential amplifiers as voltage measurements were used, which could be implemented to increase measurement frame acquisition. This would allow the system to use the proposed peak detector system. One electrode in each image frame is a common electrode connected to virtual ground so that electrode could be the differential voltage measurement reference. The ability to swap the virtual ground between electrodes also allows flexibility among measurement techniques to allow for more optimization as different measurement pattern algorithms are tested, such as adjacent and trigonometric patterns, which is a clear advantage over current state of the art systems like the ACT3.

Higher throughput can be achieved on the ADCs with the addition of four more measurement circuits. The ADCs offer up to four single-ended channel measurements for RMS-to-DC systems and two differential measurements for peak detector circuits. Single ended mode can only measure positive values, which makes it ideal for the RMS value or peak value of a sinusoidal signal. Depending on reconfigurations of the circuit, anywhere from 2-8 signals can be measured, which would significantly decrease frame acquisition time. The addition of more ADCs would also improve the throughput, as four ADCs can be chained together on one I2C line for a total of 16 measurements. The Teensy 4.0 board supports two I2C buses, allowing 32 measurements to be taken rapidly.

This device is intended for use within an incubator necessary for cell cultures. This requires isolation from the humidity that has the potential to corrode electrical contacts and degrade the system. An hermetic chamber is out of our design capabilities, but using a chamber mold that stores the system with rubber gaskets, we expect to limit humidity exposure. The

addition of desiccants can also aid in maintaining a safe environment for the electronics. For this

purpose, the DHT11 humidity and temperature sensors were added to provide real time

monitoring of the health of the enclosed system.

Appendix
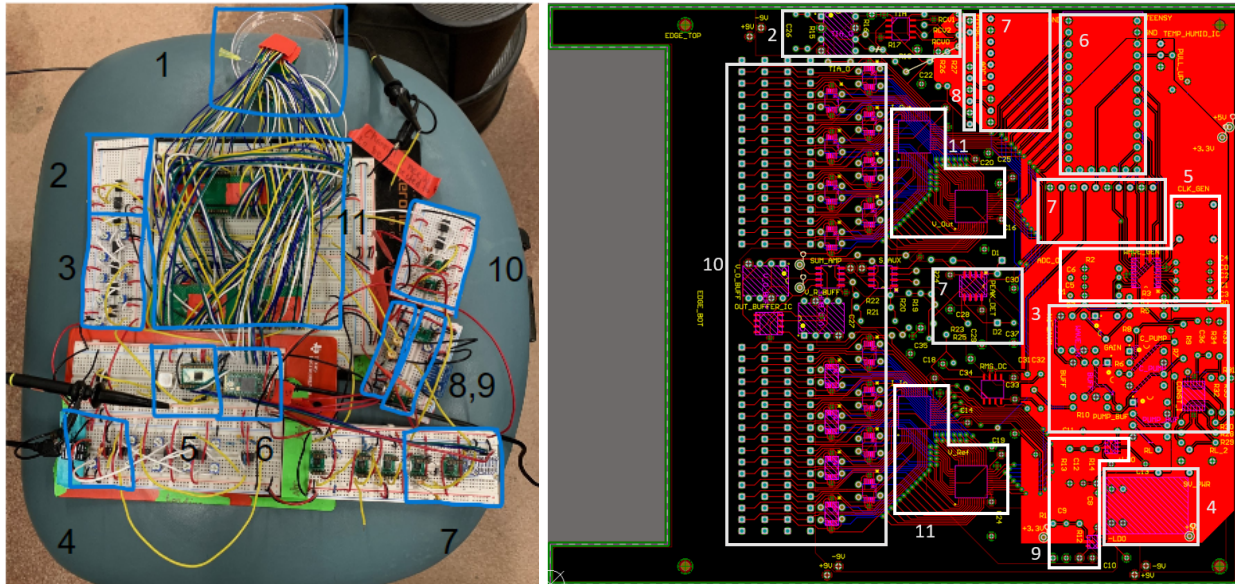
Figure A.1 First prototype breadboard implementation of design excluding voltage buffers, compared to second prototype on a PCB.

Components: 1) PDMS Test Chamber on 2x 32 pin electrode PCBs. 2) Transimpedance amplifier for C-to-V conversion. 3) Constant Current Source (Modified Howland Current Pump). 4) 9 V Power Brick. 5) AD5930 Programmable Waveform Generator and 50 MHz clock oscillator. Teensyduino 4.0 (Microcontroller). 6) Teensy 4.0 Development board 7) Peak detector (AC-DC converter) and AD1115 ADC. 8) Phase detector. 9) Low dropout voltage regulators, +/- 2.5 V. 10) Voltage sense signal buffers and differential amplifier.11) 32 pin multiplexers (2x) and demultiplexers (2x).

Table A.1 100 Hz Simulated values

100 Hz	R_{Load} (Ω)			
Probe Trace	100	1K	5K	10K
V(HPF)	270.292m	272.289m	282.795m	287.208m
V(VCCS_OUT)	900.073u	9.0754m	47.131m	95.735m
V(TIA)	-900.975m	-907.629m	-942.649m	-957.358m
I(R_{Load})	9.0097u	9.0592u	9.4104u	9.560u
I(TIA)	9.0097u	9.0763u	9.4265u	9.574u
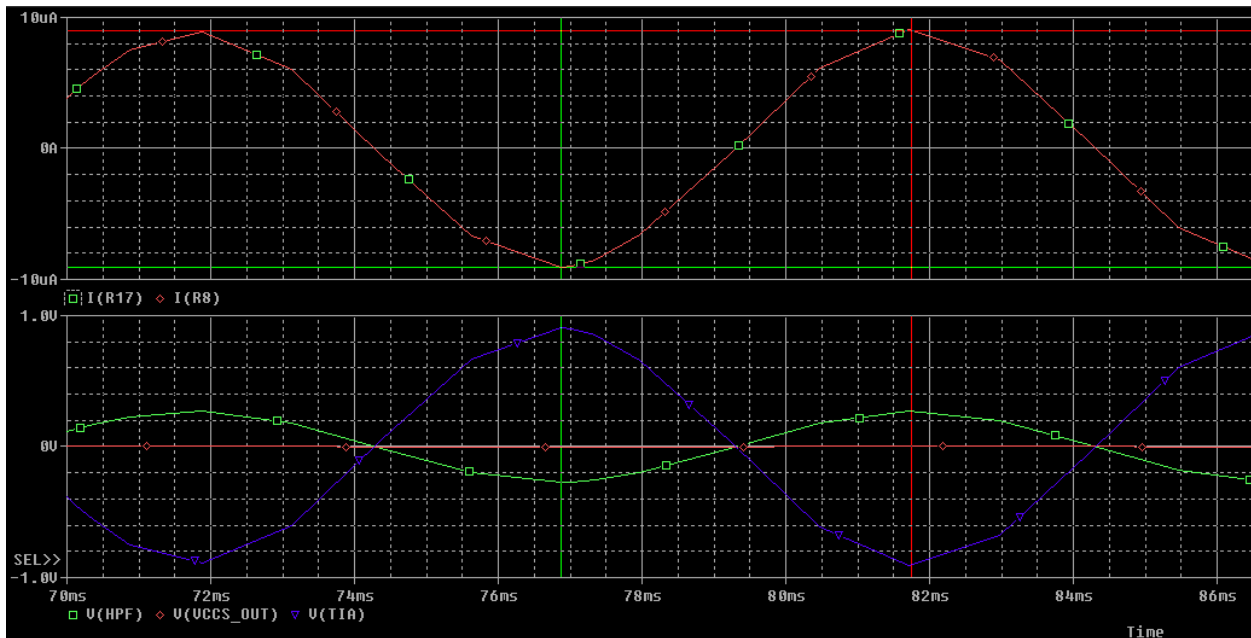
Figure A.2 100 Hz VCCS waveforms. The current is seen at a nearly ideal 10 μA.

Table A.2 1 kHz Simulated values

1 kHz	R_Load (Ω)			
Probe Trace	100	1K	5K	10K
V(HPF)	281.208m	287.963m	289.233m	286.549m
V(VCCS_OUT)	936.421u	9.598m	48.204m	95.515m
V(TIA)	-937.359m	-959.876m	-964.108m	-955.163m
I(R_Load)	9.3715u	9.599u	9.641u	9.552u
I(TIA)	9.3736u	9.599u	9.641u	9.552u
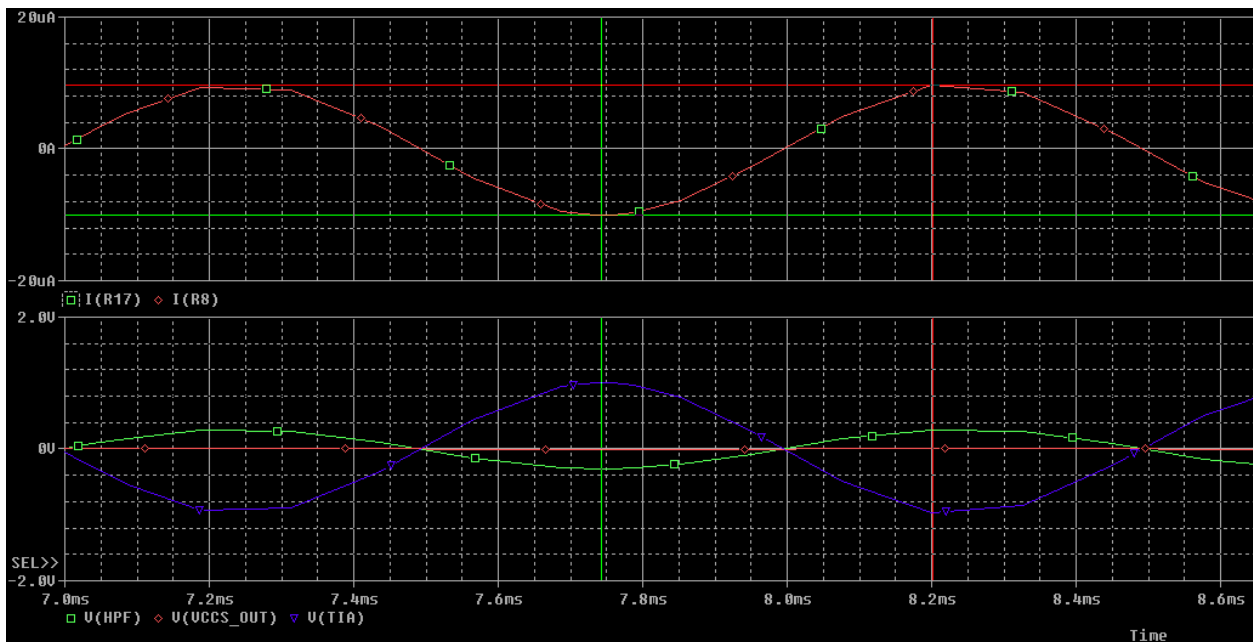
Figure A.3 1 kHz VCCS waveforms

Table A.3 10 kHz Simulated values

10 kHz	R_{Load} (Ω)			
Probe Trace	100	1K	5K	10K
V(HPF)	288.502m	277.417m	277.893m	277.627m
V(VCCS_OUT)	960.711u	9.2463m	46.315m	92.541m
V(TIA)	-961.674m	-924.724m	-926.309m	-925.423m
I(R_{Load})	9.617u	9.2472u	9.2629u	9.2542u
I(TIA)	9.617u	9.2472u	9.2631u	9.2542u
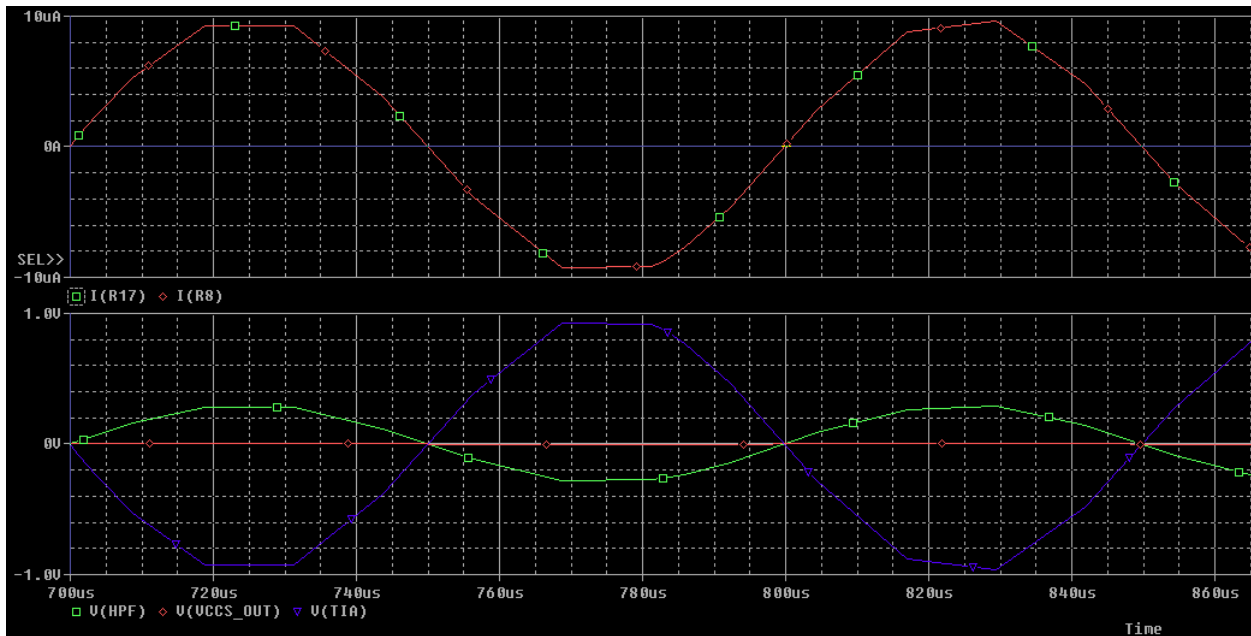
Figure A.4 10 kHz VCCS waveforms

Table A.4 100 kHz Simulated values

100 kHz	R_{Load} (Ω)			
Probe Trace	100	1K	5K	10K
V(HPF)	277.184m	277.282m	277.162m	277.189m
V(VCCS_OUT)	923.020u	9.2418m	46.193m	92.395m
V(TIA)	-923.945m	-924.274m	-923.874m	-923.962m
I(R_{Load})	9.2394u	9.2427u	9.2387u	9.2396u
I(TIA)	9.2394u	9.2427u	9.2387u	9.2396u
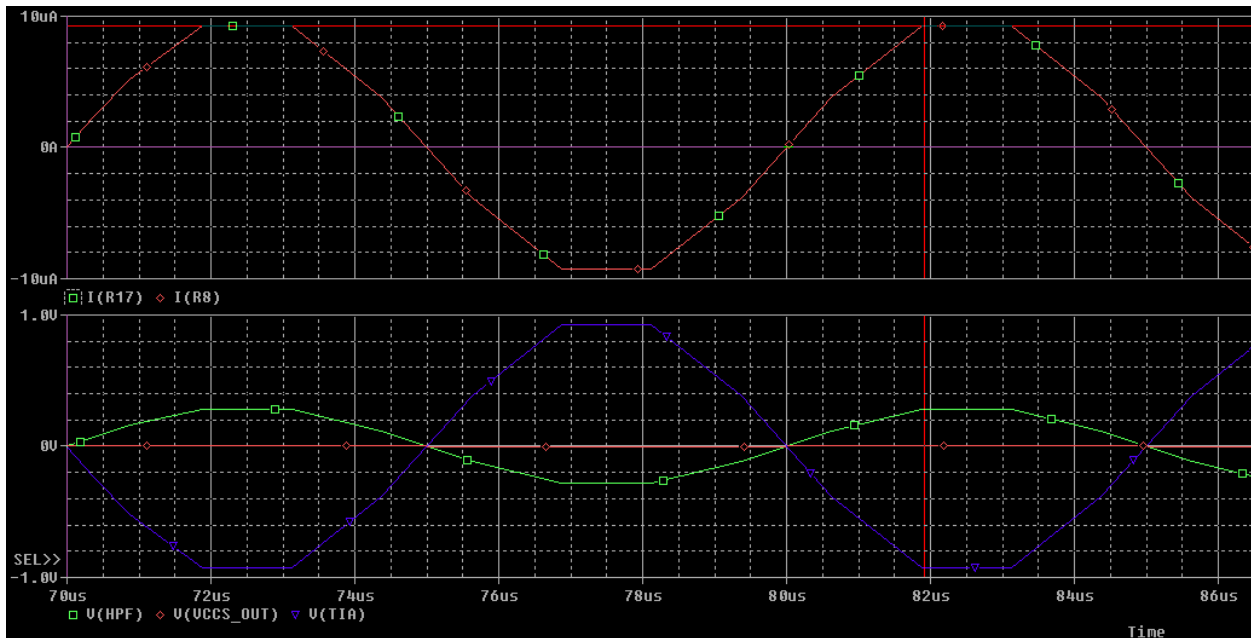
Figure A.5 100 kHz VCCS waveforms

84
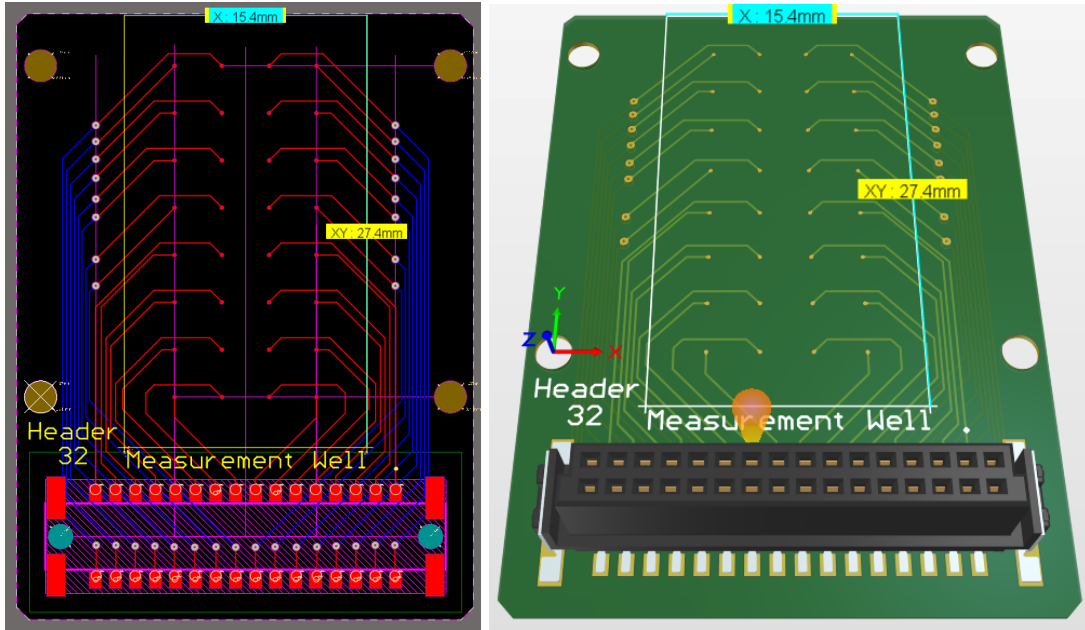
Figure A.6 Proposed microelectrode array structure with 32 pin header for easy connections.

Debug and Troubleshooting

Some components of this system required in-depth debug outside of standard testing. Characteristics of components could be undocumented in the datasheets or malfunction from unforeseen design choices. This section documents the steps to correct issues that presented themselves in this work and the resources used to solve the problems.

AD5930 F$_{START}$

As it is not explicitly described in the datasheet, we find it necessary to comment on frequency programming of a Direct Digital Synthesis (DDS) device. In early naive approaches, the F$_{START}$ register was programmed to 100, and the measured frequency was 300 Hz. The same was true for 10 outputting 30 Hz and any starting frequency being three times the intended frequency. In a DDS, F$_{START}$ is known as a "binary tuning word." There is a useful formula for calculating the binary tuning word to express the desired output frequency, F$_{OUT}$.

$$F_{OUT} = \frac{M \cdot REFLCK}{2^N},$$

where M is the binary tuning word, REFCLK is the internal reference clock frequency, and N is the bit length of the phase accumulator. The AD5930 has a 24-bit phase accumulator, and the reference clock is generated with a MXO45HS-3C-50M0000 clock oscillator. For a 100 Hz output frequency, F_{START} should be programmed as 33, and testing confirms the output at 98 Hz. This pattern reveals that the desired starting frequency should be programmed with the scaling factor of 3 Hz/bit.

Power Issues

The multiplexers of this device work on a +/-2.5 V dual supply to comply with the needs of AC signal transmissions through the analog multiplexers. For safe operation of ADG732 multiplexers, the voltage between V_{DD} to V_{SS} has an absolute maximum rating of 7 V. For the analog inputs, the maximum rating is V_{SS} - 0.3 V to V_{DD}+0.3 V [36]. Operation within these ranges is key to the correct function of the device, which is why large voltage fluctuations on the +/-2.5 V LDOs had a significant impact on the development of this system. During the breadboard stage of the device, the +/-9 V and +/-2.5 V power rails operated as expected until voltage buffers were added to channels at the output of the test chambers. Output current was being driven directly into the voltage buffers, which immediately saturated the output to the rails. The buffers were erroneously designed in series from the electrode to multiplexers. Once the buffers were assembled in parallel with the current lines, the breadboard stages displayed ideal powering and behavior.

These issues were encountered once again during the transition to a PCB. Voltage probing was done with a Digilent Analog Discovery in scope mode to capture data related to the power rails on the refactored PCB platform. With the probes measuring the +/-9 V supplies, the expected behavior is a constant bipolar 9 V DC voltage output as shown in Figure A.7. The same rail was measured across a number of power cycles with power fluctuations happening in 4% of power cycles (Figure A.7). These power fluctuations are attributed to poor electrical contacts on the +/-2.5 V LDOs.

Figure A.7 9 V rails. Top, ideal +/-9 V supply rails. Middle, unexpected fluctuations in supply rails during operation. Bottom, power spiking on supply rails after disconnection and reconnection.

It was discovered that multiple plated through holes on the PCB had deformed or been removed during the initial soldering process. Without key connections to the pins of the -2.5 V LDO, the IC was damaged and pulled a high current from the 9 V power brick, resulting in heating of the component and damage to surrounding components. Upon replacement with a new -2.5 V LDO, the negative supply rails operated within specifications, but damage was

noticed on the +2.5 V LDO that was causing similar fluctuations until the device was non-operational and a new +2.5 V LDO was needed. With replacement of the supplies, the +/-2.5 V voltage rails were measured again, seen in Figure A.8.

It is important to note that there are fluctuations seen within the traces. These are attributed to poor electrical contacts from excessive soldering and desoldering of contacts during device debug phases. The PCB was designed with multiple redundant contacts for critical components. With the appropriate reconnections, the voltage rails operate with constant voltages of -2.5089 V and +2.74 V, well within the limits required of the ADG732 32 channel analog multiplexers.
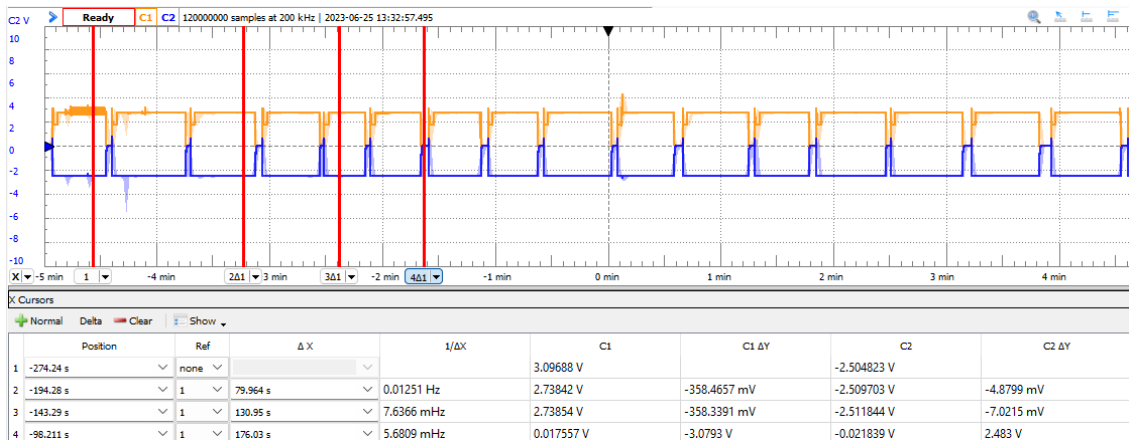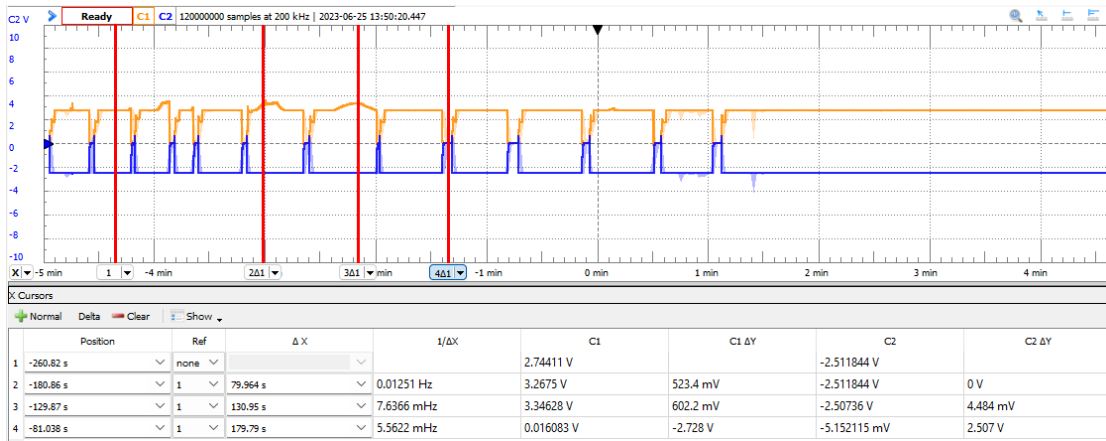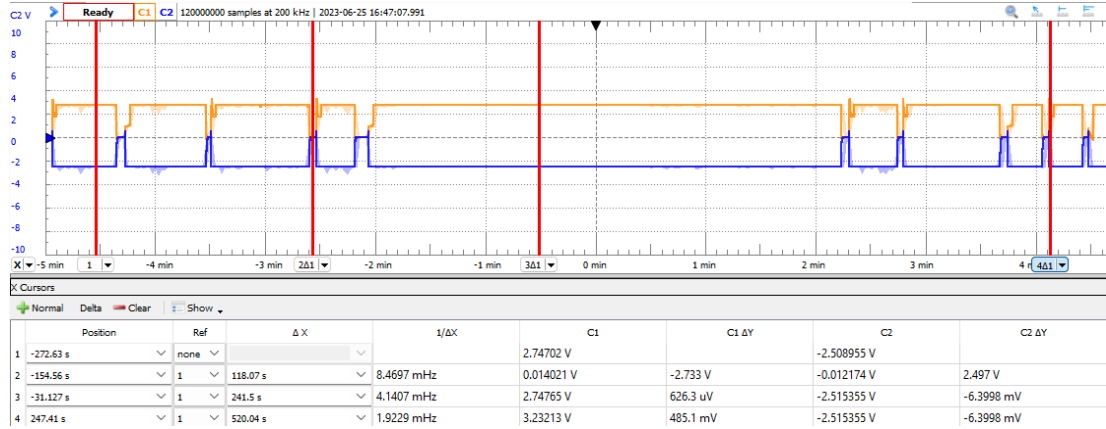
Figure A.8 2.5V Rails. Top, ideal operation of +/- 2.5 V rails with repeated disconnection, reconnection steps. Middle, power fluctuations from poor contact with V_{IN}. Bottom, +2.5 V rail with intermittent spiking.

These powering issues were finally resolved after using an ammeter on the VCCS. It was discovered that the VCCS was outputting up to 150 µA$_{RMS}$. Replacement of op amps and passive components did not resolve this issue, which is why the final design switched to a triple op amp system that showed better performance and output of an expected 10 µA current. This correction solved remaining power issues and the device performed as expected for the majority of testing. With validation complete, the focus shifted from hardware to software for image reconstruction.

Python Image Reconstruction Script

The Python script first describes the geometry of the test tank, taking parameters on the length, width, and height as well as the number of electrodes and the number of voxels used for the reconstruction. Three classes represent the voxel, electrodes, and the test body.

Voxel objects are created to store the individual data of each voxel, such as location, conductivity and higher level data including the calculations for G1, G2, and G3 from [11]. When the voxels are initialized, the script precomputes the G matrices to distribute the workload of the body class. These calculations take advantage of linear algebra to significantly reduce computation time.

Electrode objects store the location of each electrode in the system and have simple getter/setter member functions.

The bulk of the algorithm is handled by the body class, which uses linear algebra to compute the matrix $A_{x,k,r}, D_{x,k}$, and η_r. The body class also handles the initialization of the body, including the formatting of each voxel and electrode. In addition, the body class stores current, voltage, and current density vectors, either from measurement or from direct calculation of a homogenous body.

Finally, DisplayBody.py displays each voxel within the FEM mesh to display body B as a 3D plot. The plot displays each voxel with its opacity set to the conductivity, $\sigma(p)$, calculated

from the reconstruction algorithm. Opacity is the main visual identifier, chosen to function in a similar way to the reconstructions by EIDORS. Given that there will be small perturbations everywhere that the inclusion is not present, a low opacity serves the user to see through the bulk of the body to the less conductive, or higher opacity, inclusion.

CSV files with data from comparable EIDORS simulations are imported for validation of the image reconstruction. Data on the voltage measurement of each electrode is stored in each current and voltage vector that the script then uses to reconstruct the varying opacity body.

The culmination of these computations is an opaque body with a small inclusion in the upper right corner, Figure A.9. At first this was regarded as a success given the initial inclusion was a ball in the top corner in the EIDORS model. Given different data from EIDORS measurements or real data, the script fails to reconstruct the body in any different orientation. Computational values were verified with hand calculations and a comprehensive Excel spreadsheet, but the bug was unable to be corrected. Given the issues with the Python script, the decision was ultimately made to use EIDORS with the intent to correct the Python script in a future work.
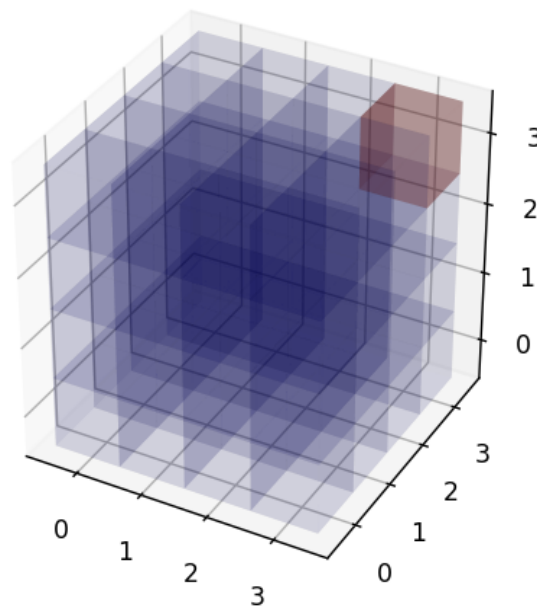
Figure A.9 Python script reconstruction of a 4x4x4 voxel system.

Effects of the Ill-Posed Inverse Problem

Artifacts are to be expected in an EIT image. Complex systems require an FEM with a large quantity of voxels to be effectively represented. The image reconstruction problem can be simplified to a linear algebra problem mapping a set of equations for the injected current and measured voltages to the unknown set of voxels. When there is an even number of equations to unknowns, the problem is well-posed and there is an accurate answer to the unknown conductivity matrix that corresponds to each voxel. As the number of voxels increases, so too does the amount of unknowns. The injection and measurement pattern does not continue to scale to reflect this increase in complexity as further measurements would be redundant. The linear system is now underdetermined or ill-posed. To solve this problem, regularization methods are used. At a high level, a regularization algorithm will add a penalty, or regularization parameter, to the solutions of the linear equations, trying to reduce the penalty's magnitude while finding the best solution to the problem [52].

In this paper, there appear to be significant differences in the conductivity displayed in the colormaps. This can be attributed to the different regularization methods used that utilize different *a priori* estimations of the conductivity, referred to as 'priors' in the EIDORS package. When comparing Figures 3.15 and 3.16, it appears that the data represents some numerical artifacts. In fact, this is not the case as it is the difference between the Laplace prior and NOSER prior in the EIDORS package. The NOSER prior regularization colormap reports conductivity values in the range of [1, -1.5] $S \cdot m^{-1}$ while the Laplace prior regularization displays a uniform conductivity colormap of -118513 $S \cdot m^{-1}$. Initial investigation suggested that the reported figures may be reporting the reconstructions improperly. A sanity check was conducted on homogenous data compared against the same homogeneous data acting as the inclusion dataset. It would follow that this would result in a fully transparent reconstruction as there would

be no change of surface measurements. As expected, in Figure A.10 a transparent chamber is displayed using both a Laplace and NOSER regularization priors.
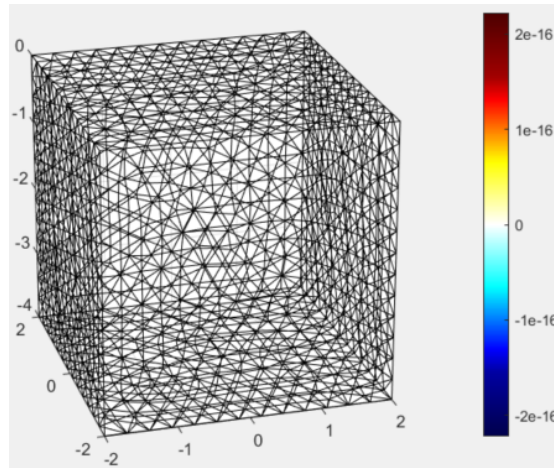
Figure A.10 Control reconstruction of the homogenous data against the same dataset acting as the non homogeneous data.

Upon further investigation of the EIDORS reconstruction script for Figure 3.19, it is apparent that the values are the same to the ninth significant digit when using the Laplace prior, at which point there is variation in the significant digits. Through regularization of the data, a clearer representation is displayed in Figure A.11.
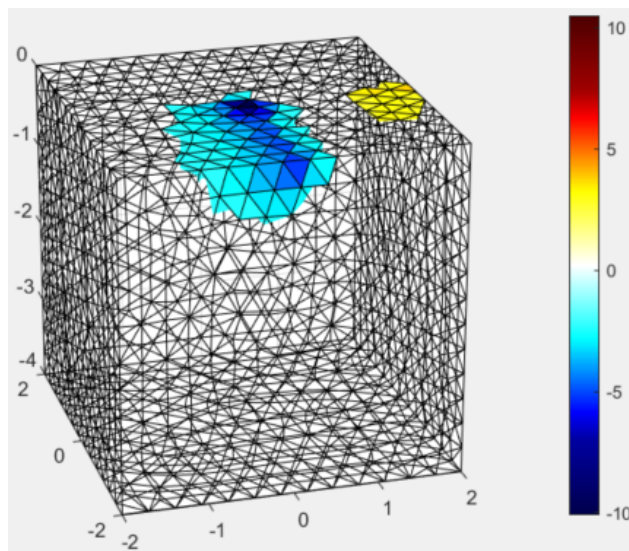
Figure A.11 Regularization of element data in inverse model FEM.

The colormaps of other regularization techniques can also add confusion. Gaussian high pass filtering and movement priors resulted in similarly odd colormap behavior, which could also be corrected through normalization of the data, but the reconstructions overall displayed the same inclusion, as displayed in Figure A.12. In Chapter 3, the figures are displayed with the Laplace regularization technique where the reconstruction was more representative of the real inclusion. It is well documented that there is no 'best' selection of the regularization technique, but rather each model requires empirical analysis of the reconstruction to find the best fit for each test case [52].
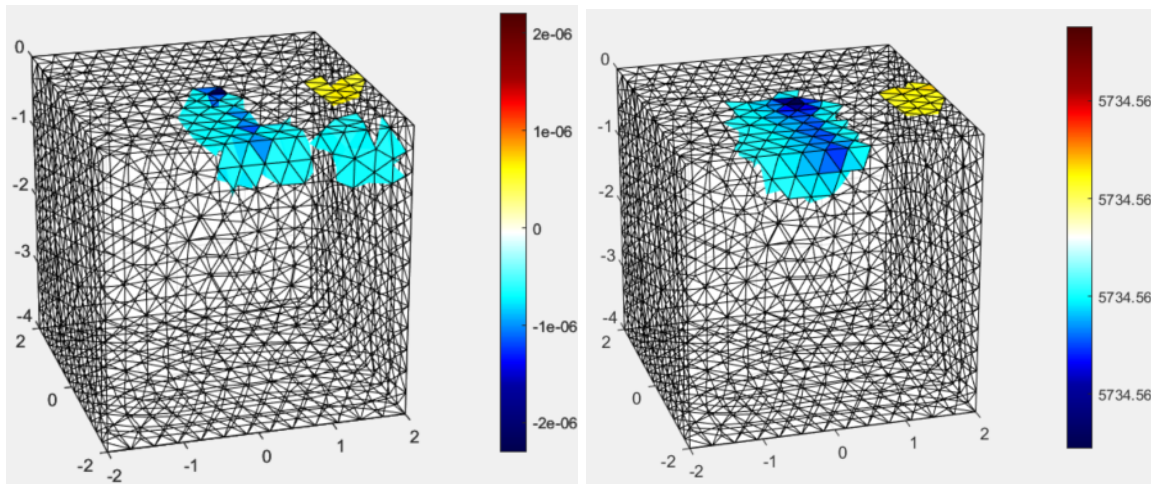
Figure A.12 Different reconstruction priors are used. Right, a gaussian high pass filter is applied to the reconstruction. Left, a movement prior is applied to the reconstruction. Note that the range is the same as in Figure 3.19.

Transient Issues in Current Injection and Analog-to-Digital Conversions

Current spiking from the VCCS resulted in overvoltage of the RMS-to-DC converters that damaged the ADC1115 ICs and subsequently crashed the Teensy 4.0 development board. This was a taxing issue as the diagnostic code on the Teensy 4.0 blinked 9 times, indicating an ARM JTAG DAP Init Error. The error prevented the microcontroller from connecting to the host PC and obfuscating the underlying issue of the ADC damage. It was only after sinking considerable hardware development time into replacing and testing the development board that it was made

clear that the ADS1115 had failed, specifically in the I2C bus. The issue can be traced to the firmware that initializes the ADCs. The ADS1115 control firmware designed by Adafruit leads to COM port erasure and the system no longer detects the development board. Only after resetting the board and reprogramming the default test sketch to the Arduino does the device enumerate. It is unknown why this software is causing the device to hang when it worked fine for the majority of the development process. Redevelopment of the I2C communication protocol that initializes the ADC control registers and accesses the conversion data register is shown to work, which contradicts the initial malfunction analysis that pointed to an I2C problem. Instead, the issue was pinpointed in the setup commands in the commercial control firmware from Adafruit. Other functions in the provided firmware functioned correctly with the ADCs, but the devices could not be properly initialized, which is why the functions had to be refactored with lower level Wire.h function calls. To prevent this in future testing, voltage protection circuitry has been added in the form of a voltage buffer between the RMS-to-DC converter and ADC input pins, running off of the 3.3 V supply rail. As the expected voltage from the ADCs should be positive with a maximum value of 2 V, this rail should protect the ADC and limit interference with conversions.

Despite the hardware limitations, further testing was conducted with a Digilent Analog Discovery operating as a waveform generator instead of the DDS IC. Internal circuitry had been damaged somewhere in the design, outputting a magnitude of 115 μA_{RMS}-140 μA_{RMS} when connected to the DDS, and 7.0 μA_{RMS} when connected to an analogous wave from the Digilent Discovery. The waveform was 1 kHz at 50 mV_{pp}. Excitingly, the system was stable during testing and no voltage spikes were seen on a multimeter used to verify the input signal to the ADCs before the system was reconnected.

References

[1] Adler, Andy, and Alistair Boyle. "Electrical impedance tomography: Tissue properties to image measures." IEEE Transactions on Biomedical Engineering 64.11 (2017): 2494-2504.

[2] Dehghani, Hamid, and Nirmal K. Soni. "Electrical impedance spectroscopy: theory." Alternative Breast Imaging. Springer, Boston, MA, 2005. 85-105.

[3] Liu, Jinlong, *et al*. "Real-time measurement of trans-epithelial electrical resistance in organ-on-a-chip during cell proliferation." Analyst (2023).

[4] Lee, Hyosang, et al. "Soft nanocomposite based multi-point, multi-directional strain mapping sensor using anisotropic electrical impedance tomography." Scientific reports 7.1 (2017): 1-10.

[5] Lehti-Polojärvi, Mari, Olli Koskela, and Jari Hyttinen. "Multifrequency electrical impedance tomography in biological applications: A multimodal perspective." Bioimpedance and Spectroscopy. Academic Press, 2021. 157-189.

[6] Zhang, Yang, Robert Xiao, and Chris Harrison. "Advancing hand gesture recognition with high resolution electrical impedance tomography." Proceedings of the 29th Annual Symposium on User Interface Software and Technology. 2016.

[7] Adler, Andy, Pascal Olivier Gaggero, and Yasheng Maimaitijiang. "Adjacent stimulation and measurement patterns considered harmful." Physiological measurement 32.7 (2011): 731.

[8] Benson, Kathrin, Sandra Cramer, and Hans-Joachim Galla. "Impedance-based cell monitoring: barrier properties and beyond." Fluids and Barriers of the CNS 10.1 (2013): 1-11.

[9] Nicolas, A., et al. "High throughput transepithelial electrical resistance (TEER) measurements on perfused membrane-free epithelia." Lab on a Chip 21.9 (2021): 1676-1685.

[10] Islam, Shekh Md Mahmudul, Md Anisur Rahman Reza, and Md Adnan Kiber. "A study of phantoms of multi-frequency Electrical Impedance Spectroscopy (EIS) system for early detection of breast cancer." 2013 International Conference on Informatics, Electronics and Vision (ICIEV). IEEE, 2013.

[11] Choi, Myoung Hwan, et al. "A reconstruction algorithm for breast cancer imaging with electrical impedance tomography in mammography geometry." IEEE transactions on biomedical engineering 54.4 (2007): 700-710.

[12] Boverman, Gregory, et al. "Robust linearized image reconstruction for multifrequency EIT of the breast." IEEE Transactions on Medical Imaging 27.10 (2008): 1439-1448.

[13] Ozkan, Gulay, et al. "Effects of lipid-based encapsulation on the bioaccessibility and bioavailability of phenolic compounds." Molecules 25.23 (2020): 5545.

[14] Zoio, Patrícia, Sara Lopes-Ventura, and Abel Oliva. "Barrier-on-a-chip with a modular architecture and integrated sensors for real-time measurement of biological barrier function." Micromachines 12.7 (2021): 816.

[15] Srinivasan, Balaji, et al. "TEER measurement techniques for in vitro barrier model systems." SLAS Technology 20.2 (2015): 107-126.

[16] Rahman, A. R. A., et al. "Cell culture monitoring by impedance mapping using a multielectrode scanning impedance spectroscopy system (CellMap)." Physiological measurement 29.6 (2008): S227.

[17] Mariadason, John M., David H. Barkla, and PETER R. Gibson. "Effect of short-chain fatty acids on paracellular permeability in Caco-2 intestinal epithelium model." American Journal of Physiology-Gastrointestinal and Liver Physiology 272.4 (1997): G705-G712.

[18] Toutounji, Mohamad, et al. "Dextran sodium sulfate-induced impairment of protein trafficking and alterations in membrane composition in intestinal Caco-2 cell line." International journal of molecular sciences 21.8 (2020): 2726.

[19] van der Helm, Marinke W., et al. "Non-invasive sensing of transepithelial barrier function and tissue differentiation in organs-on-chips using impedance spectroscopy." Lab on a Chip 19.3 (2019): 452-463.

[20] Chaparro, C. V., et al. "Considerations on electrical impedance measurements of electrolyte solutions in a four-electrode cell." Journal of Physics: Conference Series. Vol. 687. No. 1. IOP Publishing, 2016.

[21] Henry, Olivier YF, et al. "Organs-on-chips with integrated electrodes for trans-epithelial electrical resistance (TEER) measurements of human epithelial barrier function." Lab on a Chip 17.13 (2017): 2264-2271.

[22] Renous, Noa, et al. "Spatial trans-epithelial electrical resistance (S-TEER) integrated in organs-on-chips." Lab on a Chip 22.1 (2022): 71-79.

[23] Odijk, Mathieu, et al. "Measuring direct current trans-epithelial electrical resistance in organ-on-a-chip microsystems." Lab on a Chip 15.3 (2015): 745-752.

[24] Lo, Chun-Min, Charles R. Keese, and Ivar Giaever. "Cell–substrate contact: another factor may influence transepithelial electrical resistance of cell layers cultured on permeable filters." Experimental cell research 250.2 (1999): 576-580.

[25] Boone, K. G., and D. S. Holder. "Current approaches to analogue instrumentation design in electrical impedance tomography." Physiological measurement 17.4 (1996): 229.

[26] Khalighi, M., and M. Mikaeili. "A floating wide-band current source for electrical impedance tomography." Review of Scientific Instruments 89.8 (2018): 085107.

[27] *Programmable Frequency Sweep and Output Burst Waveform Generator Data ...*, www.analog.com/media/en/technical-documentation/data-sheets/AD5930.pdf. Accessed 21 Sept. 2022.

[28] Tucker, Aaron S., Robert M. Fox, and Rosalind J. Sadleir. "Biocompatible, high precision, wideband, improved Howland current source with lead-lag compensation." IEEE Transactions on Biomedical Circuits and Systems 7.1 (2012): 63-70.

[29] Russo, Stefania, et al. "Development of a high-speed current injection and voltage measurement system for electrical impedance tomography-based stretchable sensors." Technologies 5.3 (2017): 48.

[30] Franco, Sergio. "The Howland Current Pump - Technical Articles." All About Circuits, www.allaboutcircuits.com/technical-articles/the-howland-current-pump/. Accessed 20 Sept. 2022.

[31] Liu, Jinzhen, et al. "The differential Howland current source with high signal to noise ratio for bioimpedance measurement system." Review of Scientific Instruments 85.5 (2014): 055111.

[32] Ansory, Achmad, Prawito Prajitno, and Sastra Kusuma Wijaya. "Design and development of electrical impedance tomography system with 32 electrodes and microcontroller." AIP Conference Proceedings. Vol. 1933. No. 1. AIP Publishing LLC, 2018.

[33] Sapuan, Imam, et al. "Anomaly Detection Using Electric Impedance Tomography Based on Real and Imaginary Images." Sensors 20.7 (2020): 1907.

[34] Cook, Raymond Douglas, et al. "ACT3: a high-speed, high-precision electrical impedance tomograph." IEEE Transactions on Biomedical Engineering 41.8 (1994): 713-722.

[35] Yang, Lang, and Tom Chen. "A compact signal generation and acquisition circuit for electrochemical impedance spectroscopy." 2016 IEEE Biomedical Circuits and Systems Conference (BioCAS). IEEE, 2016.

[36] Mixed-Signal and Digital Signal Processing ICS | Analog Devices, www.analog.com/media/en/technical-documentation/data-sheets/ADG726_732.pdf. Accessed 15 June 2022.

[37] https://github.com/alex-d-gard/TEER_Thesis_Repo.git

[38] Gaggero, Pascal O., et al. "Active Electrode Based Electrical Impedance Tomography System." (2011).

[39] Shi, Xuetao, et al. "High-precision electrical impedance tomography data acquisition system for brain imaging." IEEE Sensors Journal 18.14 (2018): 5974-5984.

[40] Single-Supply, Low Power, Precision FET Input Quad Buffer Data Sheet AD8244, www.analog.com/media/en/technical-documentation/data-sheets/AD8244.pdf. Accessed 25 Dec. 2022.

[41] TPS723 200-MA, Low-Noise, High-PSRR, Negative Output Low-Dropout Linear ...,

www.ti.com/lit/ds/symlink/tps723.pdf. Accessed 30 July 2022.

[42] Cap-FREENMOS 250-Malow Dropout Regulator with Reverse Current ... - Ti.Com,

www.ti.com/lit/ds/symlink/tps73201-ep.pdf. Accessed 21 Sept. 2022.

[43] PowerBRICK Reference Manual Overview Input Voltage - Mouser Electronics,

www.mouser.com/datasheet/2/690/powerbrick_rm-932625.pdf. Accessed 2 Aug. 2022.

[44] LM741-Mil Operational Amplifier Datasheet - Texas Instruments India,

www.ti.com/lit/ds/symlink/lm741-mil.pdf. Accessed 16 July 2022.

[45] DHT11 Humidity & Temperature Sensor - Mouser Electronics,

www.mouser.com/datasheet/2/758/DHT11-Technical-Data-Sheet-Translated-Version-1143054.p

df. Accessed 21 Aug. 2022.

[46] Zamora-Arellano, Francisco, et al. "Development of a portable, reliable and low-cost

electrical impedance tomography system using an embedded system." Electronics 10.1 (2020):

15.

[47] Griffiths, Hugh. "A phantom for electrical impedance tomography." Clinical Physics and

Physiological Measurement 9.4A (1988): 15.

[48] A RF/If Gain and Phase Detector LF–2.7 GHz AD8302,

www.analog.com/media/en/technical-documentation/data-sheets/AD8302.pdf. Accessed 10 July

2022.

[49] Low Cost, Low Power, True RMS-to-DC Converter Data Sheet AD736,

www.analog.com/media/en/technical-documentation/data-sheets/AD736.pdf. Accessed 8 Aug.

2022.

[50] Griffiths, H. "The importance of phase measurement in electrical impedance tomography."

Physics in Medicine & Biology 32.11 (1987): 1435.

[51] ADS111x Ultra-Small, Low-Power, I2C-Compatible, 860-SPS, 16-Bit Adcs ...,

www.ti.com/lit/ds/symlink/ads1115.pdf. Accessed 15 Aug. 2022.

[52] Adler, Andy, and David Holder, eds. Electrical impedance tomography: methods, history and applications. CRC Press, 2021.

[53] Adler, Andy, and William RB Lionheart. "Uses and abuses of EIDORS: an extensible software base for EIT." Physiological measurement 27.5 (2006): S25.

[54] Polydorides, Nick, and William RB Lionheart. "A Matlab toolkit for three-dimensional electrical impedance tomography: a contribution to the Electrical Impedance and Diffuse Optical Reconstruction Software project." Measurement science and technology 13.12 (2002): 1871.

[55] Jehl, Markus, et al. "A fast parallel solver for the forward problem in electrical impedance tomography." IEEE Transactions on Biomedical Engineering 62.1 (2014): 126-137.

[56] Mueller, Jennifer L., David Isaacson, and Jonathan C. Newell. "A reconstruction algorithm for electrical impedance tomography data collected on rectangular electrode arrays." IEEE Transactions on Biomedical Engineering 46.11 (1999): 1379-1386.

[57] Taylor, Stephen H., and Suresh V. Garimella. "Design of electrode arrays for 3D capacitance tomography in a planar domain." International Journal of Heat and Mass Transfer 106 (2017): 1251-1260.

[58] Hua, Ping, et al. "Iterative reconstruction methods using regularization and optimal current patterns in electrical impedance tomography." IEEE Transactions on Medical Imaging 10.4 (1991): 621-628.

[59] Khalighi, Mohammad, and Mohammad Mikaeili. "Modified weighted back-projection algorithm (MWBP) for 3D electrical impedance mammography systems with the planar electrode array." Biomedical Physics & Engineering Express 5.6 (2019): 065020.

[60] Cheney, Margaret, et al. "NOSER: An algorithm for solving the inverse conductivity problem." International Journal of Imaging systems and technology 2.2 (1990): 66-75.

[61] Ren, Zhen, and Wuqiang Yang. "A miniature two-plate electrical capacitance tomography sensor." IEEE Sensors Journal 15.5 (2015): 3037-3049.

[62] Dimas, Christos, and Paul P. Sotiriadis. "Electrical impedance tomography image reconstruction for adjacent and opposite strategy using FEMM and EIDORS simulation models." 2018 7th International Conference on Modern Circuits and Systems Technologies (MOCAST). IEEE, 2018.

[63] Perez, Husein, Michael Pidcock, and Cristiana Sebu. "A three-dimensional image reconstruction algorithm for electrical impedance tomography using planar electrode arrays." Inverse Problems in Science and Engineering 25.4 (2017): 471-491.